Multidimensional Simulations of Core Collapse Supernovae using a Two-patch Overset Grid in Spherical Coordinates

Annop Wongwathanarat

Technische Universität München

Physik Department

Max-Planck-Institut für Astrophysik

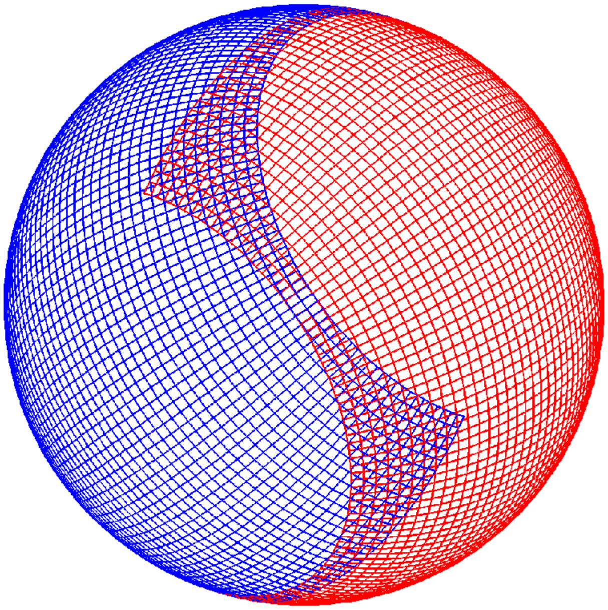

Technische Universität München
Max-Planck-Institut für Astrophysik

Multidimensional Simulations of Core Collapse Supernovae using a Two-patch Overset Grid in Spherical Coordinates

Annop Wongwathanarat

Vollständiger Abdruck der von der Fakultät für Physik der Technischen Universität München zur Erlangung des akademischen Grades eines

Doktors der Naturwissenschaften

genehmigten Dissertation.

Vorsitzender:		Univ.-Prof. Dr. L. Oberauer
Prüfer der Dissertation:		
	1.	Priv.-Doz. Dr. E. Müller
	2.	Univ.-Prof. Dr. H. Friedrich

Die Dissertation wurde am 03.02.2011 bei der Technischen Universität München eingereicht und durch die Fakultät für Physik am 24.02.2011 angenommen.

Abstract

The aim of this thesis is to study neutrino-driven core collapse supernovae by means of three-dimensional computer simulations. The computing time needed for the simulations is significantly reduced by using an overlapping grid technique called the “Yin-Yang” grid for spatial discretization of the computational domain in spherical coordinates which also avoids grid singularities in angular direction. The hydrodynamical neutron star kick mechanism and the mixing of elements in the stellar envelope are investigated. My results provide new insights into the connection of the neutron star’s peculiar motion and the distribution of elements observed in supernova ejecta. The results are compared with those of previous works and current observations of supernova remnants.

Zusammenfassung

Ziel dieser Arbeit ist das Studium von neutrino-getriebenen Gravitationskollaps-Supernovae mit Hilfe dreidimensionaler hydrodynamischer Simulationen, Die dafür benötigte Rechenzeit kann erheblich reduziert werden, wenn man ein Yin-Yang-Gitter zur Diskretisierung des Rechengebiets verwendet. Dabei handelt es sich um ein überlappendes Rechengitter in Kugelkoordinaten, das keine Gittersingularitäten in beiden Winkelkoordinaten aufweist. Unter Verwendung dieser Methode wurde sowohl der hydrodynamische Mechanismus untersucht, der für die Entstehung der Eigenbewegung von Neutronensternen diskutiert wird, als auch Mischvorgänge in Supernovahüllen studiert. Meine Rechnungen sagen voraus, dass die Eigenbewegung des Neutronensterns und die räumliche Verteilung der bei der Explosion ausgeschleuderten Elemente korreliert sind. Die Ergebnisse werden mit denen früherer Arbeiten und mit Boebachtungsdaten von Supernova-Überesten verglichen.

Parts of this thesis have already been published in

1. A. Wongwathanarat, N. J. Hammer, and E. Müller,
   An axis-free overset grid in spherical polar coordinates for simulating 3D self-gravitating flows,
   A&A, 514, A48, (2010)
2. A. Wongwathanarat, H.-Th. Janka, and E. Müller,
   Hydrodynamical neutron star kicks in three dimensions,
   ApJL, 725, L106, (2010)

Contents

Abstract **1**

Zusammenfassung **3**

1 Motivation **9**

1.1 Need for Multi-dimensional Models 9
1.2 Computational Challenge 10
1.2.1 Outline of thesis 12

2 Core Collapse Supernova **13**

2.1 Historical Supernovae 13
2.2 Modern supernova observation 14
2.3 Supernova Classification 14
2.4 Core Collapse Supernovae Theory 19

3 Numerical Techniques **23**

3.1 Governing Equations 23
3.2 The Yin-Yang Grid 24
3.2.1 Grid Geometry and Transformations 24
3.2.2 Implementation 27
3.3 Self-gravity Solver 29
3.4 Additional Physics 31
3.4.1 Explosion Simulation 32
3.4.2 Long-time Shock Propagation Simulation 32

4 Test Suites **35**

4.1 Sod Shock Tube 35
4.2 Taylor-Sedov Explosion 39
4.3 Rayleigh-Taylor Instability 43
4.4 Gravitational Potential of Homogeneous Spheroids 45
4.5 Self-gravitating Polytropes 47
4.6 Conservation problem 51
4.7 Performance and Efficiency 53

5 Hydrodynamical Neutron Star Kicks in 3D **57**
5.1 Grid and Simulation Setup 58
5.1.1 Explosion Simulation 58
5.1.2 Long-time Simulation 58
5.2 Computed Models 59
5.3 Neutron star kicks 59
5.3.1 Simulation results 59
5.3.2 Kick mechanism: theory and toy models 66
5.3.3 Analytic estimates of the kick magnitude 68
5.3.4 Mode analysis 71
5.3.5 Contribution by anisotropic neutrino emission 71
5.3.6 Neutron star spins 73

6 Element Distribution in Supernova Ejecta **75**
6.1 Connection with Neutron Star Kick 75
6.2 Supernova Shock Propagation and Element Distribution 80
6.3 Distribution in Mass Coordinate and Velocity Space 88
6.4 Comparison with Previous Work 90
6.5 Comparison with current observations 90
6.5.1 Neutron star kicks and heavy elements distributions 90
6.5.2 Mixing of elements in stellar envelopes 93

7 Summary and outlook **95**

Chapter 1

Motivation

A core-collpase supernova explosion (CCSN) is one of the most interesting astrophysical phenomena. It presents the final stage of massive stars larger than approximately $8\,M_\odot$, where $M_\odot$ is the solar mass. It involves highly complicated physics length scales, ranging from the stellar radius ($\sim 10^{13}\,\mathrm{cm}$) down to the microscopic scale, and timescales stretching from hours to milliseconds. Tremendous amounts of gravitational binding energy of the order of 10^{53} erg are released by the explosion within a timescale of seconds only. Most of the energy is carried away by numerous neutrinos streaming out from the explosion site. Nucleosysthesis processes which occur during the explosion are an important source of heavy elements (elements heavier than oxygen) in our universe. Once the star explodes these heavy elements are ejected and later mixed into the interstellar medium. Ultimately, these elements pollute molecular clouds which are the sites for star formation. The next generation of stars then form with some metals whose presence slightly changes the way how a star evolves. CCSNe are not only important for galactic chemical evolution and stellar evolution, but are also important for the origin of elements required for life forms on Earth. Asymmetric CCSNe are thought to be interesting sources of gravitational wave emission, too. It is obvious that studying such events could provide us with a better understanding of many physics areas, such as nuclear physics, neutrino physics, element synthesis, turbulent mixing, and general relativity. Despite the fact that the basic concepts of how CCSNe explode have been studied for five decades already, astrophysicists still have not been able to reach a final conclusion regarding the explosion mechanism.

1.1 Need for Multi-dimensional Models

Numerical simulations of stellar core collapse and the subsequent explosion of a massive star have shown that a successful explosion cannot be acheived when assuming spherical symmetry (e.g., Rampp & Janka 2000; Buras et al. 2003; Thompson et al. 2003; Buras et al. 2006) except for the case of $\lesssim 10\,M_\odot$ progenitors (Kitaura et al. 2006). Thus, multi-dimensional effects must play an important role for the explosion mechanism. During the past decade astrophysicists have been performing simulations of CCSNe mainly in two dimensions enforcing axisymmetry. They have found multi-dimensional hydrodynamic instabilities developing in their models which seem to play a crucial role for understanding CCSN explosions. Nevertheless, they have not yet been able to decipher the mystery completely. Naturally, the question arises what happens in a full three dimensional simulation, particularly as observations also show very complex

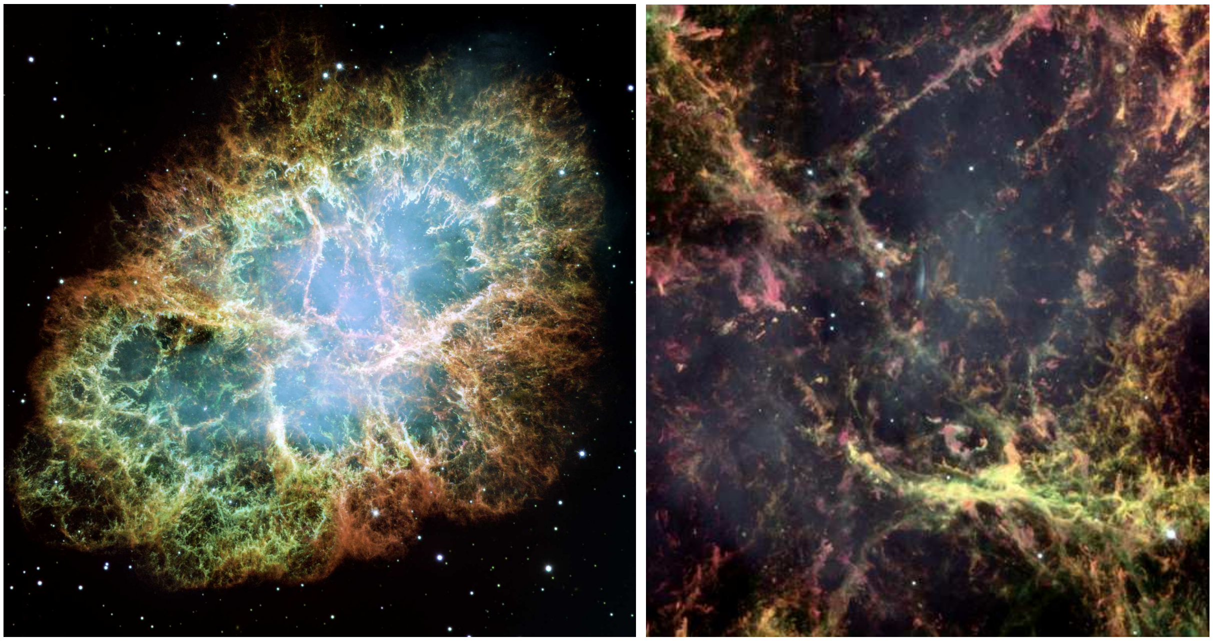

Figure 1.1: The Crab nebula (left) and the zoom-in picture (right) taken by the Hubble Space Telescope (HST). Credit: NASA/ESA, J. Hester and A. Loll (Arizona State University), the Hubble Heritage Team (STScI/AURA), and W. P. Blair (JHU).

three-dimensional structures in supernova (SN) ejecta, *e.g.,* in the Crab nebula (Figure 1.1), the remnant of a SN explosion from the year 1054. The overall geometry of the ejecta is of oval shape. The three-dimensional structure is thought to be a prolate spheroid (Trimble 1973). The filaments contain ejected material from the explosion consisting of hydrogen, helium, carbon, oxygen, nitrogen, iron, and neon. Obviously, large scale mixing occured by hydrodynamic instabilities of elements synthesized during the explosion and those present in the envelope of the progenitor's star. Therefore, modelling the collapse and explosion of massive stars ultimately requires computations in three spatial dimensions.

1.2 Computational Challenge

Since a star is best described with a spherical coordinate system we focused on modelling CCSNe using spherical polar coordinates. In a 3D finite-volume hydrodynamic simulation employing spherical polar coordinates (r, θ, ϕ) the computational volume is spatially discretized into N_r spherical shells, where each shell is discritized by a latitude-logitude grid of N_θ and N_ϕ zones in θ and ϕ direction, respectively. The coordinate center of each grid cell is then given by

$$r_i = R_0 + i \cdot \frac{\Delta r}{2} \quad \text{for} \quad 1 \leq i \leq N_r, \tag{1.1}$$

$$\theta_j = \theta_0 + j \cdot \frac{\Delta \theta}{2} \quad \text{for} \quad 1 \leq j \leq N_\theta, \tag{1.2}$$

$$\phi_k = \phi_0 + k \cdot \frac{\Delta \phi}{2} \quad \text{for} \quad 1 \leq k \leq N_\phi, \tag{1.3}$$

where R_0 and Δr are the inner radius of the grid boundary and grid spacing in the radial direction, respectively. The colatitude θ ranges from $\theta = 0$ to $\theta = \pi$ corresponding to the north and south pole, respectively. The azimuth ϕ covers $\phi = 0$ to $\phi = 2\pi$. By choosing logarithmicallly spaced radial grid one automatically achieves very high spatial resolution at small radii while the total number of radial grid zones remains fairly small compared to a grid in Cartesian coordinates. For example, in this work we use 400 logarithmically spaced radial grid zones to cover the central part of the star to the radius of $\sim 2 \times 10^9$ cm. The spatial resolution near the inner radial grid boundary is approximately 30 m. If one were to use a cube of Cartesian grid, one needs a grid of the order of 10^{18} grid zones which would be impossible using the current supercomputing power. However, the spherical polar grid comprises of grid lines which converge towards the north and south pole. This implies a severe restriction of the time step size for any hydrodynamic code using explicit time discretization due to the Courant-Friedrichs-Levy (CFL) condition, which is referred to as the so-called "pole problem". In addition, boundary conditions that have to be imposed at the coordinate symmetry axis ($\theta = 0, \pi$) flaw the simulations by causing undesired numerical artifacts near the axis which can be observed in 2D axisymmetric simulations, as e.g., finger-like flow features (Kifonidis et al. 2003). For 3D flows, the coordinate axis represents a coordinate singularity that almost unavoidably will leave its mark on the flow near or when crossing the axis.

An easy workaround which helps easing the time step restriction can be realized by omitting a small cone at the poles from the computational volume, e.g., setting $\theta_0 = 5^\circ$. This causes already a quite substantial gain in the time step size at the cost of losing only $\approx 0.4\%$ of the 4π solid angle. However, it does not solve the problem of axes artifacts, since boundary conditions in θ-direction are still required.

There have also been attempts to construct a new type of grid which avoids the pole problem. However, it is not possible to construct a single grid that can cover the entire 4π surface of a sphere, is orthogonal, and at the same time does not contain any coordinate singularity except at the origin. Multi-patch grids and overlapping (or overset) grids are employed. Such grids are widely used in the field of computational fluid dynamics, where complex grid structures are common. For flows possessing an approximate global spherical symmetry, the "cubed sphere" grid (Ronchi et al. 1996) has been developed and is currently applied to several astrophysical problems (Koldoba et al. 2002; Romanova et al. 2003; Zink et al. 2008; Fragile et al. 2009, e.g.). It is an overset grid consisting of six identical patches covering a solid angle of 4π steradians. The "Yin-Yang" grid which is used in this thesis has the latter property, too, but up to now it has not been applied to astrophysical problems. The Yin-Yang grid was introduced by Kageyama & Sato (2004). It consists of two overlapping grid patches named "Yin" and "Yang" grid. In comparison with other types of overset grids in spherical geometry, the Yin-Yang grid geometry is simple, as both the Yin and the Yang grid consist of a part of a usual spherical polar grid. The transformation of coordinates and vector components between the two patches is straightforward and symmetric, thus allowing for an easy and straightforward implementation of the grid into a 3D code already employing spherical polar coordinates. The Yin-Yang grid is successfully used on massively parallel supercomputers in the field of geophysical science for simulations of mantle convection and the geodynamo. In these applications the thermal convection equation and the magnetohydrodynamic (MHD) equations are solved on the Yin-Yang grid using a second-order accurate finite difference method. Here, we also adopt the Yin-Yang grid, and use it for astrophysically relevant (finite-volume) hydrodynamic simulations for the first time.

1.2.1 Outline of thesis

The thesis is structured as follows. In Section 2, we start by discussing historical and modern observations of supernovae, following by the classification of supernova types and the current picture of the core collapse supernova theory. In Section 3, we describe numerical techniques and the computer code used in the thesis. We presents results from test simulations to verify the viability of the computer code in Section 4. We also discuss the efficiency and performance of the new grid technique in comparison with the usual spherical polar grid. In Section 5, we report on the results obtained from three-dimensional simulations studying the hydrodynamical neutron star kick mechanism. In Section 6, results from long-time three-dimensional simulations studying mixing of elements in the envelope of the progenitor star are discussed. Finally, we summarize our findings in Section 7.

Chapter 2

Core Collapse Supernova

2.1 Historical Supernovae [1]

> 中平二年十月癸亥客星出南門中大如半筵五色喜怒稍小至後年
> 六月消占曰為兵至六年司隸校尉袁紹誅滅中官大將軍部曲將吳
> 匡攻殺車騎將軍何苗死者數千人

> “In the second year of the *Zhongping* reign period, the 10th month, on the day *Guihai* [7 December, AD 185], a ’guest star’ emerged from the middle of the asterism *Nanmen* [Southern Gate]. It seemed to be as large as half a *yan* [bamboo mat]. It displayed the five colors, and *xi* [pleasure] and *nu* [anger]. It decreased gradually in size and in brightness. In the sixth month of the next year [5 July to 2 August 186] it disappeared. According to the standard prognostication this means military action. In the sixth year of the same reign period [AD 189] Metropolitan Commandant *Yuan Shao* wiped out the eunuchs; an officer *Wu Kuang* of the General-in-Chief attacked and killed *He Miao*, the Chariot and Horse General, and several thousand people were killed.”

says the first recorded supernova by mankind in *Houhanshu*, the official history of the Later Han Dynasty (AD 23-220) (Chin & Huang 1994). The term “guest start” was used as at that time, the time long before the word “supernova” was invented, yet, the record is informative enough for modern scientists to be able to identify the object RCW86 as a prime candidate for the supernova remnant (SNR) of this historical supernova (Stephenson & Green 2002). This suddenly appeared guest star was remarkably bright, bright enought to see with naked eyes, and it remained for several months before its shining light died out. Such an event is quite rare as within the next several hundred years there were only two more events, SN386 and SN393.

Later on, in 1006, the brightest supernova recorded was observed. It could possibly be seen even during the daytime. The radio source PKS1459-41 was associated as the remnant of SN1006 only in 1965 (Gardner & Milne 1965). The supernova of AD 1054 is also a very well-known supernova thanks to its associated remnant, the Crab Nebula. It is even more interesting in particular since later one of the first pulsars to be discovered was found at the center of the

---

[1] This section is based on the book by Marschall (1988), “The Supernova Story”.

Crab Nebula (Staelin & Reifenstein 1968). Over a hundred year later another supernova was seen in 1181, however, with several magnitudes dimmer than the previous one.

In 1572, Tycho Brahe, a Danish astronomer, observed a supernova in the constellation of Cassiopeia. Although he was not the first to observe the supernova his observation was conducted with great precision. Tycho's supernova was visible as long as 18 months. Another supernova, although dimmer than Tycho's supernova, visible to naked eyes was spotted in 1604 in the constellation of Ophiuchus. Johannes Kepler, who was the assistant of Brahe, was among the discoverers of this supernova. Kepler conducted systematic observations and published a book which later on helped marking his name on the supernova of 1604. Kepler's supernova is, as recorded, the last supernova within our Galaxy observed from the Earth.

Also in the seventeenth century a galactic supernova exploded in the direction of the constellation Cassiopeia known nowadays as the Cassiopeia A (Cas A) supernova. However, it appeared to be much dimmer than previous galactic supernovae due to obscuration by dust cloud. Therefore, it was not identified as a supernova at that time, although there exists evidences that it might have been observed by John Flamsteed and identified as a star of sixth magnitude. Inferred by the expansion velocity of the Cas A SNR its explosion epoch is estimated to be about 1667 (Hughes 1980). The Cas A remnant is also an extremely bright radio source on the sky. Up to now, the youngest known galactic supernova is the one which occurred around 1870. It also was not observed since it exploded near the galactic center hidden behind optically opaque gas clouds. Instead, it was discovered as a SNR by radio observation in 1984, only (Green & Gull 1984). The remnant is named G1.9+0.3. The age of this supernova is estimated by combining radio images with X-ray images from the Chandra X-ray satellite of different epochs.

2.2 Modern supernova observation

In the last section, we focused mainly on SNe that exploded inside our own galaxy since astronomers in the past relied only on observations by eye or ground-based optical telescopes. Nowadays, new instruments, both ground-based and space-based, allow astronomers to detect SN events at much larger distances. Up until now, they have detected ∼5000 extragalactic SNR [2] with hundreds of new detection every year. Moreover, the detection rate is likely to increase in the future when more SN survey projects are operative.

One of the most important SN observation was the detection of SN 1987A, which is a CCSN explosion in the Large Magellanic Cloud (LMC), a nearby (∼ 50 kpc) satellite galaxy of the Milky Way. Being the closest directly observed SN explosion since SN1604, the Kepler's SN, it is the one studied in most detail up to now. Moreover, it is so far the only SN that astronomers were able to detect neutrino emission associated with the explosion as predicted by CCSN theory. Astronomers also expect to eventually detect the neutron star remnant formed in this particular SN.

2.3 Supernova Classification

According to the classification system widely used nowadays, SNe are classified into two types based on the absence (Type I) or presence (Type II) of hydrogen lines in their optical spectra

---

[2] According to the list of SNe published at http://www.cbat.eps.harvard.edu/lists/Supernovae.html by the Central Bureau for Astronomical Telegrams (CBAT).

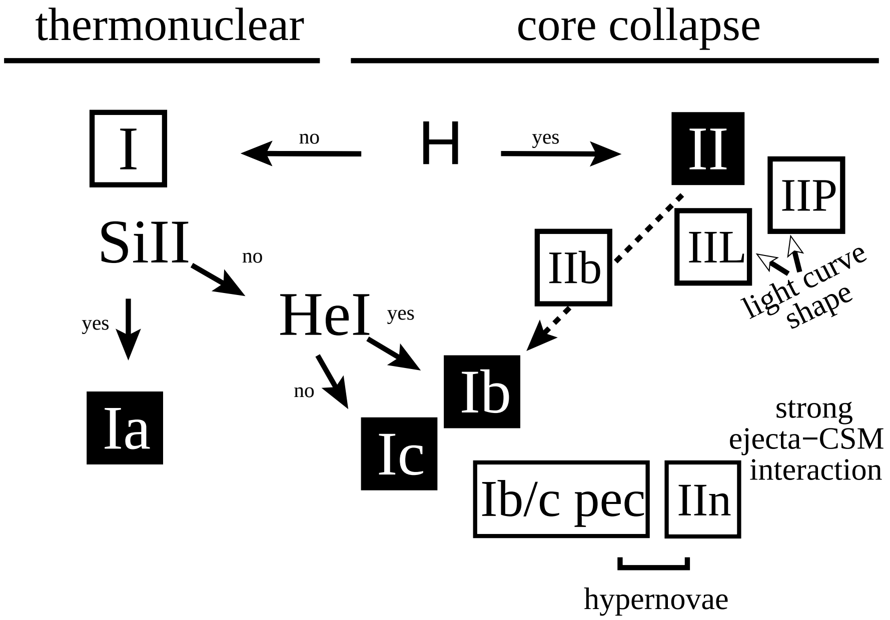

Figure 2.1: Diagram of supernova classification (from Turatto (2003)).

(Minkowski 1941). Later, as observational techniques and instruments had improved yielding high quality spectra and SN surveys reveal more events, more features can be noticed and the spectra can be subdivided further into several subclasses (See, e.g., Filippenko 1997; Turatto 2003, for detailed reviews).

Figure 2.1 shows a diagram of SNe classification. Type I SNe are divided into three subclasses SNe Ia, Ib, and Ic. The spectra of type Ia show an absorption feature at around λ6150Å which is the blueshifted Si II λ6355Å line which is not present in type Ib and Ic spectra. The spectra of type Ib can be distinguished from type Ic by strong He I lines, in particular the He I λ5876Å line. Spectra of different types of SNe are shown in figure 2.2. On the other hand, the light curves of type II SNe provide a criterium to subdivide them into two subclasses, *i.e.,* II-P and II-L. Type II-P SNe exhibit a pause in the decline of the luminosity shortly after maximum, thus forming a "plateau" in their lightcurve. In contrast to type II-P, type II-L SNe show a "linear" decline of the luminosity after the maximum without interruption (See figure 2.3). There are also some peculiar SNe. For example, type IIb SNe are found to have spectra which look similar to type II at early time but later on become similar to type Ib/c (Woosley et al. 1987). In addition, Schlegel (1990) proposed the type II-n, a new subclass of type II SNe. The letter "n" stands for "narrow" since type II-n SNe display narrow emission lines which are thought to be produced by the interaction of the SN ejecta with circumstellar material (most likely resulting from how mass loss by a stellar wind).

So far we have discussed only the classification of SNe based on their observed spectra and lightcurves. However, SNe can also be classified based on the underlying physical processes that cause the explosions. Baade & Zwicky (1934a) proposed the idea that a SN is powered by the release of a tremendous amount of gravitational binding energy when the progenitor star transforms into a neutron star which is considerably less massive and simultaneously ejects most of its mass into a rapidly expanding ($\sim 1000\,\mathrm{km\,s^{-1}}$) into a SNR (Baade & Zwicky 1934b).

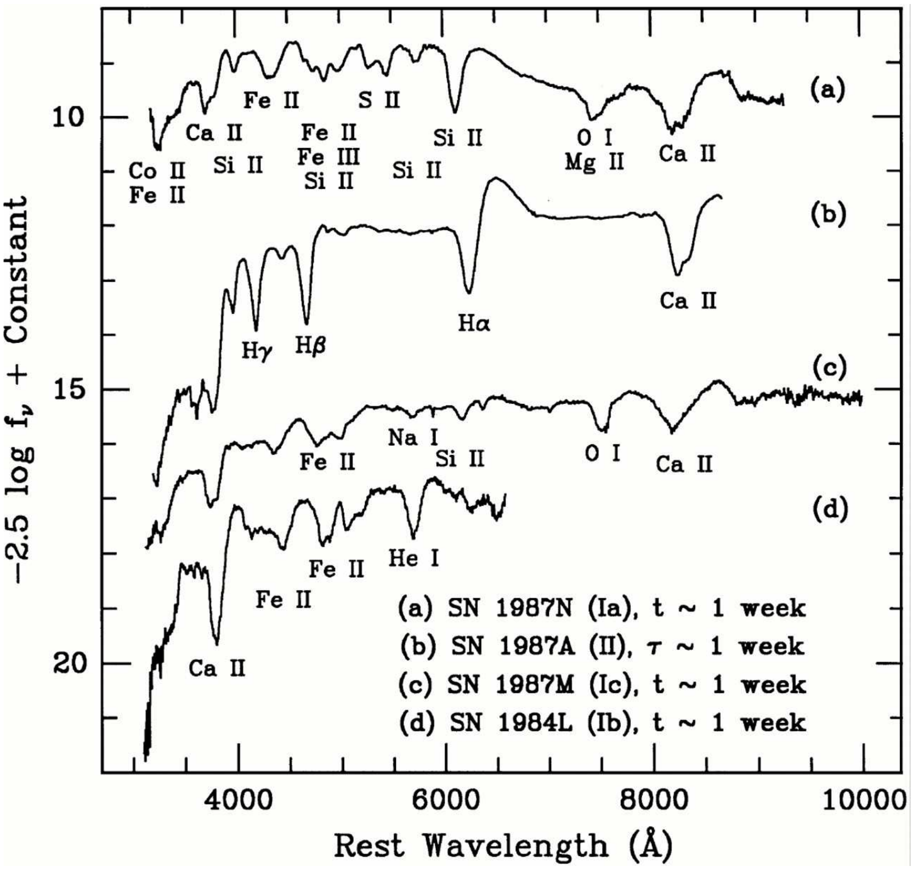

Figure 2.2: Spectra of four different types of supernovae at early time (∼ 1 week). Figure from Filippenko (1997).

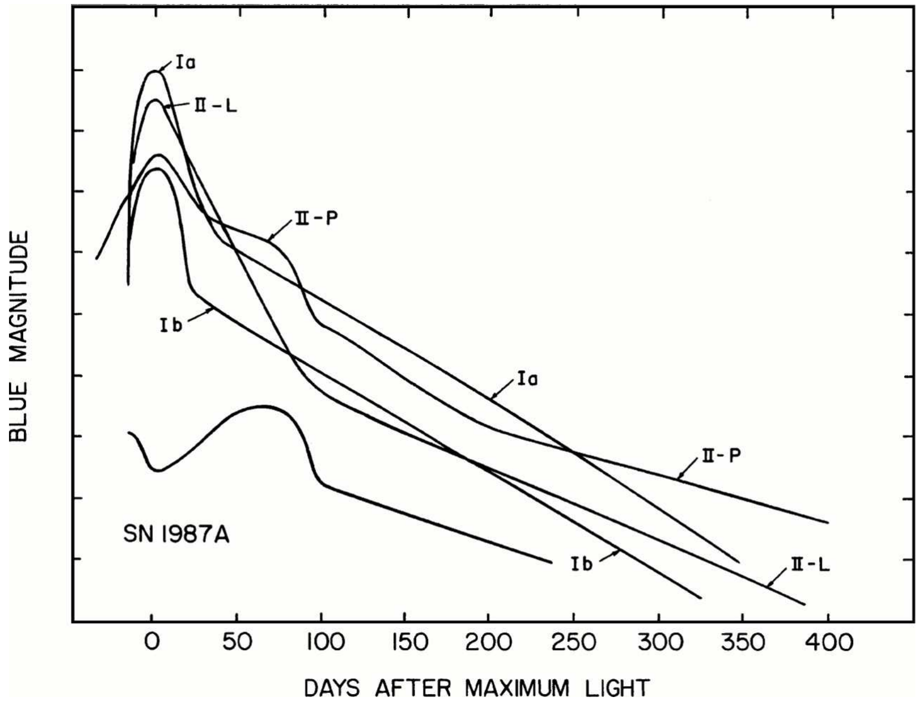

Figure 2.3: Schematic light curves of SNe Ia, Ib, II-L, II-P and SN 1987A. Figure from Wheeler (1990).

Another idea for the cause of a SN explosion was suggested by Hoyle & Fowler (1960). They proposed that the energy release by the thermonuclear explosion of a degenerate star can also drive a SN. Thus, based on these two physical processes, SNe can also be classified into two (theoretical) types, *i.e.,* thermonuclear SNe and CCSNe.

According to present knowledge, type Ia SNe result from the thermonuclear explosion of degenerate C/O white dwarfs. It is certain that an isolated white dwarf is not able to explode on its own. Thus, for an explosion to occur the white dwarf must gain mass from a companion star in a binary system. Once the mass of the white dwarf approaches the Chandrasekhar mass limit (M_{ch}), matter inside the white dwarf ignites resulting in a thermonuclear supersonic detonation or a subsonic deflagration flame. The thermonuclear runaway completely disrupts the star leaving no compact remnant behind. However, as no progenitor system has been observed up to now, the nature of such binary systems is still unknown. The donor star can either be a main sequence star or a white dwarf. Reviews on explosion models of type Ia SNe can be found in Hillebrandt & Niemeyer (2000) and Livio (2000).

The remaining classes, *i.e.,* SNe type Ib, Ic, and II are thought to be core collapse supernovae. The differences in their spectra originate from differences in the progenitor stars and their evolution. The progenitors of type Ib/c SNe must have lost thier hydrogen envelope during the evolution either stellar wind or mass exchange with a companion star (Wheeler & Levreault 1985; Woosley & Eastman 1997). In addition, for type Ic SNe, the progenitors must also have lost a substantial amount of the helium envelope. The progenitors of type II-P and II-L SNe differ only in the mass of their hydrogen envelope at the time of the explosion (Chevalier 1984).

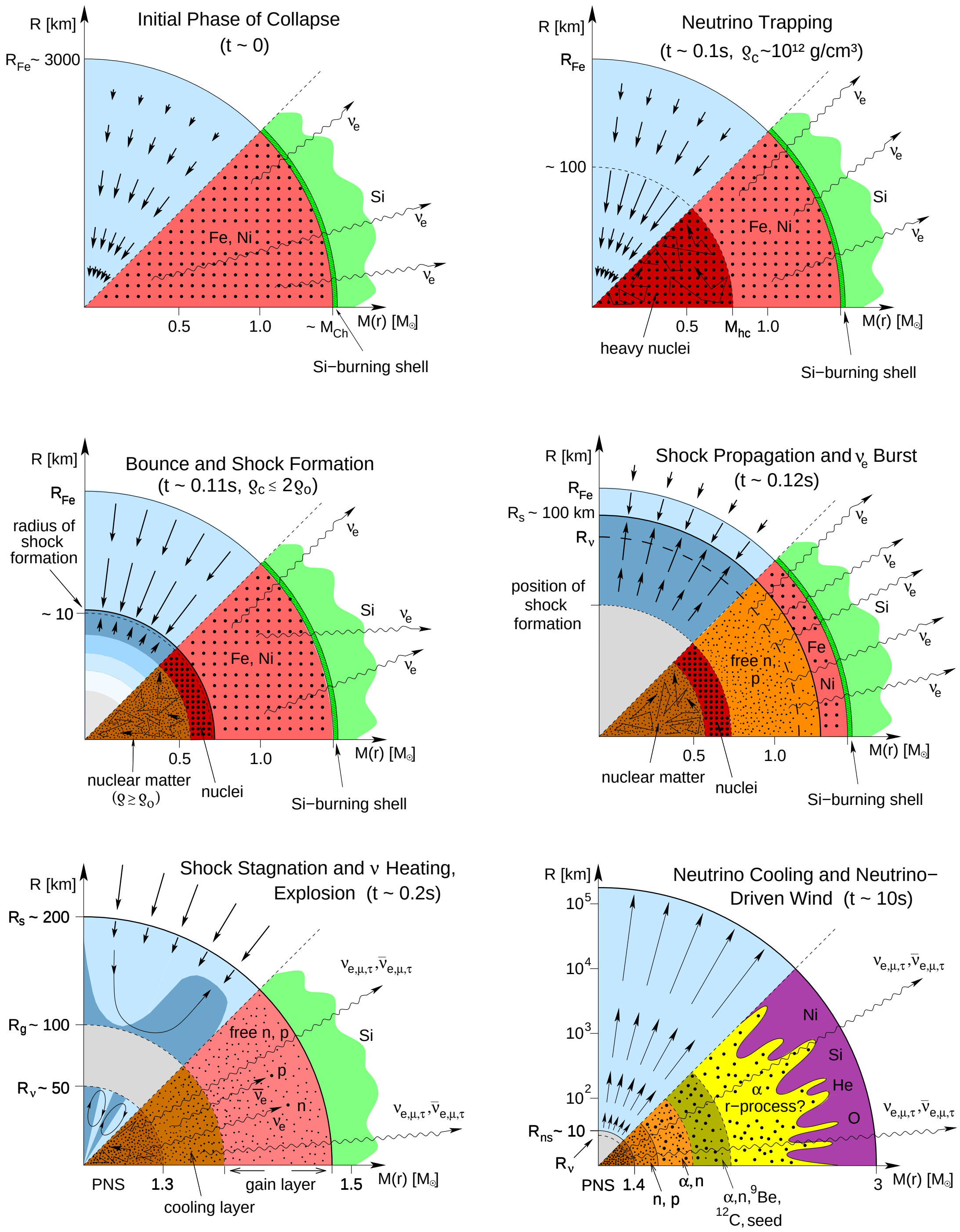
Initial Phase of Collapse
(t ~ 0)
R [km]
R_{Fe} ~ 3000
Fe, Ni
Si
ν_e
ν_e
ν_e
0.5
1.0
~ M_{Ch}
M(r) [$M_\odot$]
Si−burning shell
Neutrino Trapping
(t ~ 0.1s, ϱ_c~10^{12} g/cm³)
R [km]
R_{Fe}
~ 100
Fe, Ni
Si
ν_e
ν_e
ν_e
0.5
M_{hc}
1.0
M(r) [$M_\odot$]
heavy nuclei
Si−burning shell
Bounce and Shock Formation
(t ~ 0.11s, $\varrho_c \leq 2\varrho_0$)
R [km]
R_{Fe}
radius of shock formation
~ 10
Fe, Ni
Si
ν_e
ν_e
ν_e
0.5
1.0
M(r) [$M_\odot$]
nuclear matter
($\varrho \geq \varrho_0$)
nuclei
Si−burning shell
Shock Propagation and ν_e Burst
(t ~ 0.12s)
R [km]
R_{Fe}
R_s ~ 100 km
R_ν
position of shock formation
free n, p
Fe
Ni
Si
ν_e
ν_e
ν_e
ν_e
ν_e
0.5
1.0
M(r) [$M_\odot$]
nuclear matter
nuclei
Si−burning shell
Shock Stagnation and ν Heating,
Explosion (t ~ 0.2s)
R [km]
R_s ~ 200
R_g ~ 100
R_ν ~ 50
free n, p
p
$\bar{\nu}_e$
n
ν_e
Si
$\nu_{e,\mu,\tau}, \bar{\nu}_{e,\mu,\tau}$
$\nu_{e,\mu,\tau}, \bar{\nu}_{e,\mu,\tau}$
PNS
1.3
gain layer
1.5
M(r) [$M_\odot$]
cooling layer
Neutrino Cooling and Neutrino−
Driven Wind (t ~ 10s)
R [km]
10^5
10^4
10^3
10^2
R_{ns} ~ 10
R_ν
Ni
Si
He
O
α
r−process?
$\nu_{e,\mu,\tau}, \bar{\nu}_{e,\mu,\tau}$
$\nu_{e,\mu,\tau}, \bar{\nu}_{e,\mu,\tau}$
PNS
1.4
n, p
α, n
α,n,^{9}Be,
^{12}C, seed
3
M(r) [$M_\odot$]

Figure 2.4: Schematic representation of the evolutionary stages from stellar core collapse through the onset of the supernova explosion to the neutrino-driven wind during the neutrino-cooling phase of the proto-neutron star (PNS). The panels display the dynamical conditions in their upper half, with arrows representing velocity vectors. The nuclear composition as well as the nuclear and weak processes are indicated in the lower half of each panel. The horizontal axis gives mass information. M_{Ch} means the Chandrasekhar mass and M_{hc} the mass of the subsonically collapsing, homologous inner core. The vertical axis shows corresponding radii, with R_{Fe}, R_{s}, R_{g}, R_{ns}, and R_ν being the iron core radius, shock radius, gain radius, neutron star radius, and neutrinosphere, respectively. The PNS has maximum densities ρ above the saturation density of nuclear matter (ρ_0). Figures and description from Janka et al. (2007)

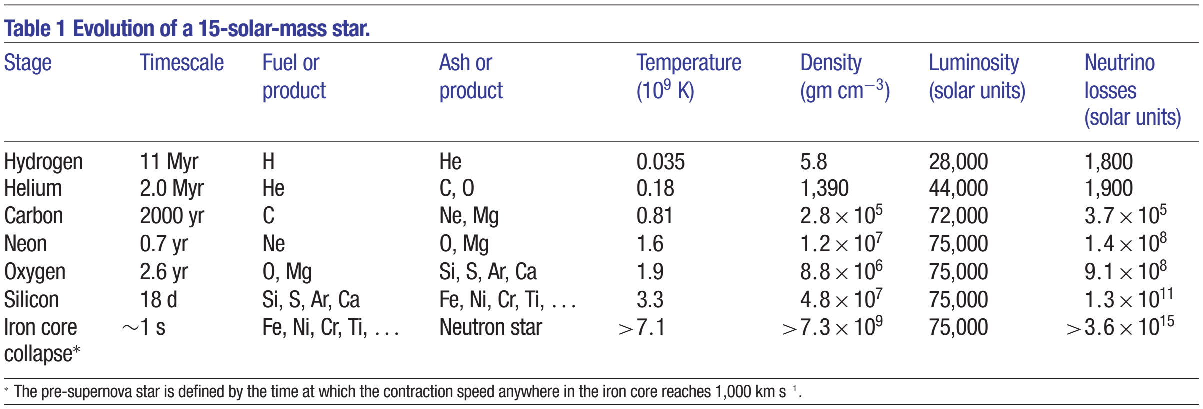

Table 1 Evolution of a 15-solar-mass star.

Stage	Timescale	Fuel or product	Ash or product	Temperature (10^9 K)	Density (gm cm^{-3})	Luminosity (solar units)	Neutrino losses (solar units)
Hydrogen	11 Myr	H	He	0.035	5.8	28,000	1,800
Helium	2.0 Myr	He	C, O	0.18	1,390	44,000	1,900
Carbon	2000 yr	C	Ne, Mg	0.81	2.8×10^5	72,000	3.7×10^5
Neon	0.7 yr	Ne	O, Mg	1.6	1.2×10^7	75,000	1.4×10^8
Oxygen	2.6 yr	O, Mg	Si, S, Ar, Ca	1.9	8.8×10^6	75,000	9.1×10^8
Silicon	18 d	Si, S, Ar, Ca	Fe, Ni, Cr, Ti, . . .	3.3	4.8×10^7	75,000	1.3×10^{11}
Iron core collapse*	~1 s	Fe, Ni, Cr, Ti, . . .	Neutron star	>7.1	$>7.3 \times 10^9$	75,000	$>3.6 \times 10^{15}$

* The pre-supernova star is defined by the time at which the contraction speed anywhere in the iron core reaches 1,000 km s^{-1}.

Table 2.1: Evolution of a 15-solar-mass star (from Woosley & Janka (2005)).

2.4 Core Collapse Supernovae Theory [3]

CCSNe are the final stage of massive stars with masses larger than approximately $8\,\mathrm{M}_\odot$. Here we will only discuss briefly the evolution of these stars shortly prior to the onset of core collapse. More details on the evolution of massive stars can be found in the review by Young & Arnett (2004). The structure of a massive star at the end of its life resembles an onion-shell like structure with elements of successively higher mass number being located incresingly closer towards the core. Stars with masses around 8–10 $\mathrm{M}_\odot$ end up with a O/Ne/Mg core after nuclear fusion reactions have ceased in their cores. However, burning can continue inside stars with masses higher than $10\,\mathrm{M}_\odot$. Elements inside the cores of these stars are converted into Fe-group elements, hence Fe-core, before nuclear reactions halt since the binding energy per nucleon peaks near ^{56}Fe, *i.e.,* conversion into heavier elements would be endothermic. Since we only study core collapse models of $15\,\mathrm{M}_\odot$ and $20\,\mathrm{M}_\odot$ here we will not further discuss O/Ne/Mg cores. A summary of the burning stages of a $15\,\mathrm{M}_\odot$ star is shown in Table 2.1. As the star loses pressure support when nuclear burning seizes inside its core, it begins to contract and heat up in the same way as during earlier evolutionary stages. The still burning Si shell layer dumps its products onto the Fe-core. Therefore, the mass of the Fe-core grows until it approaches the Chandrasekhar mass limit (Chandrasekhar 1939)

$$M_{ch} \simeq 5.8 Y_e^2 M_\odot. \tag{2.1}$$

At this stage, the pressure support provided by the degenerate and now also highly relativistic electrons inside the core is only marginal, *i.e.,* it is no longer sufficient to stabilize the core against radial pulsations as the adiabatic index of the core matter approaches the critical value of $\Gamma = 4/3$. Consequently, the core begins to collapse.

Initially the core collapses homologously. Furthermore electron captures on free protons of nuclei

$$p + e^- \longrightarrow n + \nu_e$$

occur inside the core reducing the lepton number, and therefore reducing also M_{ch}. The released neutrinos stream freely out of the core carrying energy with them. In addition, the Fe-group nuclei in the core can be photodisintegrated by enegetic photons consuming parts of the core's internal energy. These processes accelerate the collapse. At densities $\rho \gtrsim 3 \times 10^{12}$ $\mathrm{g\,cm^{-3}}$ the neutrino diffusion time scale becomes larger than the collapse timescale, $\tau_{\mathrm{diff}} > \tau_{\mathrm{coll}}$. Thus neutrinos are trapped inside the core. The Fe-core has now separated into a homologously and subsonically collapsing inner core and a supersonically falling outer core (Müller 1998) since the free-fall velocity increases with radius but the local sound speed, which is inversely proportional to the density, decreases with radius. The collapse continues until the central density of the core reaches nuclear matter density, where incompressibility of matter strongly increases. Consequently, infalling mass shells are stopped successively generating pressure waves in the inner core. The pressure waves propagate outwards and turn into a shock wave when they reach the sonic point.

---

[3] (See also, *e.g.,* Bethe 1990; Hillebrandt 1994; Mezzacappa 2005; Kotake et al. 2006; Janka et al. 2007, for reviews)

If the shock wave were to propagate all the way through the still supersonically infalling material, a supernova explosion would be the result. This scenario is called a "prompt" explosion. However, this is not the case as suggested by many numerical simulations (see Janka et al. 2007, and references therein). The shock wave loses a huge amount of its energy by photodisintegrating infalling material into free nucleons. The dissociation of infalling heavy nuclei which consist mainly of Fe group nuclei costs approximately 8.8 MeV per nucleon. This corresponds to an energy of $\sim 1.7 \times 10^{51}$ erg for dissociating $0.1\,M_{\odot}$ of infalling matter. Furthermore, free protons capture electrons generating electron neutrinos which stream freely outwards carrying energy with them. Eventually, the shock wave is unable to propagate further outwards and stalls. An important question then arises. How can we observe supernova explosions if the prompt mechanism fails to explode the star? Consequently, there must be a process (or processes) which supplies energy to the shock wave allowing it to continue its propagation and finally to eject the stellar envelope. We refer to this process as the shock revival mechanism.

Currently, the most favourable shock revival mechanism relies on neutrino heating process. Colgate & White (1966) proposed that if the vast amount of neutrinos ($\sim 10^{57}$) emitted by the newly formed PNS, which is initially very hot and not yet completely deleptonized due to neutrino trapping, could deposit a small fraction of energy ($\sim 1\%$) by the reactions

$$\begin{aligned} \nu_e + n &\longrightarrow e^- + p \\ \bar{\nu}_e + p &\longrightarrow e^+ + n \end{aligned}$$

in the region behind the stalled SN shockwave, the stalled shock can be revived leading to a successful explosion. However, neutrino cooling competes with neutrino heating in the region behind the stalled shock. Cooling by neutrino emission is more effective than heating in the region above the neutrinosphere, defined as the surface where the optical depth of neutrinos is close to 1, and inside the gain radius, defined as the radius where the cooling and heating rates are equal. Above the gain radius matter experiences a net heating. The success of the neutrino-driven explosion lies crucially in the competition between cooling and heating. Modelling accurately the neutrino-matter interactions is a challenge. In addition, multi-dimensional effects make the story even more complicated. Since the heating is more efficient near the gain radius than directly behind the stalled shock a negative entropy gradient establishes in this region, which makes the layer convectively unstable. The neutrino-driven convection generates hot high-entropy bubbles which rise, and deposit energy behind the shock. This process enhances the heating efficiency behind the stalled shock. Note that the advection timescale, which depends on the size of the gain region and the infall velocity of accreting matter, and heating timescale play an important role here. If the infall velocity is too high or the gain region is too narrow, the matter might not be heated sufficiently long enough and is advected through the gain radius before buoyancy forces can drive it outward again. There is also a convectively unstable layer inside the PNS. However, its role in aiding the explosion may be somewhat less important than the so-called "hot-bubble" region (Janka & Müller 1996) since it does not seem to enhance the neutrino luminosity by a large factor (Buras et al. 2006). Recently, another type of instability was discovered which also aids the explosion. The instability is named "Standing Accretion Shock Instability" (SASI; Blondin et al. 2003; Foglizzo & Tagger 2000; Foglizzo 2002). The stalled shock accreting the infalling matter is found to be unstable against non-radial perturbations. Linear analysis shows that the $\ell = 1, 2$ (dipole and quadrupole) modes have the fastest growth rates. The shock surface thus begins to pulsate which increases the time matter stays in the net heating region, thereby enhancing the heating efficiency.

Chapter 3

Numerical Techniques

3.1 Governing Equations

The fluid or gas in our study is assumed to be inviscid and compressible, and thus described by the Euler equations:

$$\frac{\partial \rho}{\partial t} + \boldsymbol{\nabla} \cdot (\rho \boldsymbol{u}) = 0, \tag{3.1}$$

$$\frac{\partial \rho \boldsymbol{u}}{\partial t} + \boldsymbol{\nabla} \cdot (\boldsymbol{u} \otimes (\rho \boldsymbol{u})) + \boldsymbol{\nabla} p = 0, \tag{3.2}$$

$$\frac{\partial \rho e}{\partial t} + \boldsymbol{\nabla} \cdot (\boldsymbol{u}(\rho e + p)) = 0, \tag{3.3}$$

where ρ is the density, $\boldsymbol{u}$ the fluid velocity, p the pressure, $e = u^2/2 + \epsilon$ the specific total energy, and ϵ the specific internal energy. The equations are written in conservation form representing the conservation of mass, momentum, and energy, respectively. For an astrophysical application, self-gravity of the fluid often plays an important role and must be included as source terms on the right hand side of the momentum and energy conservation equations. The two equations then take the form

$$\frac{\partial \rho \boldsymbol{u}}{\partial t} + \boldsymbol{\nabla} \cdot (\boldsymbol{u} \otimes (\rho \boldsymbol{u})) + \boldsymbol{\nabla} p = -\rho \boldsymbol{\nabla} \Phi, \tag{3.4}$$

$$\frac{\partial \rho e}{\partial t} + \boldsymbol{\nabla} \cdot (\boldsymbol{u}(\rho e + p)) = -\rho \boldsymbol{u} \cdot \boldsymbol{\nabla} \Phi, \tag{3.5}$$

where Φ is the gravitational potential. This gravitational potential is determined by the density distribution and therefore is time-dependent. The gravitational potential is solved via the Poisson equation

$$\nabla^2 \Phi = 4\pi G \rho \tag{3.6}$$

where G is the gravitational constant. Equations (3.1), (3.4), and (3.5) are the principal equations in our calculation. However, in general, additional source terms can be present on the right hand sides of the momentum and energy equation. In particular, for a core-collapse supernova explosion simulation powered by the neutrino mechanism, one needs to take into account the momentum and energy change of matter due to interactions with neutrinos. As a result the terms $\boldsymbol{Q_M}$ and $(Q_E + \boldsymbol{u} \cdot \boldsymbol{Q_M})$ are added to the right hand side of the momentum and energy equation, respectively. The final ingredient in solving this set of equations is the equation of state (EoS), which describes the relation between state variables, e.g., the fluid pressure p as a function of ρ and e.

The Euler equations with self-gravity in spherical coordinates take the form

$$\frac{\partial \rho}{\partial t} + \frac{1}{r^2}\frac{\partial}{\partial r}(r^2[\rho u_r]) + \frac{1}{r\sin\theta}\frac{\partial}{\partial\theta}(\sin\theta[\rho u_\theta]) + \frac{1}{r\sin\theta}\frac{\partial}{\partial\phi}[\rho u_\phi] = 0, \tag{3.7}$$

$$\begin{aligned}\frac{\partial \rho u_r}{\partial t} &+ \frac{1}{r^2}\frac{\partial}{\partial r}(r^2[\rho u_r^2]) + \frac{1}{r\sin\theta}\frac{\partial}{\partial\theta}(\sin\theta[\rho u_r u_\theta]) + \frac{1}{r\sin\theta}\frac{\partial}{\partial\phi}[\rho u_r u_\phi] \\ &+ \left\{-\frac{\rho u_\theta^2}{r} - \frac{\rho u_\phi^2}{r}\right\} + \frac{\partial p}{\partial r} = -\rho\frac{\partial \Phi}{\partial r},\end{aligned} \tag{3.8}$$

$$\begin{aligned}\frac{\partial \rho u_\theta}{\partial t} &+ \frac{1}{r^2}\frac{\partial}{\partial r}(r^2[\rho u_r u_\theta]) + \frac{1}{r\sin\theta}\frac{\partial}{\partial\theta}(\sin\theta[\rho u_\theta^2]) + \frac{1}{r\sin\theta}\frac{\partial}{\partial\phi}[\rho u_\theta u_\phi] \\ &+ \left\{\frac{\rho u_r u_\theta}{r} - \frac{\rho u_\phi^2\cos\theta}{r\sin\theta}\right\} + \frac{1}{r}\frac{\partial p}{\partial\theta} = -\frac{\rho}{r}\frac{\partial \Phi}{\partial\theta},\end{aligned} \tag{3.9}$$

$$\begin{aligned}\frac{\partial \rho u_\phi}{\partial t} &+ \frac{1}{r^2}\frac{\partial}{\partial r}(r^2[\rho u_r u_\phi]) + \frac{1}{r\sin\theta}\frac{\partial}{\partial\theta}(\sin\theta[\rho u_\theta u_\phi]) + \frac{1}{r\sin\theta}\frac{\partial}{\partial\phi}[\rho u_\phi^2] \\ &+ \left\{\frac{\rho u_r u_\phi}{r} + \frac{\rho u_\theta u_\phi\cos\theta}{r\sin\theta}\right\} + \frac{1}{r\sin\theta}\frac{\partial p}{\partial\phi} = -\frac{\rho}{r\sin\theta}\frac{\partial \Phi}{\partial\phi},\end{aligned} \tag{3.10}$$

$$\begin{aligned}\frac{\partial \rho e}{\partial t} &+ \frac{1}{r^2}\frac{\partial}{\partial r}(r^2[u_r(\rho e + p)]) + \frac{1}{r\sin\theta}\frac{\partial}{\partial\theta}(\sin\theta[u_\theta(\rho e + p)]) + \frac{1}{r\sin\theta}\frac{\partial}{\partial\phi}[u_\phi(\rho e + p)] \\ &= -\rho\left(u_r\frac{\partial \Phi}{\partial r} + \frac{u_\theta}{r}\frac{\partial \Phi}{\partial\theta} + \frac{u_\phi}{r\sin\theta}\frac{\partial \Phi}{\partial\phi}\right).\end{aligned} \tag{3.11}$$

Note that the terms in curly brackets, called fictitious forces, arise since we employ a curvilinear coordinate system.

Solving these nonlinear hyperbolic partial differential equations we employ the finite volume method where the computational domain is discretized into volume elements or cells. Our computer code, PROMETHEUS, developed by Bruce Fryxell and Ewald Müller (Fryxell et al. 1991; Müller et al. 1991a,b), is an explicit finite-volume Eulerian hydrodynamic code which integrates the equations of multidimensional hydrodynamics using the piecewise parabolic method (PPM; Collela & Woodward 1984) for the reconstruction scheme and the dimensional splitting method of Strang (1968) to treat the multi-dimensionality of the problem. The Riemann solver used in the code is based on the Riemann solver for real gases of Colella & Glaz (1985). Inside grid cells with strong grid-aligned shocks fluxes computed from the Riemann solver are replaced by the AUSM+ fluxes of Liou (1996) in order to prevent odd-even decoupling (Quirk 1994).

3.2 The Yin-Yang Grid

3.2.1 Grid Geometry and Transformations

The Yin-Yang grid configuration is shown in Fig. 3.1. Both the Yin and the Yang grid are simply a part of a usual spherical polar grid and are identical in geometry. The angular domain

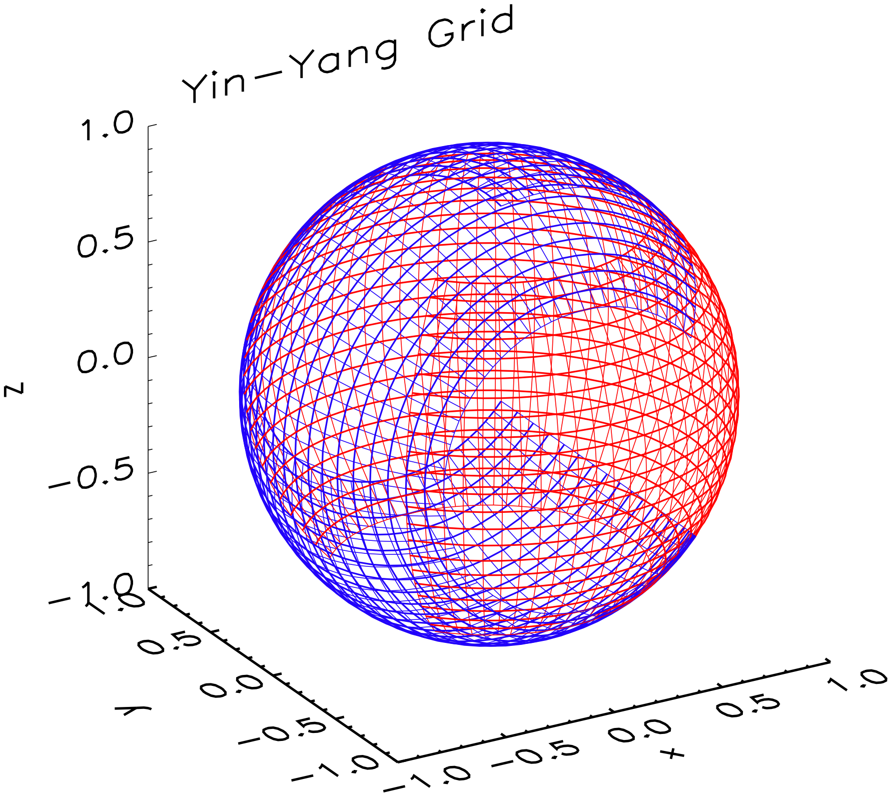
Yin-Yang Grid
1.0
0.5
0.0
-0.5
-1.0
z
1.0
0.5
0.0
-0.5
-1.0
y
-1.0
-0.5
0.0
0.5
1.0
x

Figure 3.1: An axis-free Yin-Yang grid configuration plotted on a spherical surface. Both the Yin (red) and Yang (blue) grid are the low latitude part of the normal spherical polar grid and are identical in geometry. The Yang grid is obtained from the Yin grid by two rotations, and vice versa.

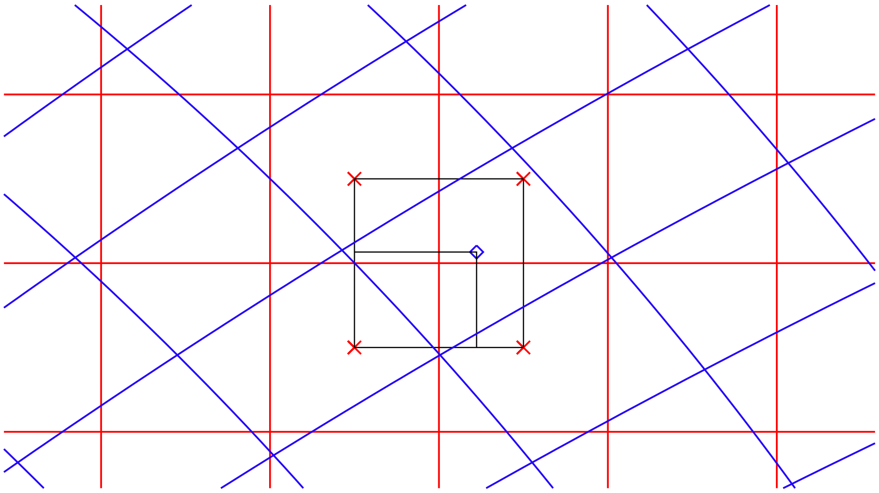

Figure 3.2: A Mercator projection of an overlap region of the Yin-Yang grid. In case of bi-linear interpolation, four neighboring values of the underlying grid (red) will be used to determine the zone-centered value of a ghost zone in the grid on top (blue). The interpolation coefficients are determined by the relative distances, denoted by black lines, between the interpolation point (diamond) and the four neighboring points (crosses).

of each grid patch is given by

$$\theta = \left[\frac{\pi}{4} - \delta,\, \frac{3\pi}{4} + \delta\right] \,\cap\, \phi = \left[-\frac{3\pi}{4} - \delta,\, \frac{3\pi}{4} + \delta\right] \tag{3.12}$$

where θ and ϕ are the colatitude and azimuth, respectively. Note that it is necessary to add at least one extra buffer grid zone to both angular directions in order to ensure an appropriate overlap of the grids. The angular width δ of this buffer zone depends on the grid resolution, *i.e.*, $\delta \equiv \Delta\theta = \Delta\phi$, where for simplicity we assumed equal angular spacing in θ- and ϕ-direction. The angular domain is hereby extended by 2δ in both angular directions. The Yin and Yang grid are patched together in a specific manner forming a spherical shell with a small overlapping region covering approximately 6% of a sphere's surface. Stacking up Yin-Yang shells in radial direction results in a 3D grid that is identical to the usual spherical polar grid in radial direction. It is obvious that, unlike in the case of the spherical polar grid, the problematic high latitude sections of the sphere are avoided, and the angular zoning is almost equidistant.

The Cartesian coordinates

$$(x^{(n)}, y^{(n)}, z^{(n)}) = (r\sin\theta^{(n)}\cos\phi^{(n)},\, r\sin\theta^{(n)}\sin\phi^{(n)},\, r\cos\theta^{(n)}) \tag{3.13}$$

corresponding to the Yin grid, denoted by a superscript (n), and the Cartesian coordinates

$$(x^{(e)}, y^{(e)}, z^{(e)}) = (r\sin\theta^{(e)}\cos\phi^{(e)},\, r\sin\theta^{(e)}\sin\phi^{(e)},\, r\cos\theta^{(e)}) \tag{3.14}$$

corresponding to the Yang grid, denoted by a superscript (e), are related to each other through the transformation

$$\begin{pmatrix} x^{(e)} \\ y^{(e)} \\ z^{(e)} \end{pmatrix} = M \begin{pmatrix} x^{(n)} \\ y^{(n)} \\ z^{(n)} \end{pmatrix} \tag{3.15}$$

where

$$M = \begin{pmatrix} -1 & 0 & 0 \\ 0 & 0 & 1 \\ 0 & 1 & 0 \end{pmatrix}. \tag{3.16}$$

This Yin-Yang coordinate transformation can also be considered as two subsequent rotations. Accordingly, the transformation matrix M can be written as $R_x(90^\circ)\, R_z(180^\circ)$, where R_x and R_z are the transformation matrices of rotations by 90° around the x-axis and by 180° around the z-axis in counterclockwise direction, respectively. For the inverse transformation matrix $M^{-1} = M$ holds.

The relation between the spherical coordinates of the Yin and Yang grid patches can be derived directly from the transformation matrix M. Because the Yin-Yang coordinate transformation involves only rotations, it implies that the radial coordinate is identical on the Yin and the Yang grid. The angular coordinates transform as

$$\theta^{(e)} = \arccos\left(\sin\theta^{(n)} \sin\phi^{(n)}\right), \tag{3.17}$$

$$\phi^{(e)} = \arctan\left(\frac{\cos\theta^{(n)}}{-\sin\theta^{(n)}\cos\phi^{(n)}}\right). \tag{3.18}$$

Note that the inverse transformation has the same form as (3.17) and (3.18) but exchanging the (grid) superscripts.

Vector components in spherical coordinates transform according to

$$\begin{pmatrix} v_r^{(e)} \\ v_\theta^{(e)} \\ v_\phi^{(e)} \end{pmatrix} = P \begin{pmatrix} v_r^{(n)} \\ v_\theta^{(n)} \\ v_\phi^{(n)} \end{pmatrix} \tag{3.19}$$

where

$$P = \begin{pmatrix} 1 & 0 & 0 \\ 0 & -\sin\phi^{(e)}\sin\phi^{(n)} & -\cos\phi^{(n)}/\sin\theta^{(e)} \\ 0 & \cos\phi^{(n)}/\sin\theta^{(e)} & -\sin\phi^{(e)}\sin\phi^{(n)} \end{pmatrix} \tag{3.20}$$

is the vector transformation matrix. When switching (grid) superscripts (e) and (n) in matrix P, the inverse vector transformation matrix is obtained. For a detailed derivation of the transformation matrix P, we refer to section 3 of Kageyama & Sato (2004). Note that the vector transformation matrix P is singular at $\sin\theta^{(e)} = 0$, but this singular point is rectifiable. In practice, one can always decompose vectors into their Cartesian components and perform the corresponding transformation.

3.2.2 Implementation

Firstly, the Yin-Yang grid needs to be constructed. Since both the Yin and the Yang grid are part of a spherical polar grid an analogous spatial discretization in angular direction can be used. For example, using the discretization formulae (1.2) and (1.3), the θ and ϕ coordinates of the zone center of an angular zone (j, k) of a Yin-Yang grid, having N_θ zones in θ-direction and

N_ϕ zones in ϕ-direction, are given by

$$\theta_j = \theta_{min} + j \cdot \frac{\Delta\theta}{2} \quad \text{for} \quad 1 \leq j \leq N_\theta, \tag{3.21}$$

$$\phi_k = \phi_{min} + k \cdot \frac{\Delta\phi}{2} \quad \text{for} \quad 1 \leq k \leq N_\phi, \tag{3.22}$$

where

$$\Delta\theta = \frac{\theta_{max} - \theta_{min}}{N_\theta}, \tag{3.23}$$

$$\Delta\phi = \frac{\phi_{max} - \phi_{min}}{N_\phi} \tag{3.24}$$

are the respective angular grid spacings.

The range of values for the colatitude θ and the azimuth angle ϕ are as given in (3.12), and for simplicity we set $\Delta\theta = \Delta\phi$. In radial direction no modification is required. The geometric property of the Yin-Yang grid allows us to make use of the coordinate arrays r_i, θ_j, and ϕ_k twice by enforcing the same grid resolution for both grid patches. This approach avoids doubling the coordinate arrays.

Only simple modifications are needed concerning the data and program structure. Arrays with three spatial indices, e.g., i, j, and k, need an extra grid index, say, l. For example, the array for the density field will be $\rho(i, j, k, l)$ instead of $\rho(i, j, k)$. As a consequence any triple loop running over indices i, j, and k in the program becomes a fourfold loop over i, j, k, and l instead. Otherwise, the Yin-Yang grid allows one to exploit without any further modification any already implemented finite-volume scheme in spherical coordinates to solve the equations of hydrodynamics.

Different from the spherical polar grid, the Yin-Yang grid requires no boundary conditions in angular directions. Each grid patch communicates with its neighboring patch using information from ghost zones that is obtained by interpolation of data between internal grid zones of the neighboring grid patch. Interpolation is only required in the two angular coordinates as the radial part of the Yin-Yang grid is identical to that of a spherical polar grid. It is straightforward to determine the corresponding interpolation coefficients. The mapping of vector quantities between the Yin and Yang grid patches requires an additional step. After interpolating the vector components they must be transformed according to the transformation given in Eq. (3.19) from the Yin to the Yang angular coordinate system, and vice versa.

We tested two interpolation procedures. In the first one all primitive state variables (density, velocity, energy, pressure, temperature, abundances) are interpolated ignoring the resulting small thermodynamic inconsistencies. In the second procedure, we only interpolate the conserved quantities (density, momentum, total energy, and abundances), and compute the velocity and the remaining thermodynamic state variables consistently via the equation of state. Both procedures produce very similar results which differ at the level of the discretization errors. As the second procedure is more consistent we use it as the standard one in our code.

An example of overlapping situations which are encountered when using a Yin-Yang grid is shown in Fig. 3.2. For simplicity, we use bi-linear interpolation in order to prevent unwanted oscillation. Because the grid patches are fixed in both angular directions the interpolation coefficients for each ghost zone need to be calculated only once per simulation at the initialization step. After initialization, the coefficient map is stored in an array for later usage. Moreover, the symmetry property of the Yin-Yang transformation allows one to make use of the interpolation coefficients twice for both grids.

Because the Yin-Yang grid is an overlapping grid integral quantities such as the total mass or total energy on the computational domain cannot be obtained by just summing local quantities from every grid cells. Doing so will result in counting the contributions in the overlapping region twice. To circumvent this problem, weights are given to each grid zone during the summation. Suppose a grid zone has an overlapping volume fraction α the cell will receive a weight $w = 1.0 - 0.5\alpha$. Zones in the non-overlapping region receive the weight of 1.0, i.e., the entire zone contributes to the integral while, on the other hand, zones that are fully contained within the overlapping region have a weight 0.5. The volume fraction α does not depend on the radial coordinate and can be thought of as an area fraction since the grid patches are not offset in radial direction. Prior to the area integration, one needs to determine for each zone interface of the underlying grid the points where the interface is intersected by the boundary lines of the other grid, e.g., points on the Yin grid intersected by the boundary lines of the Yang grid. The intersection points can be determined using the Yin-Yang coordinate transformation in (3.17) and (3.18), respectively. The integration in the overlapping area is then carried out using the trapezoidal method. This procedure is also described in Peng et al. (2006). Once the area or volume fraction α is calculated, the weights for each cell are obtained easily. Note that these weights need to be calculated only at the initialization step, and are stored for later usage in a coefficient map $w(j, k)$, where j and k are the indices referring to the θ and ϕ coordinates, respectively. The coefficient map can be applied to both grids without any modification. Using the above described approach, the volume or surface area of the grids can be calculated with an accuracy up to machine precision.

3.3 Self-gravity Solver

The 3D Newtonian gravitational potential is computed from Poisson's equation in its integral form using an expansion into spherical harmonics as described in Müller & Steinmetz (1995). Because the algorithm of these authors is based on a (single) spherical polar grid the density on the Yin-Yang sphere has to be interpolated onto an auxiliary spherical polar grid. The interpolation used is first-order accurate, and due to the simplicity of the Yin-Yang grid configuration has to be performed only in the two angular dimensions. Concerning the resolution of the auxiliary grid, it is natural to employ the same grid resolution as that used for the Yin-Yang grid in all three spatial dimensions. The orientation of the auxiliary grid can be chosen freely in principle. However, it is convenient to align it with one of the two grid patches (the Yin-grid in our case). Once the density is interpolated onto the auxiliary spherical grid we compute the gravitational potential, as suggested by Müller & Steinmetz (1995), at zone interfaces instead of at zone centers on both the Yin and Yang grid. The gravitational acceleration at zone centers can then be obtained by central differencing the potential. Note that the interpolation coefficients for the density need to be calculated only once per simulation, because both the auxiliary grid and the Yin-Yang grid are fixed in angular directions. In addition, all angular weights, Legendre polynomials, and their integrals required for the calculation of the gravitational potential are stored after the initialization step for later usage.

It is also possible to directly calculate the gravitational acceleration at zone centers. The gravitational potential is given by (see Eqs. (5), (6) and (7) in Müller & Steinmetz (1995))

$$\Phi(r,\theta,\phi) = -G\sum_{l=0}^{\infty}\frac{4\pi}{2l+1}\sum_{m=-l}^{l} Y^{lm}(\theta,\phi)\left(\frac{1}{r^{l+1}}C^{lm}(r) + r^l D^{lm}(r)\right) \tag{3.25}$$

with

$$C^{lm}(r) = \int\limits_{4\pi} d\,\Omega' Y^{lm*}(\theta',\phi') \int\limits_{0}^{r} dr' r'^{l+2}\rho(r',\theta',\phi')\,, \tag{3.26}$$

$$D^{lm}(r) = \int\limits_{4\pi} d\,\Omega' Y^{lm*}(\theta',\phi') \int\limits_{r}^{\infty} dr' r'^{1-l}\rho(r',\theta',\phi')\,, \tag{3.27}$$

where Y^{lm} and Y^{lm*} are the spherical harmonics and their complex conjugates, ρ is the density, and $d\,\Omega \equiv \sin\theta\, d\theta\, d\phi$. The gravitational acceleration in radial direction is then

$$\begin{aligned}&\frac{\partial}{\partial r}\Phi(r,\theta,\phi) = \\ &-G\sum_{l=0}^{\infty}\frac{4\pi}{2l+1}\sum_{m=-l}^{l} Y^{lm}(\theta,\phi)\frac{d}{dr}\left(\frac{1}{r^{l+1}}C^{lm}(r) + r^l D^{lm}(r)\right)\,.\end{aligned} \tag{3.28}$$

Writing the radial derivative in Eq. (3.28) as

$$\begin{aligned}\frac{d}{dr}\left(\frac{1}{r^{l+1}}C^{lm}(r) + r^l D^{lm}(r)\right) &= \frac{1}{r^{l+1}}\frac{d}{dr}C^{lm}(r) - \frac{l+1}{r}\cdot\frac{1}{r^{l+1}}C^{lm}(r) \\ &+ r^l\frac{d}{dr}D^{lm}(r) + \frac{l}{r}\cdot r^l D^{lm}(r)\,,\end{aligned} \tag{3.29}$$

and noticing that the first and third term on the right hand side of this expression cancel each other because of the identities

$$\frac{d}{dx}\int\limits_{0}^{x} f(x')dx' = f(x) \tag{3.30}$$

and

$$\frac{d}{dx}\int\limits_{x}^{\infty} f(x')dx' = -f(x) \tag{3.31}$$

the gravitational acceleration in radial direction becomes

$$\begin{aligned}\frac{\partial}{\partial r}\Phi(r,\theta,\phi) = &- G\sum_{l=0}^{\infty}\frac{4\pi}{2l+1}\sum_{m=-l}^{l} Y^{lm}(\theta,\phi) \\ &\left(-\frac{l+1}{r}\cdot\frac{1}{r^{l+1}}C^{lm}(r) + \frac{l}{r}\cdot r^l D^{lm}(r)\right)\,.\end{aligned} \tag{3.32}$$

The corresponding expressions for the gravitational acceleration in the two angular directions are easy to obtain since the spherical harmonics Y^{lm} are the only angular-dependent terms in

Eq. (3.25). Therefore, we only need to consider the partial derivatives of the spherical harmonics with respect to the θ and ϕ coordinates. As the spherical harmonics are given by

$$Y^{lm}(\theta,\phi) = N^{lm} P^{lm}(\cos\theta) e^{im\phi}\,, \tag{3.33}$$

where N^{lm} is the normalization constant and P^{lm} the associated Legendre polynomial, one finds

$$\frac{\partial}{\partial\theta} Y^{lm}(\theta,\phi) = N^{lm} e^{im\phi} \frac{d}{d\theta} P^{lm}(\cos\theta) \tag{3.34}$$

and

$$\frac{\partial}{\partial\phi} Y^{lm}(\theta,\phi) = im Y^{lm}(\theta,\phi). \tag{3.35}$$

The derivatives of the associated Legendre polynomials are easily obtained using the recurrence formula

$$(x^2-1)\frac{d}{dx} P_l^m(x) = lxP_l^m(x) - (l+m)P_{l-1}^m(x)\,. \tag{3.36}$$

Thus, one finds for the gravitational acceleration in the angular directions

$$\frac{1}{r}\frac{\partial}{\partial\theta}\Phi(r,\theta,\phi) = -\frac{G}{r}\sum_{l=0}^{\infty}\frac{4\pi}{2l+1} \sum_{m=-l}^{l} N^{lm} e^{im\phi}\frac{d}{d\theta}P^{lm}(\cos\theta) \left(\frac{1}{r^{l+1}}C^{lm}(r) + r^l D^{lm}(r)\right) \tag{3.37}$$

and

$$\frac{1}{r\sin\theta}\frac{\partial}{\partial\phi}\Phi(r,\theta,\phi) = -\frac{G}{r\sin\theta} \sum_{l=0}^{\infty}\frac{4\pi}{2l+1}\sum_{m=-l}^{l} im Y^{lm}(\theta,\phi) \left(\frac{1}{r^{l+1}}C^{lm}(r) + r^l D^{lm}(r)\right)\,. \tag{3.38}$$

Obviously, the expressions for three components of the gravitational acceleration (see Eqs. (3.32), (3.37), and (3.38)) are similar to that for the gravitational potential itself (see Eq. (3.25)). Hence, besides computing derivatives of Legendre polynomials, our extended Poisson solver can provide without much additional effort both the gravitational potential and the corresponding acceleration.

Usage of the analytic expressions for the gravitational acceleration avoids the errors arising from the numerical differentiation of the gravitational potential. However, tests show that the results obtained using either the gravitational potential computed with the "standard" Poisson solver and subsequent numerical differentiation or directly the gravitational acceleration provided by the extended Poisson solver differ only very slightly (see next chapter). Thus, we decided to stick to the "standard" Poisson solver in our simulations and compute the gravitational acceleration by numerical differentiation, as it requires no modification of our code.

3.4 Additional Physics

We divided our simulations into two phases: the explosion simulation and the long-time shock propagation simulation. Each phase is treated with a different set of additional physics as necessary to follow the evolution. The explosion phase considers the supernova evolution starting from approximately 10-15 ms after bounce until 1.4 s after bounce. At this stage, the supernova shockwave locates roughly at 15000 km. The long-time simulation is then a continuation from 1.4 s after bounce until the supernova shock reaches the surface of the progenitor's star which is roughly at the radius of 3.3×10^{13} cm.

3.4.1 Explosion Simulation

In our supernova simulations, we employ the tabulated EoS of Janka & Müller (1996) to describe the stellar fluid. It includes arbitarily degenerate and arbitarily relativistic electrons and positrons, photons, and four predefined nuclear species (n, p, α, and a representative Fe-group nucleus) in nuclear statistical equilibrium. The dense inner core of the proto-neutron star (PNS) is excised and replaced by a point mass at the coordinate origin. The cooling of the PNS is then prescribed by neutrino emission properties as boundary condition at the inner grid boundary. The contraction of the PNS is mimicked by a contracting inner grid boundary and a radial grid movement. "Ray-by-ray" neutrino transport and neutrino-matter interactions are approximated as in Scheck et al. (2006) by radial integration of the one-dimensional (spherical), grey transport equation for all angular grid directions (θ, ϕ) independently. This approach allows for angular variations of the neutrino fluxes. We take into account the dominant general relativistic effects by replacing the monopole term of the Newtonian gravitational potential by the potential described in Scheck et al. (2006) and Arcones et al. (2007). The code treats advection of nuclear species by employing the Consistent Multi-fluid Advection (CMA) scheme of Plewa & Müller (1999).

In addition, to follow approximately the explosive nucleosynthesis, we solve a small alpha-reactions network, similar to the network described in Kifonidis et al. (2003), consisting of the 10 α-nuclei: ^{4}He, ^{12}C, ^{16}O, ^{20}Ne, ^{24}Mg, ^{28}Si, ^{40}Ca, ^{44}Ti, ^{56}Ni, and an additional tracer nucleus (discarding ^{32}S, ^{36}Ar, ^{48}Cr, and ^{52}Fe). The two gaps between ^{28}Si - ^{40}Ca and ^{44}Ti - ^{56}Ni are bridged by combining the intermediate reactions steps and taking the slowest reaction rate of the intermediate reaction. The tracer nucleus is produced via the reaction $^{44}\mathrm{Ti}(3\alpha,\gamma)^{56}\mathrm{Ni}$ within grid cells whose electron fraction Y_e is below 0.49. This allows us to keep track of element formation in neutron-rich regions. The network is solved within grid cells whose temperature is within the range of $10^8\,\mathrm{K} - 8 \times 10^9\,\mathrm{K}$. We assume that all nuclei are photo-disintegrated into α-particles at temperatures above 8×10^9 K. We also neglect feedback from the network to the EOS and the hydrodynamic flow.

3.4.2 Long-time Shock Propagation Simulation

To follow the propagation of the SN shock wave until very late time, we map our computed data at the end of the explosion phase onto a new computational grid. We neglected the neutrino transport as it becomes unimportant, but still consider nucleosysthesis and Newtonian self-gravity. The EoS used for this simulation is based on the tabulated EoS by Timmes & Swesty (2000). It considers contributions of an arbitarily degenerate and relativistic electron-positron gas and a photon gas. It also considers the contribution of ideal Boltzmann gases consisting of 12 nuclear species: n, p, ^{4}He, ^{12}C, ^{16}O, ^{20}Ne, ^{24}Mg, ^{28}Si, ^{40}Ca, ^{44}Ti, ^{56}Ni. During the course of the simulation, we move the inner grid boundary out to a new radius whenever the radius of the inner grid boundary becomes less than 2% of the minimum shock radius reducing the total number of radial grid zones. Moving the inner grid boundary to a larger radius helps relaxing the restrictive CFL timestep and allows us to follow the evolution to very late time ($\sim$hours or days) with reasonable computational time.

Chapter 4

Test Suites

In this chapter, we present results from tests to ensure that the Yin-Yang grid is working properly together with the hydrodynamic and self-gravity parts of the code.

4.1 Sod Shock Tube

The first problem of our test suite is the planar Sod shock tube problem, a classical hydrodynamic test problem (Sod 1978). We simulated this (1D Cartesian) flow problem using spherical coordinates and the Yin-Yang grid. The initial state consists of two constant states given by

$$(\rho, p, v_x) = \begin{cases} (1.0, 1.0, 0.0) & \text{if } x^{(n)} > 0.4\,\mathrm{cm} \\ (0.125, 0.1, 0.0) & \text{if } x^{(n)} \leq 0.4\,\mathrm{cm} \end{cases}, \tag{4.1}$$

where ρ, p, and v_x are the density, pressure and the velocity in x-direction of the fluid, respectively. Note again that the superscript n and e refer to coordinates on the Yin and Yang grid, respectively. We assume the fluid to obey an ideal gas equation of state with an adiabatic index $\gamma = 1.4$. The surface separating the two constant states is a plane orthogonal to the x-axis located at $x^{(n)} = 0.4\,\mathrm{cm}$, the (positive) x-axis corresponding to a radial ray with angular coordinates $\theta^{(n)} = \pi/2$ and $\phi^{(n)} = 0$. Thus, this 1D planar Sod shock tube problem invokes all three spherical velocity components v_r, v_θ, and v_ϕ when simulating the flow in spherical polar coordinates. This allows us to test both the scalar and vector transformations as well as the interpolation between the Yin and Yang grid patches. The simulation was carried out on an equidistant Yin-Yang grid of $400\,(r) \times 92\,(\theta) \times 272\,(\phi) \times 2$ zones (i.e., with an angular resolution of one degree; see Eq.(3.12)). In radial direction the computational domain ranges from $r = 0.05\,\mathrm{cm}$ to $r = 1.0\,\mathrm{cm}$. We impose a zero-gradient boundary condition at both edges of the radial domain.

The solution of the shock tube problem is well-known. We compare our results with the solution calculated using an exact Riemann solver (Toro 1997). For comparison, data are resampled along the x-direction with a spacing $\Delta x = 0.002\,\mathrm{cm}$. Fig. 4.1 shows one dimensional profiles of ρ, p, v_x, and e (specific internal energy), respectively, along the x-direction at $z^{(n)} = 0.25\,\mathrm{cm}$ and $y^{(n)} = 0\,\mathrm{cm}$ (dashed-dotted line in Fig. 4.2) at different times. Our results agree very well with the solution obtained with the exact Riemann solver. The grid resolution is sufficiently high to give a sharp shock front and contact discontinuity while the rarefaction wave is smooth. The shock position is correct at all time throughout the simulation. The re-sampled

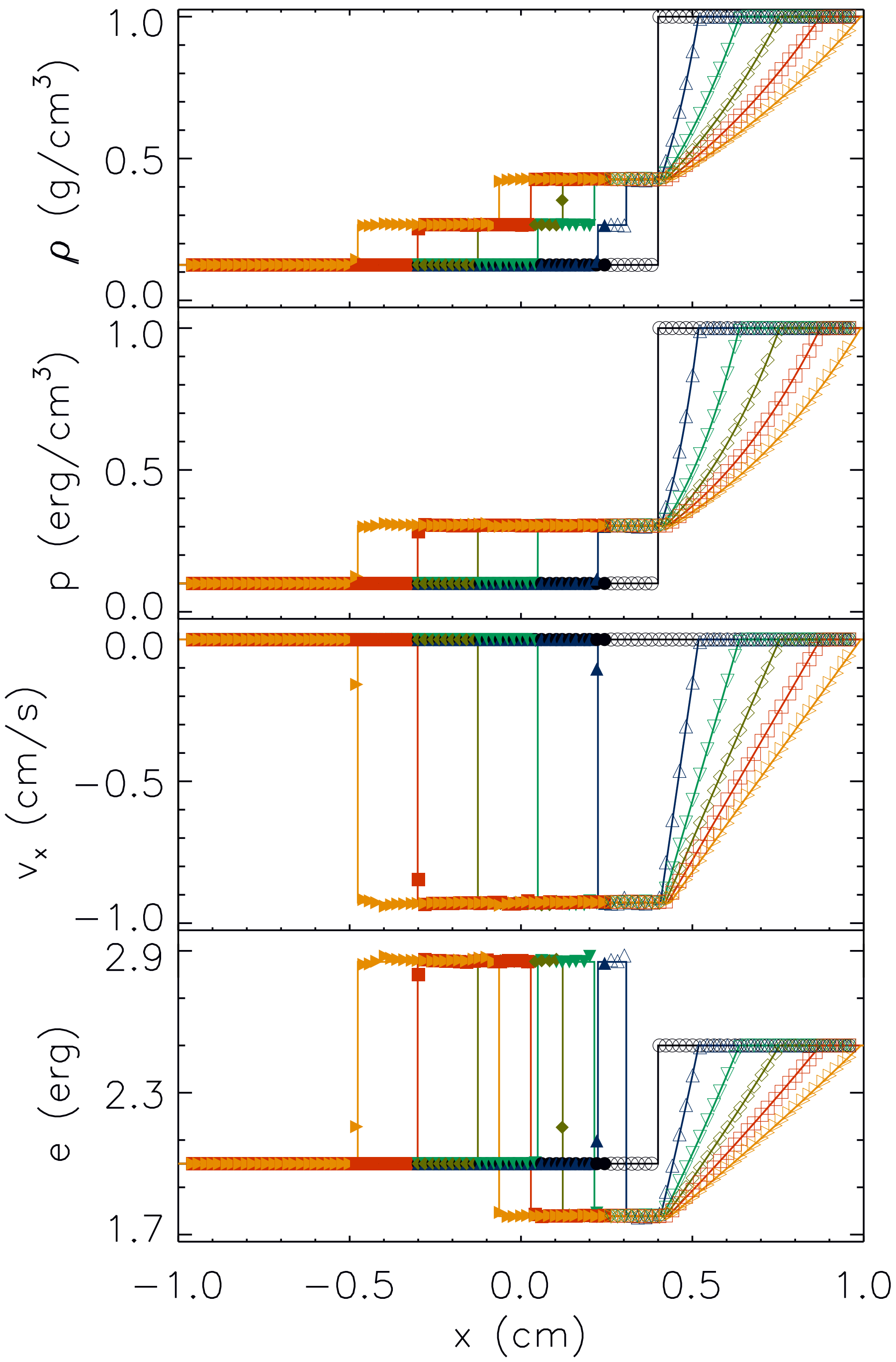

Figure 4.1: One dimensional profiles of density ρ, pressure p, velocity in x-direction v_x, and specific internal energy e are shown along the x-direction at $z^{(n)} = 0.25\,\mathrm{cm}$ and $y^{(n)} = 0\,\mathrm{cm}$ (dashed-dotted line in Fig. 4.2) for the shock tube simulation at every 0.1 s. Open and filled symbols represent data points on the Yin and Yang grid, respectively. Solid lines give the distributions calculated with an exact Riemann solver.

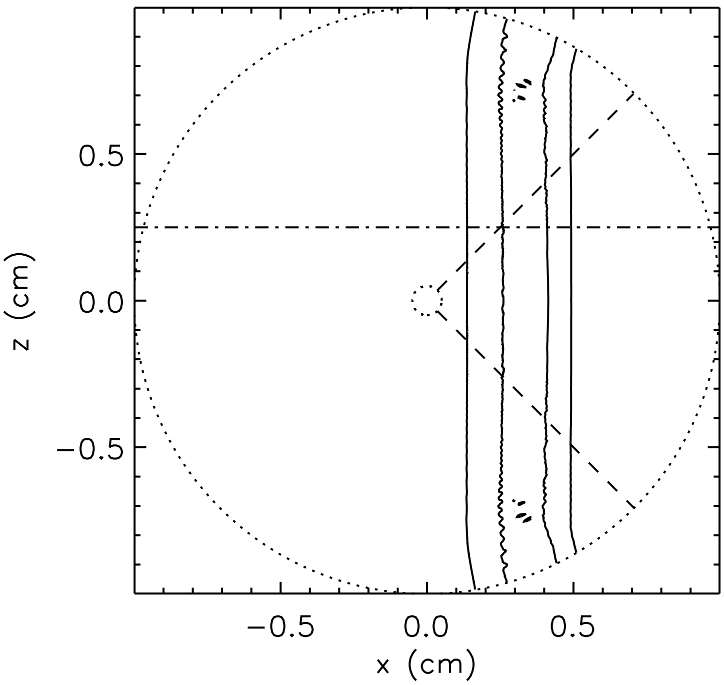

Figure 4.2: Snapshot of density contours in the meridional plane $\phi^{(n)} = 0$ at $t = 0.15\,\mathrm{s}$ for the shock tube test problem. Dashed lines mark the Yin-Yang grid boundary, while the dotted circular curves represent the inner and outer radial boundary of the computational domain, respectively. The one dimensional profiles shown in Fig. 4.1 are re-sampled along the dashed-dotted line at $z^{(n)} = 0.25\,\mathrm{cm}$.

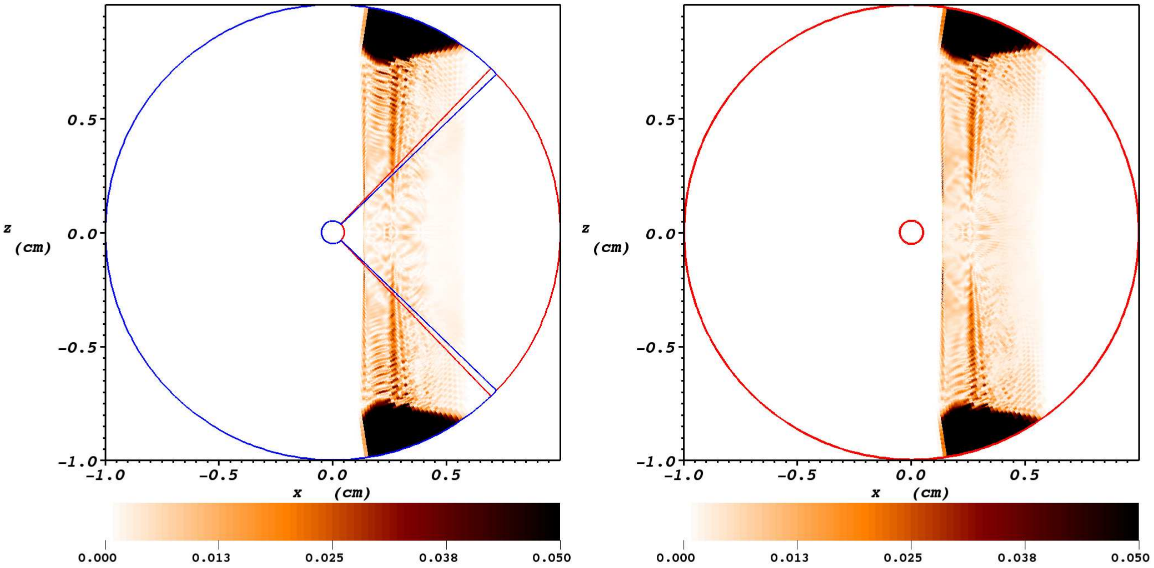

Figure 4.3: Color maps of the tangential velocity defined by $\sqrt{(v_y^{(n)})^2 + (v_z^{(n)})^2}$ in the meridional plane $\phi^{(n)} = 0$ resulting from the (1D Cartesian) shock tube problem. The snapshots are computed using the Yin-Yang grid (left) and a standard spherical polar grid (right) at a time $t = 0.15\,\mathrm{s}$. On the left panel, red and blue lines mark the boundaries of the Yin and the Yang grid patches, respectively. On the right panel, the two red circles show the inner and outer boundary in the radial direction of the standard spherical polar grid. The labels at the color bars give the tangential velocity in units of cm/s. The color range is limited to 0.05 cm/s to emphasize the smallness of the tangential velocity far from the outer radial grid boundary.

data yield an accuracy of approximately 6% on average for shock positions. The shock wave and the contact discontinuity propagate smoothly across the Yin-Yang boundary located at $x^{(n)} = 0.25\,\mathrm{cm}$ without any noticeable effect by the existence of the boundary. To illustrate this behavior, Fig. 4.2 shows lines of constant density in the meridional plane $\phi^{(n)} = 0$ at time $t = 0.15\,\mathrm{s}$. The isocontours are nearly perfectly straight lines perpendicular to the x-axis that are unaffected by the Yin-Yang boundary (dashed line). The contour lines are slightly bent near the outer radial edge of the computational domain due to the zero-gradient boundary condition we have imposed there.

In order to firmly demonstrate that the Yin-Yang boundary does not cause numerical artifacts, we also computed this shock tube problem with a standard spherical polar grid using the same radial and angular resolution as for the Yin-Yang grid described above, *i.e.,* $400\,(r) \times 180(\theta) \times 360\,(\phi)$. We imposed reflecting boundary conditions in θ-direction and periodic ones in ϕ-direction. Fig. 4.3 shows a comparison of the results obtained with both simulations. The two panels give the tangential velocity, defined as $\sqrt{(v_y^{(n)})^2 + (v_z^{(n)})^2}$, in the meridional plane $\phi^{(n)} = 0$ at time $t = 0.15\,\mathrm{s}$ for the Yin-Yang grid (left), and the standard spherical polar grid (right), respectively. This velocity component should remain exactly zero because of the chosen initial conditions. Thus, it is a sensitive indicator whether the Yin-Yang boundary works properly, which obviously is indeed the case as the left panel of Fig. 4.3 shows no hint of the location of that boundary. The modulus of the tangential velocity does nowhere exceed a value of $0.05\,\mathrm{cm/s}$ or approximately 5% of the shock velocity (in x-direction) except near the outer radial edge of the grids, where the boundary condition causes larger numerical errors. Note that nonzero tangential velocities are encountered on both the Yin-Yang grid and the standard spherical polar grid in the same grid regions at the same level. We thus conclude that they are the result of numerical errors that unavoidably occur when propagating a planar shock across a spherical polar grid, be it a standard one or a Yin-Yang grid.

4.2 Taylor-Sedov Explosion

As a second test for our code we consider the Taylor-Sedov explosion problem. We set up the initial state for the problem by mapping a spherically symmetric analytic solution (Landau & Lifshitz 1959) onto the computational grid. We choose the parameters of the problem to mimic a supernova explosion in an interstellar medium. Because the shock wave resulting from the explosion is spherically symmetric with respect to the center of the explosion, we assume the explosion center to be located at the point $(x^{(n)}, y^{(n)}, z^{(n)}) = (7.0, 0.0, 2.5) \times 10^{19}\,\mathrm{cm}$. Hence, this second test problem also involves a non-zero flux of mass, momentum, and energy across the Yin-Yang boundary, and as the previous shock tube test, it probes whether that boundary causes any numerical artifacts.

The initial shock radius is $r_0 = 2.9625 \times 10^{19}\,\mathrm{cm}$ corresponding to a time $t_{exp} = 0.34 \times 10^{11}\,\mathrm{s}$ past the onset of the explosion, and the explosion energy was set to $E_0 = 10^{51}\,\mathrm{erg}$. The ambient medium into which the shock wave is propagating is at rest. It has a constant density $\rho_b = 10^{-25}\,\mathrm{g/cm^3}$, and a constant pressure $p_b = 1.4 \times 10^{-13}\,\mathrm{erg/cm^3}$. The fluid is described by an ideal gas equation of state with an adiabatic index $\gamma = 5/3$, resulting in a density jump across the shock front of $(\gamma + 1)/(\gamma - 1) = 4$. We use a grid resolution of $400 \times 92 \times 272 \times 2$ zones, a computational domain covering the radial interval $r = [0.5, 15.] \times 10^{19}\,\mathrm{cm}$, and employ a zero-gradient boundary condition at both the inner and the outer radial boundary.

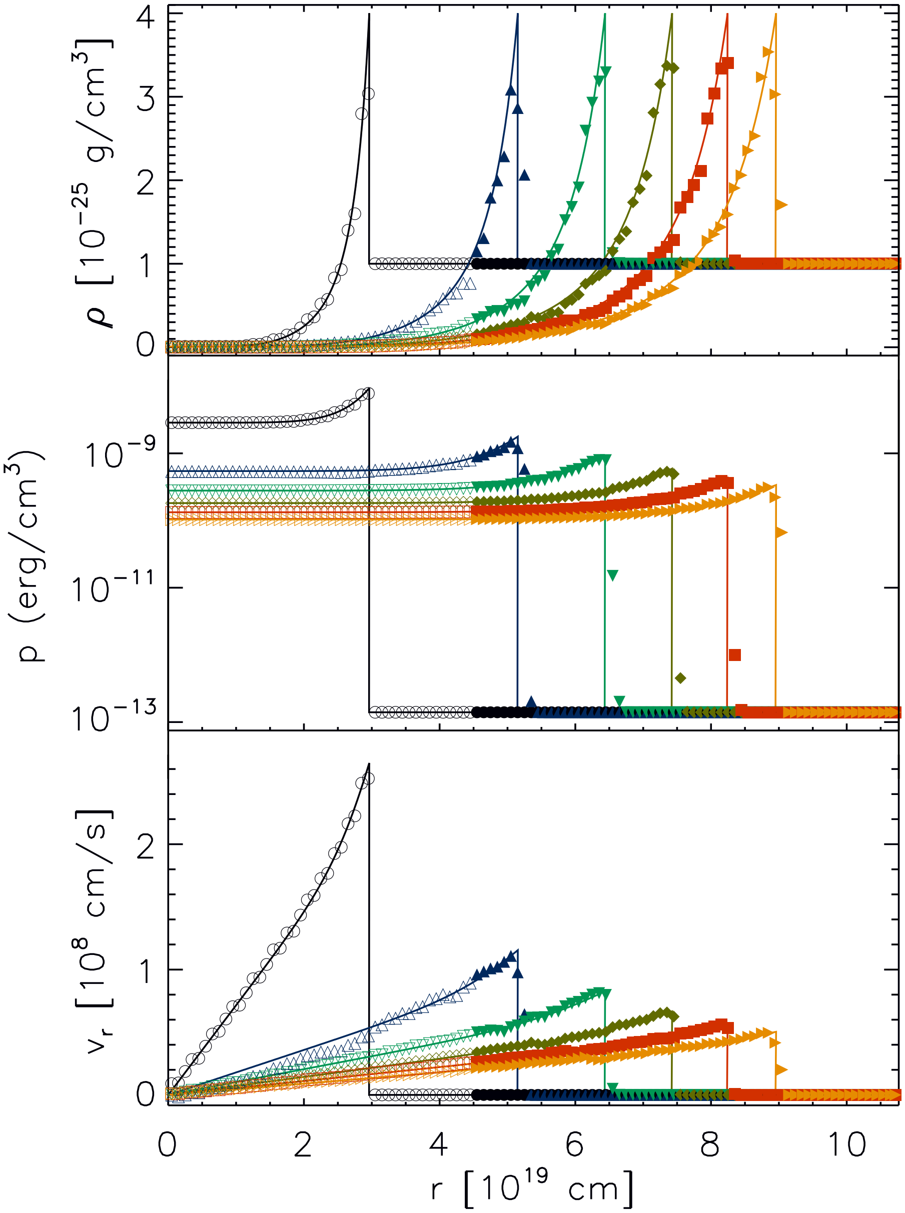

Figure 4.4: Distributions of density (top), pressure (middle) and radial velocity (bottom) versus radius from the explosion center (located at $(x^{(n)}, y^{(n)}, z^{(n)}) = (7.0, 0.0, 2.5) \times 10^{19}$ cm for the Taylor-Sedov explosion problem plotted at every 10^{11} s. Open symbols are data points from the Yin grid, while filled symbols represent sampled data from the Yang grid. The solid lines give the corresponding analytic solution. The data are re-sampled along the dashed-dotted line shown in Fig. 4.5.

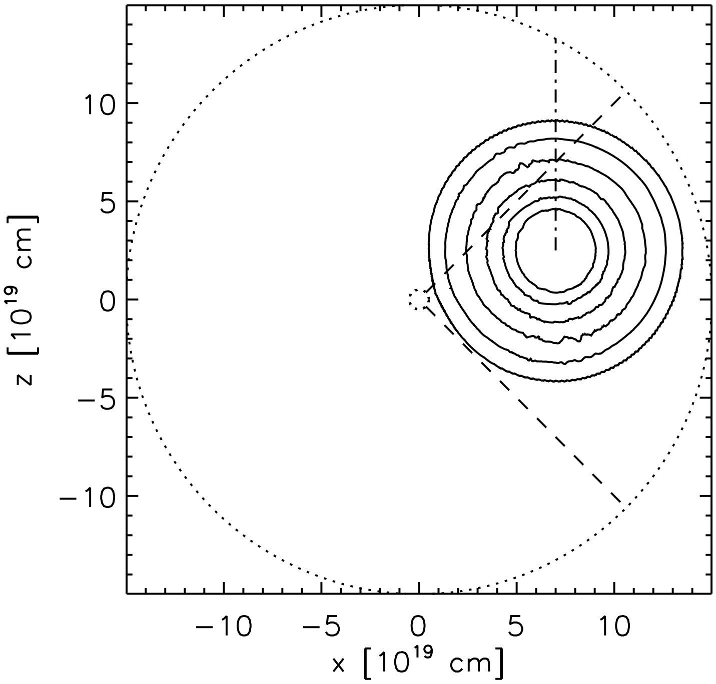

Figure 4.5: Lines of constant density in the meridional plane $\phi^{(n)} = 0$ obtained from our simulation of a Taylor-Sedov explosion. The snapshot is taken at a simulation time $t_{sim} = 2.0 \times 10^{11}$ s which corresponds to an explosion time $t_{exp} \approx 2.34 \times 10^{11}$ s. The dashed lines mark the Yin-Yang boundary, while the two dotted circles represent the inner and outer radial boundary of the computational domain, respectively. The data presented in Fig. 4.4 are re-sampled along the dashed-dotted line .

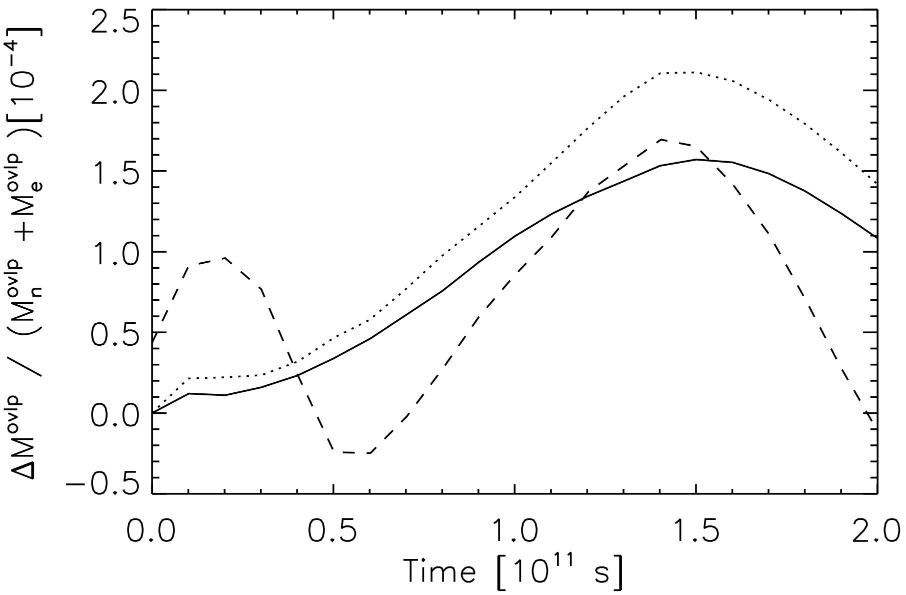

Figure 4.6: Evolution of the mass within the overlap region for the Taylor-Sedov test case computed on the Yin grid, M_n^{ovlp} minus the mass computed on the Yang grid, M_e^{ovlp}, divided by the sum of these two masses. The dashed, dotted and solid lines give the solutions computed on a grid of $400 \times 32 \times 92 \times 2$ zones, (*i.e.,* 3° angular resolution), $400 \times 92 \times 272 \times 2$ zones (*i.e.,* 1° angular resolution), and $400 \times 182 \times 542 \times 2$ zones (*i.e.,* 0.5° angular resolution), respectively.

Our results are shown together with the analytic solution in Fig. 4.4. We have re-sampled our data and calculated radial profiles of the density ρ, pressure p, and radial velocity v_r along a line in z-direction through the explosion center using a uniform radial spacing $\Delta r = 10^{18}$ cm. As one can see the numerical results agree very well with the analytic solution. All flow quantities are smooth across the Yin-Yang boundary, *i.e.,* the shock wave passes that boundary without any noticeable numerical artifact. Due to the finite resolution the density jump across the shock front is slightly smaller in the simulation than the analytic value of four. However, the shock front is sharp throughout the whole simulation, and it propagates with the correct speed. One distinct feature of the Taylor-Sedov solution is its spherical symmetry. To illustrate that the Yin-Yang grid does not destroy this symmetry of the solution, we show a set of lines of constant density in the meridional plane $\phi^{(n)} = 0$ in Fig. 4.5. We also marked the line (dashed-dotted) along which the data given in Fig. 4.4 are re-sampled. The contour lines, all of which are almost perfectly circular, are drawn at a simulation time $t_{sim} = 2.0 \times 10^{11}$ s (*i.e.,* time step number 1276) corresponding to an explosion time $t_{exp} \approx 2.34 \times 10^{11}$ s.

We further studied how the solution differs in the region where the Yin and Yang grid overlap. To this end we compare the total mass within the overlap region computed on the Yin and the Yang grid, respectively. Fig. 4.6 shows the evolution of the relative mass difference, *i.e.,* the mass within the overlap region computed on the Yin grid, M_n^{ovlp} minus the mass computed on the Yang grid, M_e^{ovlp}, divided by the sum of these two masses. We calculated this quantity for three different (angular) grids with $400 \times 32 \times 92 \times 2$ zones (*i.e.,* 3° angular resolution), $400 \times 92 \times 272 \times 2$ zones (*i.e.,* 1° angular resolution), and $400 \times 182 \times 542 \times 2$ (*i.e.,* 0.5° angular resolution), respectively. For all three grid resolutions the relative mass difference has a value of

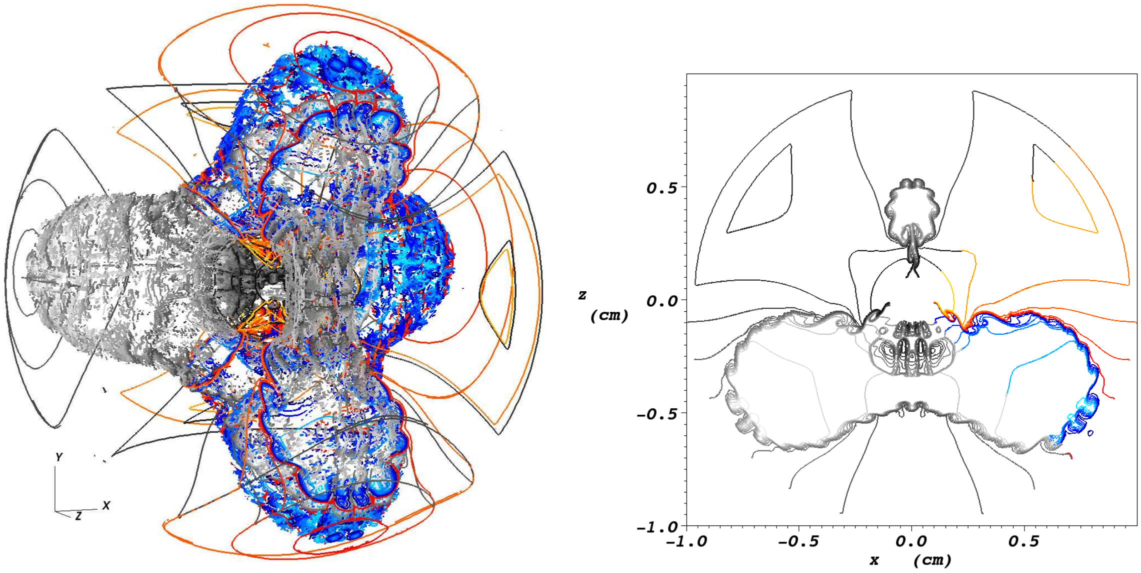

Figure 4.7: Surfaces of constant density in 3D (left) and 2D (right; meridional cut at $\phi^{(n)} = 0$) resulting from the simulation of the Rayleigh-Taylor instability described in the text at $t = 2.85\,\mathrm{s}$. Contour lines on the Yin grid are shown using the blue-yellow colors while contour lines on the Yang grid are displayed using the white-black colors.

about 10^{-4}. Although its evolution with time is different in case of the 3° simulation (because the coarse angular grid causes large errors when mapping the analytic initial data onto the grid which determine the further evolution), Fig. 4.6 shows that for an angular resolution better than 1° the relative mass difference behaves similarly, its maximum value decreasing from 2.1×10^{-4} at 1° angular resolution to 1.5×10^{-4} at 0.5° angular resolution.

4.3 Rayleigh-Taylor Instability

We also simulated a single mode Rayleigh-Taylor instability (RTI) on a Yin-Yang sphere. The initial configuration consists of a spherical shell of a heavier fluid of density $\rho_H = 2\,\mathrm{g/cm^3}$ that is supported against a constant gravitational field $g = 1\,\mathrm{cm/s^2}$ pointing in negative radial direction by a spherical shell of a lighter fluid of density $\rho_L = 1\,\mathrm{g/cm^3}$. The boundary between the two fluid shells is initially located at a radius $r = 0.5\,\mathrm{cm}$. To balance the gravitational force, the initial (radial) pressure distribution is set to

$$P(r) = \begin{cases} P_0 + g\rho_H\,(1.0 - r) & \text{if } r \geq 0.5 \text{ cm} \\ P(r = 0.5) + g\rho_L\,(0.5 - r) & \text{if } r < 0.5 \text{ cm} \end{cases} \tag{4.2}$$

where $P_0 = 1\,\mathrm{erg/cm^3}$. A radial velocity varying in angular direction as the spherical harmonics $Y_l^m(\theta, \phi)$ with $l = 3$ and $m = 2$ is used to perturb the initial configuration. The amplitude of the velocity perturbation is 2.5% of the local sound speed $c_s(r)$. Hence, the initial radial velocity is given by

$$v_r(r, \theta, \phi) = -0.025 \times c_s(r)\, Y_3^2(\theta, \phi). \tag{4.3}$$

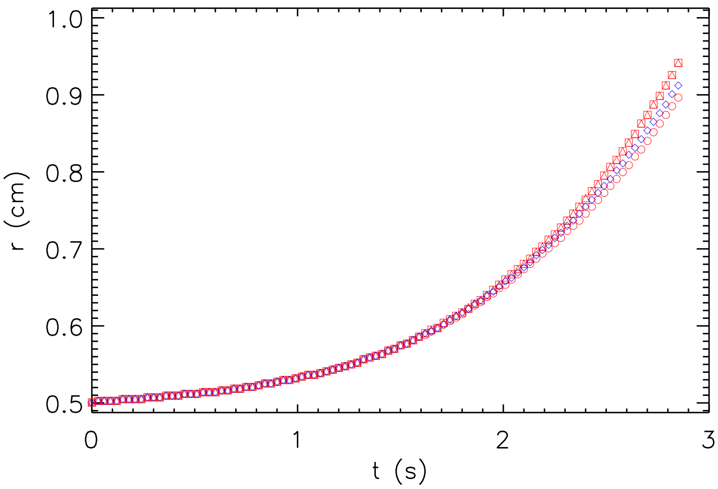

Figure 4.8: Position of the heads of the RTI bubbles versus time. Red symbols (circles, triangles, and squares) show data from the Yin grid, while blue symbols (diamonds) represent data on the Yang grid.

The spherical harmonics $Y_l^m(\theta, \phi)$ are connected with the associated Legendre polynomials P_l^m via the expression

$$Y_l^m(\theta, \phi) = \sqrt{\frac{(l-m)!}{(l+m)!}}\, P_l^m(\cos\theta) e^{im\phi} \,. \tag{4.4}$$

The perturbation mode $(l, m) = (3, 2)$ yields a maximum radial velocity in the directions

$$(\theta, \phi) = \{(\pi - \alpha, 0),\, (\pi - \alpha, \pi),\, (\alpha, \pi/2),\, (\alpha, -\pi/2)\} \;, \tag{4.5}$$

where $\alpha \equiv \arccos(\sqrt{3}/3)$. The remaining two velocity components of the perturbation mode are set equal to 0. The fluids are described by an ideal gas equation of state with an adiabatic index $\gamma = 1.4$. The simulation is carried out on a Yin-Yang grid of $400 \times 92 \times 272 \times 2$ zones. To keep the fluid in hydrostatic equilibrium, a zero-gradient boundary condition is used for both the inner and outer boundary in radial direction. The inner radial boundary is located at $r = 0.1$ cm.

A snapshot of the resulting density distribution obtained with the Yin-Yang grid is displayed in Fig. 4.7 at epoch $t = 2.85$ s. The left panel shows color coded contour lines in 3D, and the right one a meridional cut at $\phi^{(n)} = 0$. The contour lines are drawn using different color tables for the Yin and Yang grid, respectively. Four distinct bubbles of rising low density fluid (Yin: blue; Yang: bright gray) are clearly visible that reflect the initial perturbation mode $(l, m) = (3, 2)$. High density fluid (Yin: yellow/red; Yang: dark gray/black) sinks down and settles at the inner part of the sphere. One can also notice Kelvin-Helmholtz instabilities developing at the surface of the bubbles. This is particularly obvious in the meridional cut (right panel). One of the RTI bubbles is within the Yang grid, while the three others reside on the Yin grid. It is obvious that the bubbles are distributed symmetrically following the perturbation pattern regardless of the grid patch. The 2D contour lines shown in the right panel of Fig. 4.7 emphasize this fact.

The RTI bubbles grow with nearly the same growth rate in all four (perturbation) directions, as can also be seen from Fig. 4.8 that displays the position of each bubble's head versus time. The four curves lie exactly on top of each other during the phase of linear growth. There are slight discrepancies between the four curves in the non-linear regime, because the linear grid

Component	Prolate spheroid		Sphere	
	Poisson solver	extended Poisson solver	Poisson solver	extended Poisson solver
$\hat{\boldsymbol{r}}$	4.821×10^{-4}	4.698×10^{-4}	1.598×10^{-2}	1.557×10^{-2}
$\hat{\boldsymbol{\theta}}$	6.134×10^{-2}	2.592×10^{-2}	1.67×10^{-2}	1.67×10^{-2}
$\hat{\boldsymbol{\phi}}$	1.245×10^{-2}	2.435×10^{-3}	1.655×10^{-2}	1.655×10^{-2}

Table 4.1: Mean errors in the gravitational acceleration.

resolution in angular direction is slightly non-equidistant (due to its θ dependence). Two curves from the Yin grid coincide perfectly since they represent the two bubbles that lie symmetrically above and below the equator in the Yin grid. The results confirm that the Yin-Yang grid does not favor any angular direction on the sphere. Since our aim was only to demonstrate this important fact, we do not further analyze the growth rate of the RTI.

4.4 Gravitational Potential of Homogeneous Spheroids

We investigate the accuracy of our gravity solver by calculating the gravitational potential of homogeneous spheroids. We consider two homogeneous self-gravitating configurations: a prolate spheroid with an axis ratio of 0.7, and a sphere. The configurations have a constant density $\rho = 1\,\mathrm{g/cm^3}$, and are embedded into a homogeneous background of much lower density $\rho_b = 10^{-20}\,\mathrm{g/cm^3}$ in order to minimize the background's contribution to the gravitational potential. The semi-major axis of the spheroid aligns with the x-axis, while its center is placed at the origin of the Yin-Yang grid. To provide a more difficult test for our multipole based gravity solver, we shift the center of the sphere off the origin of the computational grid by more than one sphere radius.

The analytical form of the gravitational potential for both type of configurations are known. The solution for the prolate spheroid can be found in chapter 3 of Chandrasekhar (1969), and the sphere's potential can be easily calculated. Fig. 4.9 shows contour lines of the gravitational potential for both cases in the meridional plane $\phi^{(n)} = 0$. The potential is calculated on a grid of $400 \times 92 \times 272 \times 2$ zones with $L = 15$, where L is the number of spherical harmonics taken into account (see section 3.3). The contour lines are smooth across the Yin-Yang boundary for both the prolate spheroid and the sphere.

Concerning the convergence behavior of the solver, we consider various grid resolutions and a number of spherical harmonics ranging up to $L = 25$ for this convergence test. The grid resolutions used in the test are $400 \times 92 \times 272 \times 2$ zones, $400 \times 47 \times 137 \times 2$ zones, $200 \times 92 \times 272 \times 2$ zones, and $200 \times 47 \times 137 \times 2$ zones, respectively. The maximum and mean error of the gravitational potential are given as a function of L for both considered configurations in the middle and right panels of Fig. 4.9, respectively. Both errors show a convergence behavior with higher grid resolution, and tend to saturate at large values of L. This behavior is similar to what is described in Müller & Steinmetz (1995). In addition, for lower grid resolution the accuracy saturates at a lower number of spherical harmonics compared to calculations with a higher grid resolution. This is expected since higher order terms in the multipole expansion are not well represented on grids of lower angular resolution.

We also tested our extended Poisson solver discussed in section 3.3. In Table 4.1 we compare the mean errors in the components of the gravitational acceleration for both the prolate spheroid

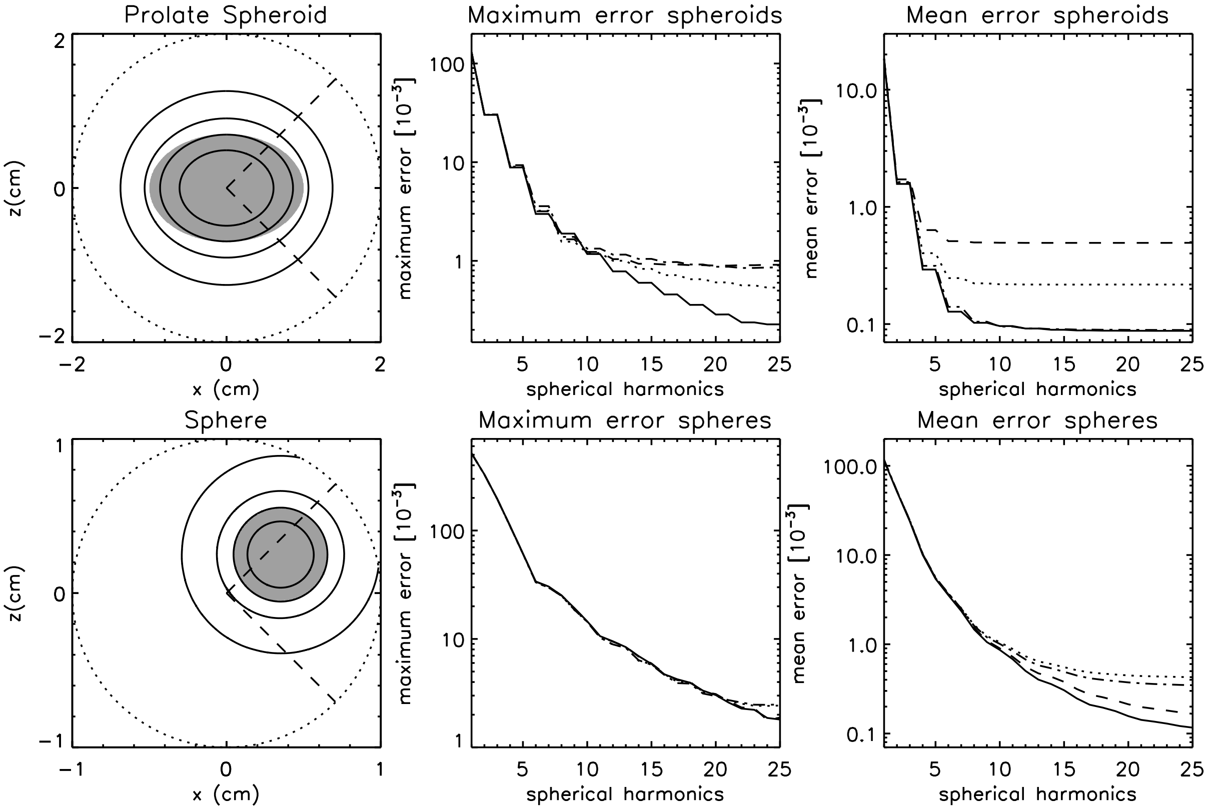

Figure 4.9: Contour lines of the gravitational potential (left column) for two homogeneous self-gravitating configurations: a prolate spheroid (top row) with an axis ratio of 0.7, and a sphere (bottom row). The configurations are indicated by the dark-gray shaded areas. Dashed lines show the Yin-Yang boundary, while dotted lines indicate the outer radial boundary of the computational grid. The middle and right columns give the maximum and mean error of the numerically calculated gravitational potential for different grid resolutions as a function of the number of spherical harmonics used in our multipole gravity solver. The solid, dotted, dashed, and dashed-dotted lines in both columns correspond to a grid resolution of $400 \times 92 \times 272 \times 2$ zones , $400 \times 47 \times 137 \times 2$ zones, $200 \times 92 \times 272 \times 2$ zones, and $200 \times 47 \times 137 \times 2$ zones, respectively.

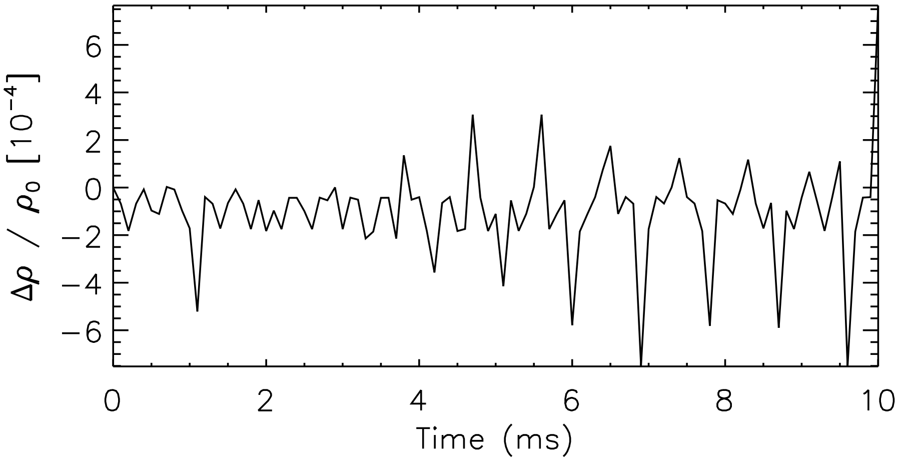

Figure 4.10: Relative change of the central density of a non-rotating (nearly) equilibrium polytrope as a function of time.

and the sphere test case computed with the numerically differentiated gravitational potential given in Eq. (3.25) with those obtained from the analytic expression given in Eqs. (3.32), (3.37), and (3.38), respectively. We used a grid of $400 \times 92 \times 272 \times 2$ zones and $L = 15$ for this comparison.

For the prolate spheroid test case the "analytically" obtained accelerations exhibit a smaller mean error, especially for the θ- and ϕ-component of the gravitational acceleration. This results from a strong decrease of the maximum error, which is large in regions where the angular components of the gravitational acceleration approach zero, *i.e.,* near the major and minor axes of the prolate spheroid. However, in these regions the accelerations in θ and ϕ-direction are orders of magnitude smaller than the radial component. Thus, they contribute only a tiny fraction to the total acceleration. In the sphere test case both variants of the extended Poisson solver produce similar mean errors. Based on these results we conclude that the extended Poisson solver, which provides the gravitational acceleration using analytic expressions, works properly. Moreover, it gives a slightly more accurate gravitational acceleration, as it does not involve numerically differencing the gravitational potential. Nevertheless, for the reasons stated in section 3.3, we prefer to use the Poisson solver of Müller & Steinmetz (1995) in our simulations.

4.5 Self-gravitating Polytropes

Using our Yin-Yang grid based hydro-code we have also considered self-gravitating, non-rotating and rotating equilibrium polytropes. Both kinds of polytropes provide another test of the Poisson solver, and a test of how well our hydrodynamics code can keep a self-gravitating configuration in hydrostatic and stationary equilibrium, respectively. In addition, the rotating polytrope also serves to test the proper working of the Yin-Yang boundary treatment, as it involves a considerable and systematic flow of mass, momentum and energy flux across that boundary due to the polytrope's rotation.

The polytropes have a polytropic index $n = 1$, a polytropic constant $\kappa = 1.455 \times 10^5$, and a central density of $\rho_c = 7.905 \times 10^{14}\,\mathrm{g/cm^3}$. For our test runs we interpolated equilibrium polytropes calculated with the method of Eriguchi & Müller (1985) onto a Yin-Yang sphere,

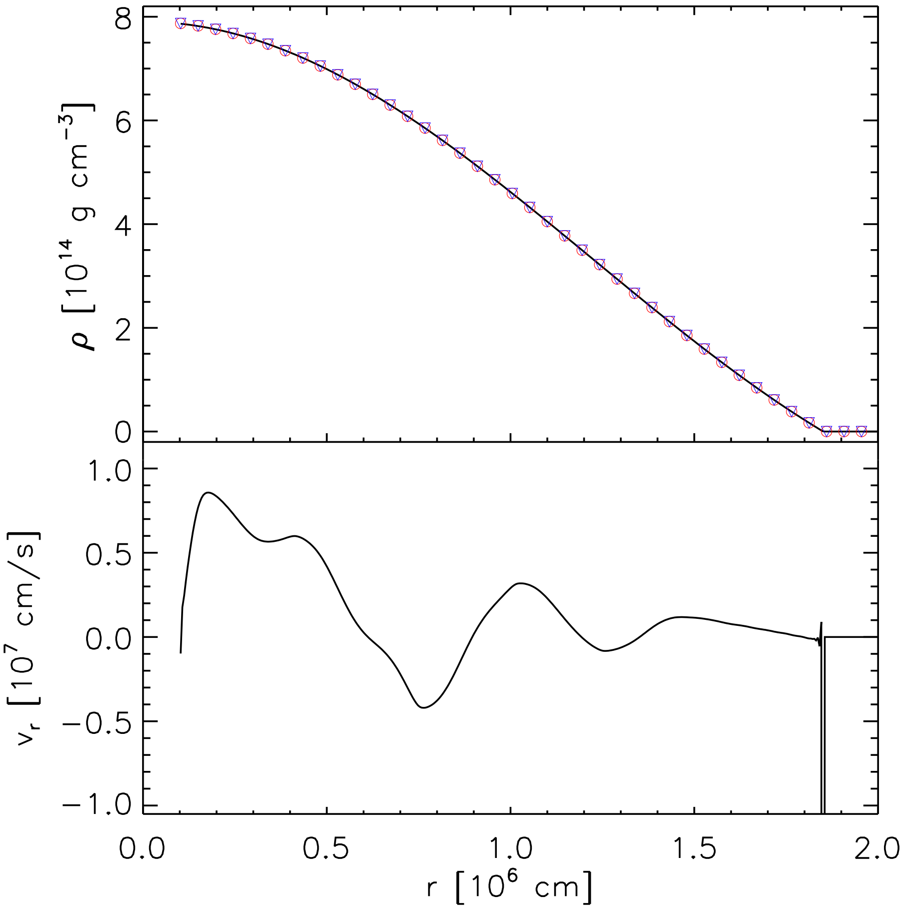

Figure 4.11: Density (top) and radial velocity (bottom) of a non-rotating $n = 1$ equilibrium polytrope as a function of radius after $t = 10$ ms of "evolution". In the top panel, the solid line shows the initial density profile. Red circles and blue triangles correspond to data from the Yin and the Yang grid, respectively.

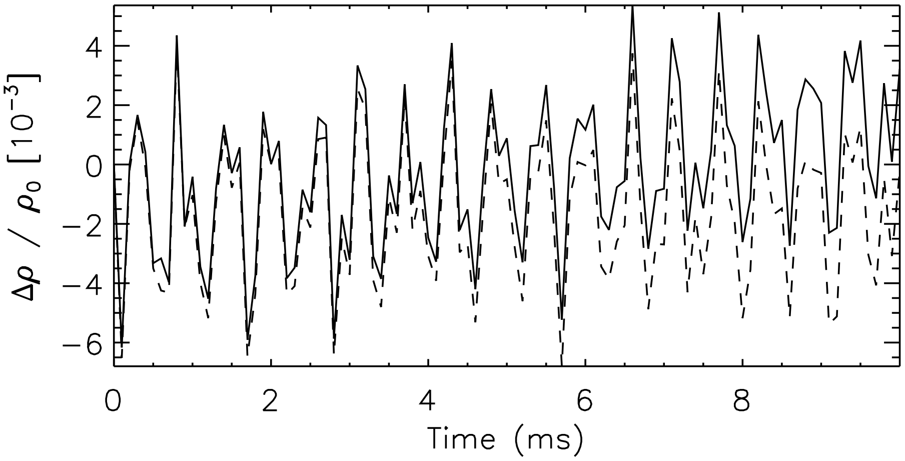

Figure 4.12: Same as Fig. 4.10 but for a rotating polytrope. The solid and dashed curves show the relative variation of the density along an equatorial ray ($\theta^{(n)} = \pi/2$; $\phi^{(n)} = 0$) and along the pole ($\theta^{(n)} = 0$), respectively.

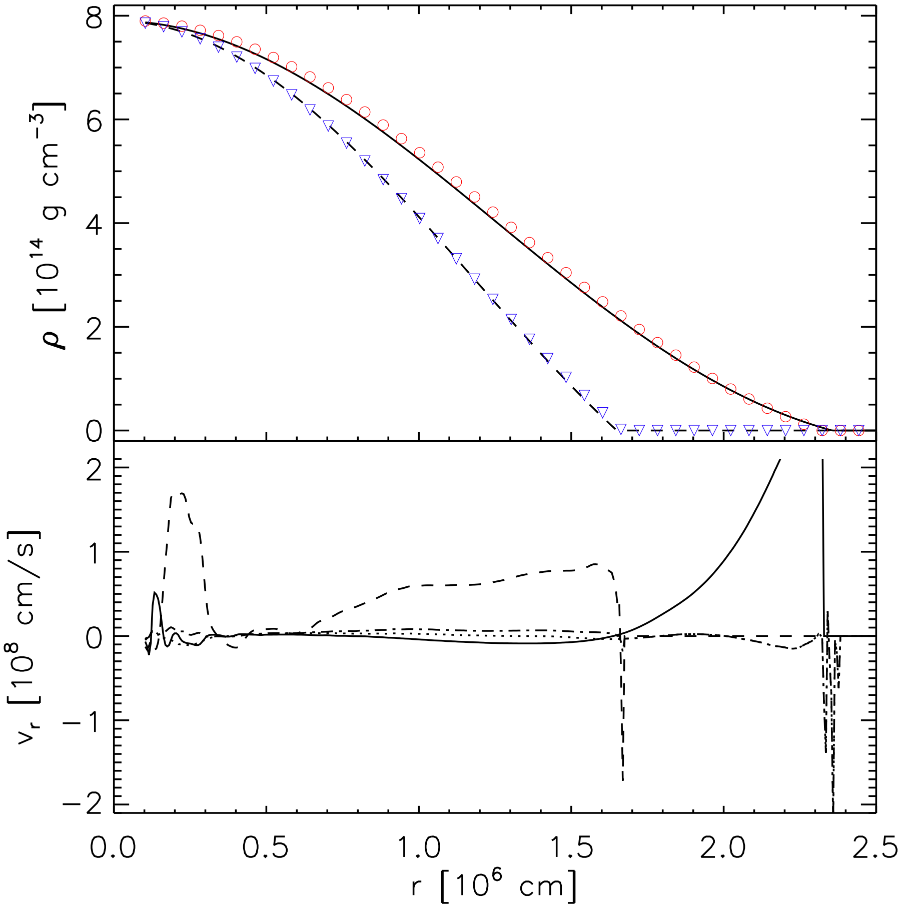

Figure 4.13: Density (upper panel) and radial velocity (lower panel) of a $n = 1$ rotating polytrope in stationary equilibrium as a function of radius after $t = 10\,\mathrm{ms}$ of "evolution". In both panels the solid and dashed lines show the profiles along an equatorial ray ($\theta^{(n)} = \pi/2$, $\phi^{(n)} = 0$) and along the pole ($\theta^{(n)} = 0$), respectively. Red circles and blue triangles in the upper panel correspond to data from the Yin and the Yang grid, respectively. In the lower panel, we show in addition time averaged (over the interval $t = [9, 10]\,\mathrm{ms}$) velocity profiles along the equatorial ray (dotted) and the pole (dashed-dotted).

and simulated their dynamic evolution (occurring as the interpolated configuration is not in perfect hydrostatic equilibrium). The central region ($r < 1\,\mathrm{km}$) of the polytrope is cut out and replaced by a corresponding point mass to allow for a larger time step.

We use an artificial atmosphere technique to handle those regions of the computational grid that lie outside the (rotating, i.e., non-spherical) polytrope. The density in the atmosphere is set equal to a value $\rho_{atm} = 10^{-10}\rho_c$, where ρ_c is the central density of the polytrope. Here, atmosphere denotes any grid zone whose density is less than the cut-off density $\rho_{cut-off} = 10^{-7}\rho_{max}$. Furthermore, for all zones in the atmosphere the velocity is set to zero in order to keep the atmosphere quiet. This procedure is applied at the end of every time step throughout the simulation. A zero-gradient boundary condition is imposed at the outer radial boundary, and a reflecting boundary condition at the inner one. The polytrope's evolution is followed for 10 ms corresponding to approximately 10 dynamic time scales in order to check how well the initial approximate equilibrium configuration is maintained by the Yin-Yang code.

For the non-rotating polytrope, we employ a grid of $400 \times 20 \times 56 \times 2$ zones. Note that we are able to use a relatively low angular resolution compared to the other tests, because the problem has spherical symmetry. Our results show that the polytrope stays perfectly spherically symmetric throughout the simulation, and that the non-radial velocities inside the polytrope remain zero. This demonstrates that the Yin-Yang grid is able to preserve the initial spherical symmetry. Fig. 4.10 shows the evolution of the central density (more precisely of the density of the innermost radial zone at $r = 1\,\mathrm{km}$), which exhibits oscillations with an amplitude of the order of 10^{-4} without any sign of a systematic trend. Comparing the initial radial distributions of the density (Fig. 4.11, upper panel) and the radial velocity (Fig. 4.11, lower panel) of the polytrope with those after 10 ms of evolution, we find no significant deviations. Relative changes in the density profile are of the order of 10^{-4}, comparable to the size of the fluctuations of the central density. Only for zones near the edge of the polytrope the deviations can reach a level of up to 20%, in particular in the zone next to the atmosphere. The figure also shows that data points from the Yin and the Yang grid lie on top of each other confirming that the code preserves the initial spherical symmetry of the polytrope very well. Except for the zones at the polytrope's surface, where the radial velocity is fluctuating at a level of approximately $2 \times 10^8\,\mathrm{cm/s}$, the radial velocities are less than $10^6\,\mathrm{cm/s}$ (i.e., less than 0.1% of the local sound speed). Thus, we conclude that a non-rotating ($n = 1$) equilibrium polytrope is correctly handled by our Yin-Yang hydro-code.

The rotating polytrope needs a higher grid resolution in θ-direction, as it is no longer spherically symmetric. Thus, we used a grid resolution of $400 \times 92 \times 272 \times 2$ zones for this simulation. The initial oblate equilibrium configuration has an axis ratio of 0.7. We, again, evolve the configuration for 10 ms to test the correct treatment of the situation by our Yin-Yang hydro-code.

Fig. 4.12 shows the relative variation of the central density as a function of time along an equatorial ray ($\theta^{(n)} = \pi/2$; $\phi^{(n)} = 0$) and along the pole ($\theta^{(n)} = 0$), respectively. One also recognizes a slight systematic trend in the behavior of the density fluctuation, which is steeper along the equator than at the pole. However, in both cases the relative increase of the central density is very small ($\sim 10^{-3}$). The initial radial density profiles along the pole and the equator do not show any significant change during the 10 ms of evolution we have simulated with the Yin-Yang code (Fig. 4.13, upper panel). The axis ratio has slightly increased to a value of 0.719. The radial velocities (Fig. 4.13, lower panel) are larger than in the non-rotating case by about an order of magnitude, because it is obviously more difficult to keep a rotating polytrope in equilibrium than a non-rotating (spherically symmetric) one. We again find the

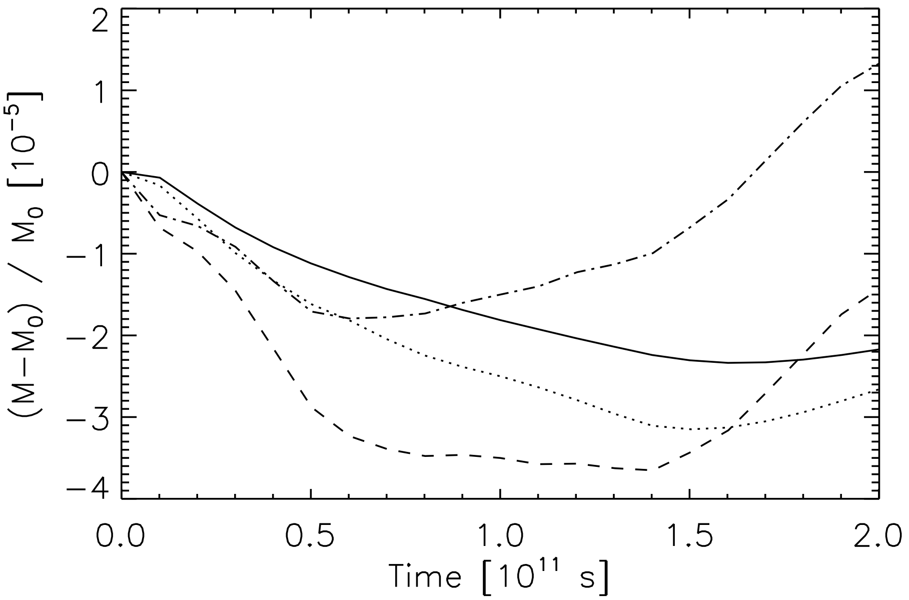

Figure 4.14: Evolution of the relative mass loss, $(M - M_0)/M_0$, where M_0 is the initial total mass, for the Taylor-Sedov test simulated on four different (angular) grids with $400 \times 32 \times 92 \times 2$ zones (*i.e.,* 3° angular resolution; dashed line), $400 \times 47 \times 137 \times 2$ zones (*i.e.,* 2° angular resolution; dashed-dotted line), $400 \times 92 \times 272 \times 2$ zones (*i.e.,* 1° angular resolution; dotted line), and $400 \times 182 \times 542 \times 2$ zones (*i.e.,* 0.5° angular resolution; solid line), respectively.

largest radial velocities (a few times 10^8 cm/s) near the surface of the polytrope, especially along the equator. However, these velocities vary with time. When averaged over time (in the time interval $t = [9, 10]$ ms) the profiles become flatter and the velocities smaller. This confirms that the polytrope is oscillating around its equilibrium configuration.

4.6 Conservation problem

The Yin-Yang grid has a disadvantage common with other types of overlapping grids (see, e.g., Chesshire & Henshaw 1994; Wang 1995; Wu et al. 2007). The communication via interpolation between the two grid patches does not guarantee conservation of conserved quantities even though the finite-volume difference scheme employed on each grid patch is conservative. Non-conservation occurs when a flow across the Yin-Yang boundary is present. This is the case in most of our tests except for the simulation of the non-rotating polytrope that involves only radial flow.

Nevertheless, we are still able to obtain sufficiently good results for all the test simulations discussed in the previous section. The degree of non-conservation is highly problem dependent. A simulation involving a considerable and systematic flow across the Yin-Yang boundary, as *e.g.,* in the case of the rotating polytrope, will result in a larger degree of non-conservation. We observe that the total mass increases by 0.07% within 10 ms (or about ten dynamical timescales) in the case of the rotating polytrope. For the Taylor-Sedov test case, which is the cleanest test case in this respect (as it involves, *e.g.,* no boundary effects like the shock tube, and *e.g.,* no artificial atmosphere like the rotating polytrope), we find a mass loss of the order of 10^{-5}, only.

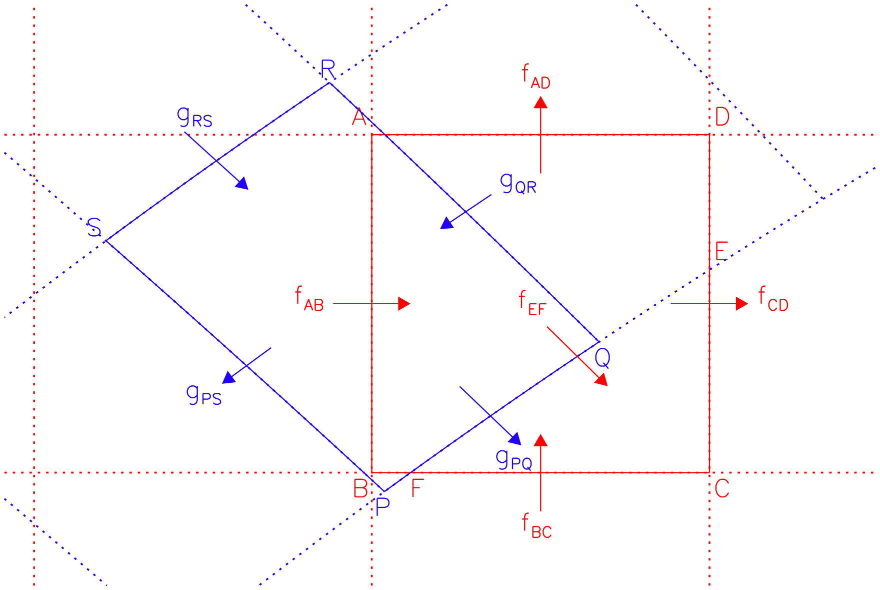

Figure 4.15: Illustration of the Yin-Yang grid overlap configuration, where $PQRS$ is a grid zone at the boundary of the Yang grid (blue) which overlaps with the underlying grid zone $ABCD$ of the Yin grid (red). Fluxes referring to the Yin and the Yang grid are denoted by f and g, respectively.

As Fig. 4.14 demonstrates this mass loss can be reduced by using a higher angular resolution.

Conservation of conserved scalar quantities can be obtained to machine precision by applying the algorithm described in detail in Peng et al. (2006), and summarized below. According to this algorithm scalar fluxes at the outer edges of boundary zones of both the Yin and the Yang grid are replaced by scalar fluxes computed using only "interior" fluxes from adjacent grid zones.

As an illustration, consider the Yin-Yang grid overlap configuration in Fig. 4.15, where $PQRS$ is a grid zone at the boundary of the Yang grid (blue) which overlaps with the underlying grid zone $ABCD$ of the Yin grid (red). Fluxes referring to the Yin and the Yang grid are denoted by f and g, respectively.

The boundary flux g_{PQ} of the Yang grid is replaced by the flux

$$f_{PQ} = f_{FQ} + f_{PF}, \tag{4.6}$$

where f_{FQ} and f_{PF} are the fluxes through the segments $\overline{FQ}$ and $\overline{PF}$, respectively.

The flux f_{FQ} in Eq.(4.6) is calculated using information from zone $ABCD$. The evolution of a scalar quantity ξ_{ABCD} of zone $ABCD$ is given by

$$\xi^{t+\Delta t}_{ABCD} = \xi^{t}_{ABCD} + (f_{AB} - f_{CD} + f_{BC} - f_{AD}). \tag{4.7}$$

Similarly, for the fraction of the zone $ABCD$ defined by the polygon $ABFED$ one has,

$$\xi^{t+\Delta t}_{ABFED} = \xi^{t}_{ABFED} + (f_{AB} - f_{CD}\frac{\overline{DE}}{\overline{CD}} + f_{BC}\frac{\overline{BF}}{\overline{BC}} - f_{AD} - f_{EF}). \tag{4.8}$$

Assuming a piecewise constant state within the zone $ABCD$, Eqs.(4.7) and (4.8) lead to

$$\alpha(\xi^{t+\Delta t}_{ABCD} - \xi^{t}_{ABCD}) = \xi^{t+\Delta t}_{ABFED} - \xi^{t}_{ABFED} \tag{4.9}$$

Computational domain	Angular grid resolution	Gain factor
full 4π sphere	3°	26
	2°	40
	1°	80
sphere except for a cone of 5° half opening angle cut-out at both poles	1°	7

Table 4.2: Expected gain factor when using the Yin-Yang grid.

where α is the overlapping volume fraction (area) described in section 3. Therefore,

$$\alpha(f_{AB} - f_{CD} + f_{BC} - f_{AD}) = f_{AB} - f_{CD}\frac{\overline{DE}}{\overline{CD}} + f_{BC}\frac{\overline{BF}}{\overline{BC}} - f_{AD} - f_{EF} \tag{4.10}$$

Note that the flux f_{EF} is the only unknown in Eq.(4.10). Since the intersection points E and F are already known from the step to calculate the volume fraction α, the lengths of all segments can be obtained. The flux f_{FQ} is then given by

$$f_{FQ} = f_{EF}\frac{\overline{FQ}}{\overline{EF}}\,. \tag{4.11}$$

After obtaining the still missing flux f_{PF} in Eq.(4.6) by a similar procedure, the scalar quantity ξ_{PQRS} of the boundary zone $PQRS$ is updated according to

$$\xi^{t+\Delta t}_{PQRS} = \xi^{t}_{PQRS} + (g_{QR} - g_{PS} + g_{RS} - f_{PQ}). \tag{4.12}$$

This procedure is then repeated to update all boundary grid zones.

After implementing the above algorithm we are able to conserve mass and total energy up to machine precision. However, the conservation of momentum is more complicated since the momentum equations in spherical coordinates involve not only flux (*i.e.,* divergence) terms but also source terms (due to the presence of fictitious and pressure forces), and due to the "mixing" of momentum components as the Yin and Yang grid patches are rotated relative to each other (see Fig. 4.15).

As we have not yet devised and implemented a corresponding momentum conservation algorithm, momentum is not yet perfectly conserved in our code. For that reason we also refrain from using the scalar conservation algorithm described above, since in some simulations (*e.g.,* in the Taylor-Sedov explosion simulation) we encountered a negative internal energy in some zones due to the inconsistency arising from the perfect conservation of mass and total energy on one hand and the imperfect conservation of momentum on the other hand. In our test runs the momentum violation is small, *e.g.,* amounting to 0.24% (0.03%) angular momentum loss in the case of the rotating polytrope for a grid with three (one) degree angular resolution.

4.7 Performance and Efficiency

One of the main purposes in implementing the Yin-Yang grid is to ease the severe restriction imposed on the size of the time step for any explicit hydrodynamics scheme by the CFL condition in the polar regions of 3D simulations using a grid in spherical polar coordinates. In most applications the size of the time step is restricted most strongly by the size of the zones in ϕ-direction, which is smaller than the size in θ-direction by the factor $\sin\theta$ assuming an equal angular resolution $\delta \equiv \Delta\theta = \Delta\phi$ in both angular directions.

For a spherical polar grid the factor $\sin\theta$ implies (assuming zone centered variables) a minimum zone size

$$d_\phi^{sph} \equiv \delta \, \sin(\delta/2)$$

(in radians) in ϕ-direction for the first zone next to the pole. Typically, $\sin(\delta/2) \approx 10^{-2}$. On the other hand, applying the Yin-Yang grid yields

$$d_\phi^{YY} \equiv \delta \, \sin(\pi/4 - \delta/2)$$

for the size of the smallest zone in ϕ-direction, which is typically about 0.7. Hence, for the Yin-Yang grid the smallest zone size in azimuthal direction is larger by the ratio

$$\frac{d_\phi^{YY}}{d_\phi^{sph}} = \frac{\sin(\pi/4 - \delta/2)}{\sin(\delta/2)} \tag{4.13}$$

compared to the spherical polar grid.

Table 4.2 gives the value of this ratio for grids of various angular resolution, and various computational domains. These numbers provide an estimate of the gain in computation time one can expect when using the Yin-Yang grid instead of the spherical polar grid.

However, the gain factor calculated from the relative grid spacings does not determine the gain in the size of the time step, as the latter is given in a more complicated way by the CFL condition

$$\Delta t_{CFL} < C \left(\left|\frac{v_r}{\Delta r}\right| + \left|\frac{v_\theta}{r\Delta\theta}\right| + \left|\frac{v_\phi}{r\sin\theta\Delta\phi}\right| + \sqrt{\frac{c_s^2}{\Delta r^2 + (r\Delta\theta)^2 + (r\sin\theta\Delta\phi)^2}} \right)^{-1}, \tag{4.14}$$

where C, v_r, v_θ, v_ϕ, and c_s are the Courant factor, the flow velocities in radial, colatitude and azimuthal direction, and the local sound speed, respectively. The CFL condition shows that the increase in the size of the CFL time step is somewhat smaller than implied by the gain factor resulting from the ratio of the sizes of the smallest zones of the Yin-Yang grid and the spherical polar grid. In addition, the increase of the time step is problem dependent.

Besides the performance gain due to the increased size of the CFL time step, the Yin-Yang grid also requires less computational zones to cover the full sphere, and thus less computational time. For an angular resolution δ the spherical polar grid needs

$$(\pi/\delta) \times (2\pi/\delta)$$

zones to cover the full sphere, while the Yin-Yang grid requires only

$$(\pi/2\delta + 2) \times (3\pi/2\delta + 2) \times 2$$

zones. Hence, up to 25% fewer computational zones are required. The gain depends only weakly on angular resolution and is problem independent.

However, employing the Yin-Yang grid also requires some extra amount of computation compared to the spherical polar grid (see Sec. 3.2.2). In the following we only consider the extra costs of calculations during the actual simulation, but not the extra costs arising during the initialization, since these are negligible. We emphasize again that there are two major extra sets of calculations necessary when applying the Yin-Yang grid. The first set concerns the interpolation of the ghost zone values that are needed for the communication between the Yin and Yang grid patches. The second set arises from the interpolation of the density onto the auxiliary spherical polar grid grid and the interpolation of the gravitational potential back from the auxiliary grid onto the Yin-Yang grid. Exploiting the algorithms described in Sec. 3, the computational cost for both parts is almost negligible compared to the total computing time. Interpolation of the ghost zone values requires only 2.3% of the total computing time per cycle in simulations with self-gravity, while the interpolation of density and gravitational potential performed within the gravity solver accounts for 1.5% of the computing time needed for the gravity solver. This corresponds to approximately 0.3% of the computing time per cycle.

To obtain actual numbers for the gain, we performed several timing tests including simulations with and without self-gravity using four different grid resolutions. The tests were carried on an IBM Power6 using a single processor. According to these tests the computing time per cycle for the Yin-Yang grid averaged over five cycles is approximately 15% and 20% smaller than for the spherical polar grid for simulations without self-gravity and with 2° and 1° angular resolution, respectively. For simulations including self-gravity, the gain factor decreases by 3% approximately.

Concerning the gain from the less restrictive CFL condition, we consider the case of the rotating polytrope since the size of the time step does not vary much throughout the simulation. For an angular resolution of 1°, we find a gain of approximately a factor of 63 when using the same Courant number both for the Yin-Yang grid and the spherical polar grid.

Chapter 5

Hydrodynamical Neutron Star Kicks in 3D

Young neutron stars (NSs) possess mean space velocities around $400\,\mathrm{km\,s^{-1}}$, much larger than those of their progenitor stars, implying that they are accelerated during their birth in a supernova (SN) explosion (e.g., Faucher-Giguère & Kaspi 2006; Hobbs et al. 2005; Arzoumanian et al. 2002). Moreover, alignment of the NS spin and kick was inferred for the Crab and Vela pulsars (Kaplan et al. 2008; Ng & Romani 2007) and several other young pulsars (see Wang et al. 2006, and references therein) from comparisons of the direction of proper motion with the projected rotation axis as determined from the symmetry axis of the pulsar wind nebula on X-ray images. The same conclusion was drawn for samples of radio pulsars from the linear polarization of the pulses, whose position angle reflects the spin direction (Johnston et al. 2005; Rankin 2007). However, the Crab and Vela pulsars may not be good cases for determining misalignments because they are moving at smaller speeds than the average pulsar population, and therefore the unknown velocity of the progenitor implies a bigger uncertainty. On the other hand, also the radio data do not seem to make a clear case for a general alignment of spin and kick directions in the reference frame of the progenitor's motion (Johnston et al. 2007).

Analysing the observational information, in particular the characteristics of NS binaries, Lai et al. (2001) concluded that the NSs received their kicks most probably at the time of the SN explosion. A large variety of mechanisms for natal kicks has been proposed, either by hydrodynamical effects linked to large-scale asymmetries of the SN explosion (e.g., Herant 1995; Burrows & Hayes 1996; Janka & Müller 1994; Thompson 2000; Scheck et al. 2004, 2006) or by anisotropic neutrino emission from the nascent NS (e.g., Chugai 1984; Burrows & Woosley 1986; Socrates et al. 2005). However, it is very difficult to produce even only a one-percent global dipole asymmetry of the neutrino emission, which is needed for a kick of $300\,\mathrm{km\,s^{-1}}$. For this to be possible one has to invoke controversial assumptions like very strong global dipolar magnetic fields inside the NS ($\gtrsim 10^{16}\,\mathrm{G}$; e.g., Arras & Lai 1999), arguable neutrino properties (e.g., sterile neutrinos, large neutrino magnetic moments; e.g., Fuller et al. 2003), or unsettled mechanisms to create strong emission asymmetries in the neutrinospheric region (e.g., Socrates et al. 2005).

On the basis of 2D SN models Scheck et al. (2004, 2006) argued that the standing accretion shock instability (SASI; Blondin et al. 2003; Foglizzo & Tagger 2000; Foglizzo 2002), which grows after shock stagnation and the beginning SN explosion causing large global non-radial asymmetry of the accretion flow to the NS can lead to kicks of typically several hundred $\mathrm{km\,s^{-1}}$ and even more than $1000\,\mathrm{km\,s^{-1}}$ if the dipole ($\ell = 1$) component of the flow and matter distribution asymmetry is sufficiently strong. Blondin & Mezzacappa (2007) showed in idealized, stationary-accretion setups that SASI spiral modes may also have the potential to generate pulsar spin periods consistent with observations. In this chapter we present the first simulations of SN explosions from core bounce to $\sim$1.5 s later that confirm the potential of SASI-induced asymmetries to produce typical NS kicks in the more realistic 3D environment of collapsing stellar cores.

5.1 Grid and Simulation Setup

In this section, we only discuss the grid geometry and how the simulations are set up. Additional physics treatments used in these simulations are already discussed in details in Section 3.4.

5.1.1 Explosion Simulation

We employed the axis-free overlapping "Yin-Yang" grid in spherical polar coordinates described in Section 3.2 and Wongwathanarat et al. (2010). Our standard grid configuration consists of $400(r)\times47(\theta)\times137(\phi)\times2$ grid cells corresponding to an angular resolution of 2° and covering the full 4π solid angle. The lower angular resolution grid configuration consists of $400(r) \times 20(\theta) \times 56(\phi) \times 2$ corresponding to an angular resolution of 5°. The radial grid has a constant spacing of 0.03 km up to $r \approx 100$ km. Beyond this radius the radial grid is logarithmically spaced. The outer grid boundary R_{ob} is at 18000 km, which is sufficient to prevent the SN shock from leaving the computational domain during the simulated time. Hydrostatic equilibrium is assumed at the inner grid boundary R_{ib}, while a free outflow boundary condition is imposed at the outer grid boundary.

We have investigated two $15\,M_{\odot}$ and a $20\,M_{\odot}$ progenitor models: W15, L15, and N20. The W15 model is based on the non-rotating $15\,M_{\odot}$ progenitor s15s7b2 of Woosley & Weaver (1995), and the L15 model is based on a star evolved by Limongi et al. (2000). The N20 progenitor was computed by Shigeyama & Nomoto (1990). The two $15\,M_{\odot}$ progenitor models were followed through collapse to 15 ms after bounce with the Prometheus-Vertex code in one dimension (A. Marek and R. Buras, private communication). Using the same code, the N20 progenitor was followed only until 11 ms after bounce. To break spherical symmetry, random seed perturbations of 0.1% are imposed on the radial velocity (v_r) field. Explosions with chosen energy are artificially initiated by imposing suitable values of the neutrino luminosities at the inner radial grid boundary. Neutrinos streaming into the computational volume through the boundary interact with matter and deposit energy. Finally, the shock wave is revived leading to a successful explosion.

5.1.2 Long-time Simulation

At the end of the explosion simulations, data are mapped onto another computational grid whose radial inner and outer boundary are placed at 500 km and 3.3×10^8 km, *i.e.,* near the stellar surface. At the inner grid boundary we employed a spherically symmetric neutrino-driven wind inflow because this wind is still present when we stopped the simulations of the explosion phase. Since the inflow is spherically symmetric it will not affect the anisotropic distribution of the ejecta that we would like to investigate. The hydrodynamic inflow quantities are acquired from the angular averaged flow properties at 500 km at the mapping time. We kept the inflow profile

Table 5.1: Explosion and NS properties for all of our simulated models at the end of the explosion phase (1.3 s or 1.4 s after bounce).

Model	$M_{\rm ns}$ [$M_\odot$]	$t_{\rm exp}$ [ms]	$E_{\rm exp}$ [B]	$v_{\rm ns}$ [km/s]	$a_{\rm ns}$ [km/s^2]	$v_{{\rm ns},\nu}$ [km/s]	$v_{\rm ns}^{\rm long\,\star}$ [km/s]	$a_{\rm ns}^{\rm long\,\star}$ [km/s^2]	$J_{\rm ns,46}$ [g cm^2/s]	$\alpha_{\rm sk}$ [°]	$T_{\rm spin}$ [ms]
W15-1	1.37	246	1.12	331	175	3	528	47	1.51	117	652
W15-2	1.37	248	1.13	405	144	1	575	49	1.56	58	632
W15-3	1.36	250	1.11	266	126	1	-	-	1.13	105	864
W15-4	1.38	272	0.94	262	136	4	-	-	1.27	43	785
W15-5-lr	1.40	270	0.97	128	72	1	-	-	2.29	141	440
L15-1	1.58	421	1.13	161	66	5	230	20	1.89	148	604
L15-2	1.51	381	1.74	78	3	1	96	4	1.04	62	1041
L15-3	1.62	477	0.84	31	0	1	-	-	1.55	123	750
L15-4-lr	1.70	703	0.55	146	152	4	-	-	1.64	100	743
N20-1-lr	1.53	348	0.83	175	62	30	-	-	2.81	155	393

* The NS velocity and acceleration given in the eighth and ninth column with the superscript "long" are computed at 3.3 or 3.4 s after bounce in our long-time simulations.

constant for another 2 s of the evolution time and applied a free outflow boundary condition afterwards. The outer boundary condition remains a free outflow boundary condition at all times. Keeping the angular grid resolution unchanged and increasing the number of radial zones our computational grid consists of $1200(r) \times 47(\theta) \times 137(\phi) \times 2$ grid cells. The radial resolution corresponds approximately to $\Delta r/r$ of 0.01.

5.2 Computed Models

We have computed, in total, 10 models, for which we varied the initial seed perturbation pattern or the neutrino luminosities and thus the resulting explosion energy. The evolution is followed until 1.3 s after bounce for the W15 and N20 progenitor models, while the L15 model is simulated until 1.4 s postbounce. Our models W15-1,W15-2, and W15-3 differ only by the initial seed perturbations. Models which are simulated using the lower angular grid resolution (5°) are denoted with the suffix "lr" after their model names. In addition, models W15-1, W15-2, L15-1, and L15-2 are evolved beyond 1.3 s after bounce by means of our long-time simulations until the SN shock leaves the computational domain.

5.3 Neutron star kicks

5.3.1 Simulation results

Figure 5.3 shows snapshots of our results from model W15-2 at four different epochs: 140, 248, 515 ms, and 1.3 s after bounce. The delayed explosion is triggered by neutrino heating around the NS. At $\sim$ 100 ms, small Rayleigh-Taylor mushrooms grow from the imposed seed perturbation in the convectively unstable layer between the forming PNS and the SN shock. These high-entropy bubbles start rising, merge, sinking, and rising again. Consequently, these bubbles grow in angular size. Aided by convective overturn and the SASI the explosion sets in

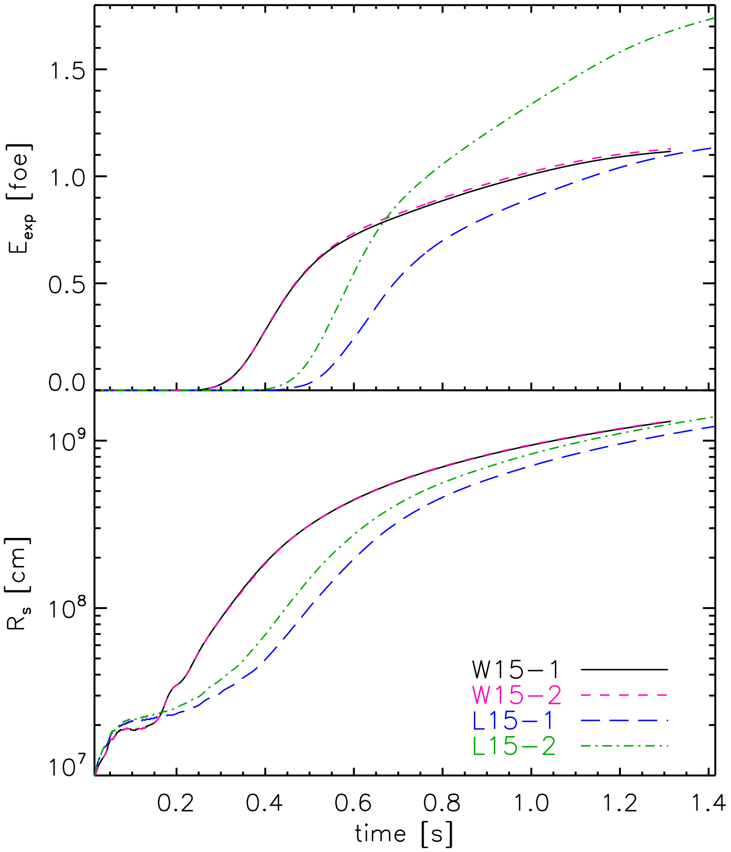

Figure 5.1: Time evolution of the SN explosion energy E_{exp} (*top*) and of the average shock radius R_{s} for models W15-1, W15-2, L15-1, and L15-2. Since models W15-1 and W15-2 differ only in the initial random seed perturbations of the radial velocity field, the results for these models are essentially identical and the short-dashed and solid lines lie on top of each other. Despite the similarity of the global parameters, both models develop different explosion asymmetries and neutron star kicks (see Table 5.1 and Fig. 5.2).

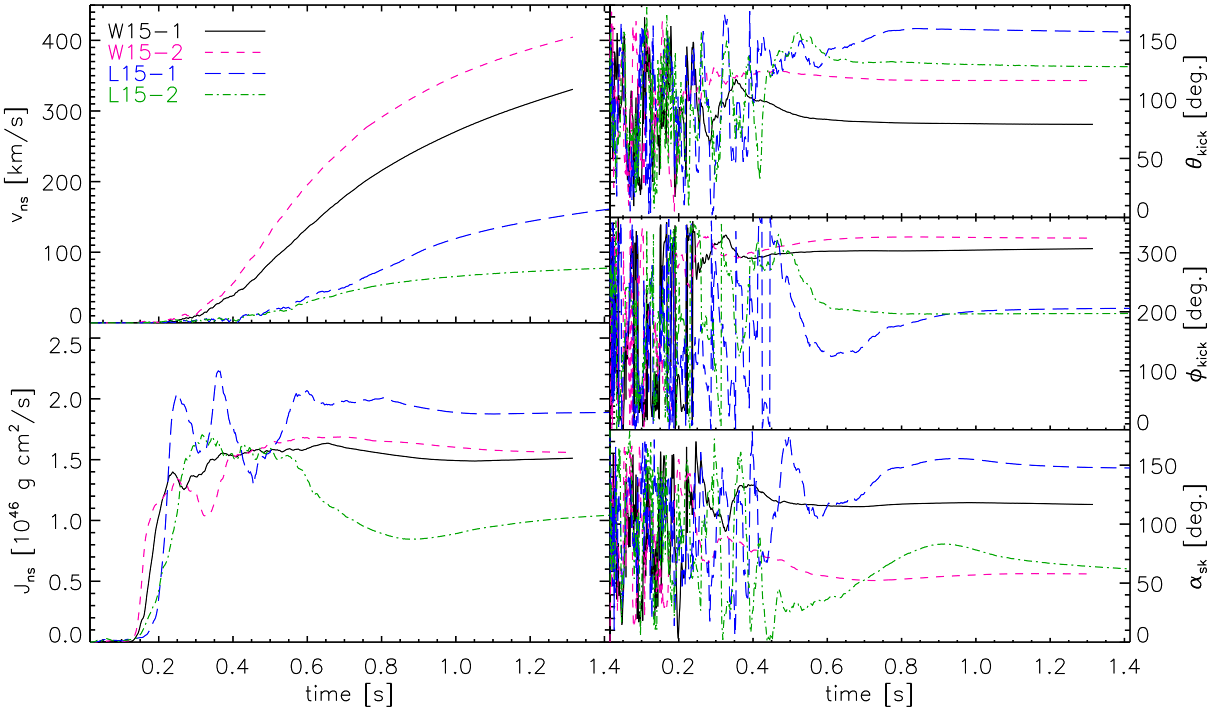

Figure 5.2: Time evolution of NS velocity $v_{\rm ns}$ (*top-left*), angular momentum $J_{\rm ns}$ (*bottom-left*), latitudinal (*top-right*) and azimuthal (*middle-right*) angles of the NS kick vector, $\theta_{\rm kick}$ and $\phi_{\rm kick}$, respectively, and the angle $\alpha_{\rm sk}$ between the NS spin and kick directions (*bottom-right*).

at 248 ms postbounce. For identifying the explosion epoch, we calculated the explosion energy $E_{\rm exp}$ as the sum of the total (*i.e.,* internal plus kinetic plus gravitational) energy for all grid cells where this energy is positive. We can then define the explosion time $t_{\rm exp}$ as the moment at which the computed explosion energy exceeds 10^{48} erg. Figure 5.1 shows the time evolution of the explosion energy and the average SN shock radius. The figure shows that the explosion time roughly corresponds to the time when the average shock radius exceeds 400-500 km. At this time, the NS starts accelerating and its velocity starts growing as can be seen in Figure 5.2 where we show the time evolution of the NS kick velocity $v_{\rm ns}$, NS angular momentum $J_{\rm ns}$, lateral and longitudinal angles of the kick direction ($\theta_{\rm kick}$ and $\phi_{\rm kick}$, respectively), and the angle $\alpha_{\rm sk}$ between spin and kick directions. The calculation of $J_{\rm ns}$ will be addressed in Section 5.3.6. A cross-sectional view of the entropy distribution clearly shows dipolar asymmetry with, dense low-entropy material concentrated more on the hemisphere where the kick vector lies (Fig. 5.3, third row). At a later stage, the ejecta undergo mainly radial expansion and all structures freeze in. An entropy slice shows the spherically symmetric neutrino-driven wind embedded within the anisotropic wind-termination shock. On the side where the explosion is stronger, which is visible by higher entropy behind the SN shock and faster expansion (upper left in last row of Fig. 5.3), the wind is shocked to higher entropies since it passes the termination shock at larger radii.

Table 5.1 summarizes the explosion and NS properties which we computed in a post-processing step for all models after the end of the simulations. The NS mass $M_{\rm ns}$ is defined by the baryonic mass enclosed by the NS radius $R_{\rm ns}$, which is the radius where the density is 10^{11} g/cm^3. In

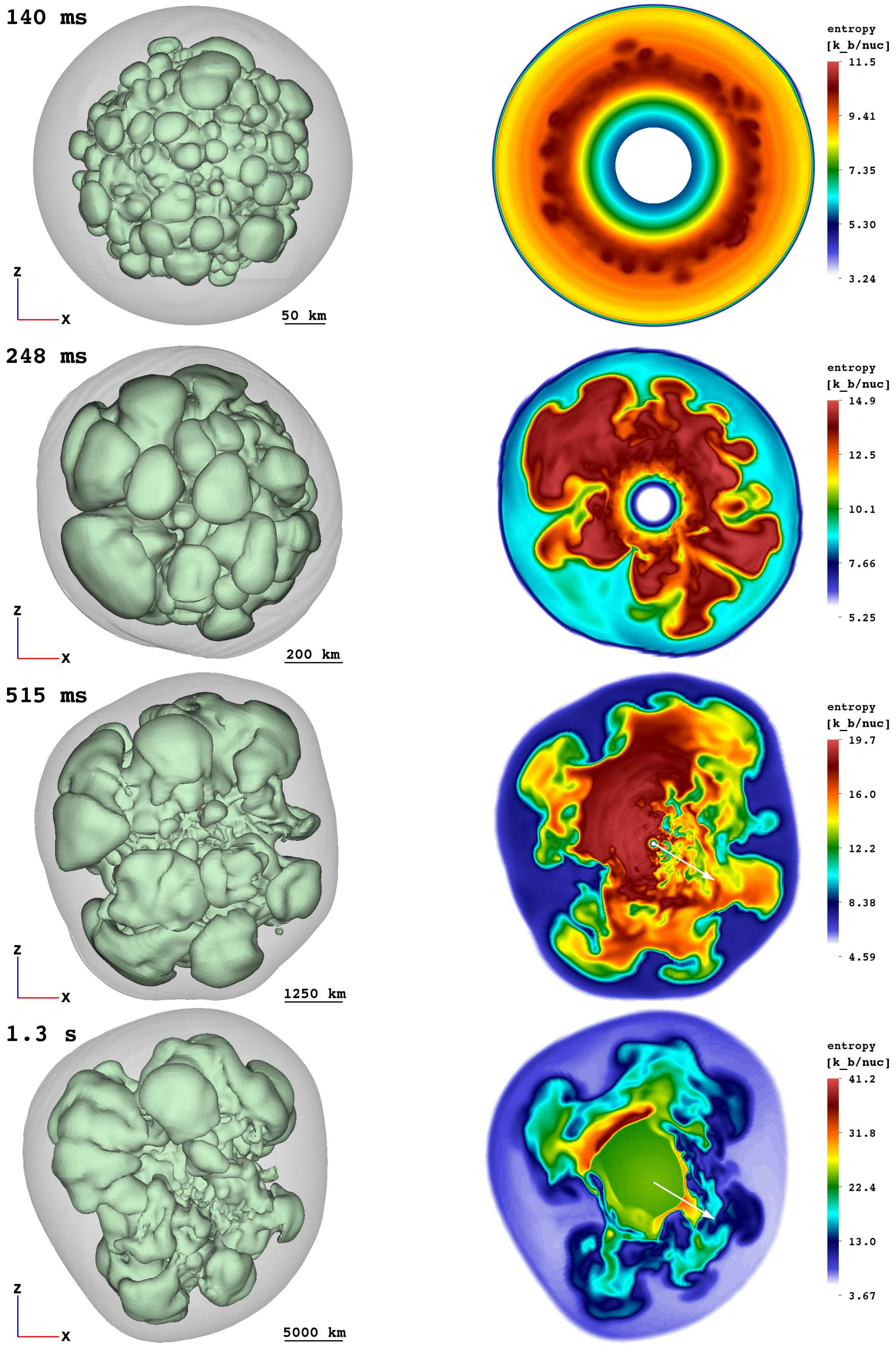
140 ms
z
x
50 km
entropy
[k_b/nuc]
11.5
9.41
7.35
5.30
3.24
248 ms
z
x
200 km
entropy
[k_b/nuc]
14.9
12.5
10.1
7.66
5.25
515 ms
z
x
1250 km
entropy
[k_b/nuc]
19.7
16.0
12.2
8.38
4.59
1.3 s
z
x
5000 km
entropy
[k_b/nuc]
41.2
31.8
22.4
13.0
3.67

Figure 5.3: Entropy-isosurfaces (left) of the SN shock (grey) and the high-entropy bubbles (green), and entropy distribution in a cross-sectional plane (right) at t =140 ms,248 ms,515 ms and 1.3 s for model W15-2. Small Rayleigh-Taylor mushrooms start growing at $\sim$ 100 ms (first row). The rising high-entropy bubbles merge and form even larger bubbles by the time the explosion sets in (second row). The NS starts accelerating due to the asymmetric distribution of the ejecta, and the acceleration reaches its maximum at $\sim$ 500 ms (third row). At this epoch, the ejecta show a clear dipolar distribution with more dense low-entropy material concentrated in the hemisphere containing the kick direction. The NS kick direction has already settled and its *projection* onto the xz-plane is shown by the white arrows pointing to the lower right. The last row shows the entropy structure at the end of the simulation. Spherically symmetric neutrino-driven wind material is visible in green color inside the region enclosed by the wind termination shock.

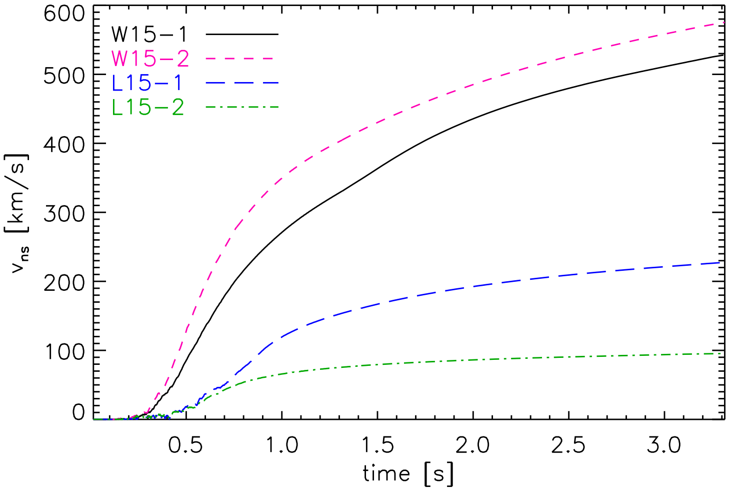

Figure 5.4: Long-time evolution of the NS velocity for models W15-1, W15-2, L15-1, and L15-2, respectively. The NS in model W15-2 is accelerated to 575 km/s. Note also the saturation of the velocity curves for model L15-1 and L15-2.

estimating the NS recoil velocities, we assume conservation of linear momentum of the system. Since the NS in our simulations is excised it cannot move when it absorbs momentum from surrounding gas as if it had an infinite inertial mass (like a wall reflecting a bouncing ball). Nevertheless, following Scheck et al. (2006), the NS velocity $\mathbf{v}_{\rm ns}$ can be estimated from the negative of the total linear momentum of the ejecta gas as

$$\mathbf{v}_{\rm ns}(t) = -\mathbf{P}_{\rm gas}(t)/M_{\rm ns}(t)\,, \tag{5.1}$$

where $\mathbf{P}_{\rm gas} = \int_{R_{\rm ns}}^{R_{\rm ob}} {\rm d}V\,\rho\mathbf{v}$.

In our simulations, we find NS kick velocities ranging from $\sim$ 30 km s^{-1} (L15-3) to $\sim$ 400 km s^{-1} (W15-2) at 1.3 s (1.4 s) after bounce. The NS acceleration $a_{\rm ns}$ can then be computed by differentiating the NS velocity calculated from Eq. (5.1) and is also given in Table 5.1. Note that the NS velocity at 1.3 s (1.4 s) after bounce is not the final one since the NS is still accelerating, except for models with low kick velocity (L15-2 and L15-3). Therefore, we also give the NS velocity and acceleration at 3.3 s (3.4 s) after bounce (denoted with the superscript “long” in the seventh and eighth column of Table 5.1) for the models of our long-time simulations. Although these simulations extend to a much later times we do not compute the NS velocity beyond 3.3 s (3.4 s) after bounce, because of the inner grid boundary is moved out during the simulations and because of the free outflow boundary condition whereby anisotropic momentum flow across the inner grid boundary which has to be accounted for may occur. We find that the NS in model W15-2 is accelerated to a velocity of 575 km s^{-1}, and we show the time evolution of the NS velocity from 15 ms after bounce to 3.3 s (3.4 s) after bounce for models W15-1, W15-2, L15-1, and L15-2 in Fig. 5.4.

Figure 5.5 illustrates the morphology of the SN shock and of the high-entropy bubbles. It shows entropy-isosurfaces at 1.3 s for model W15-2 which possesses the highest NS kick velocity. The ray-casting image of the density distribution (*middle* panel) corresponding roughly to a density projection onto the plane normal to the kick and spin vector, shows dense clumps of matter concentrated mostly in the direction of NS motion. Moreover, the NS position is clearly

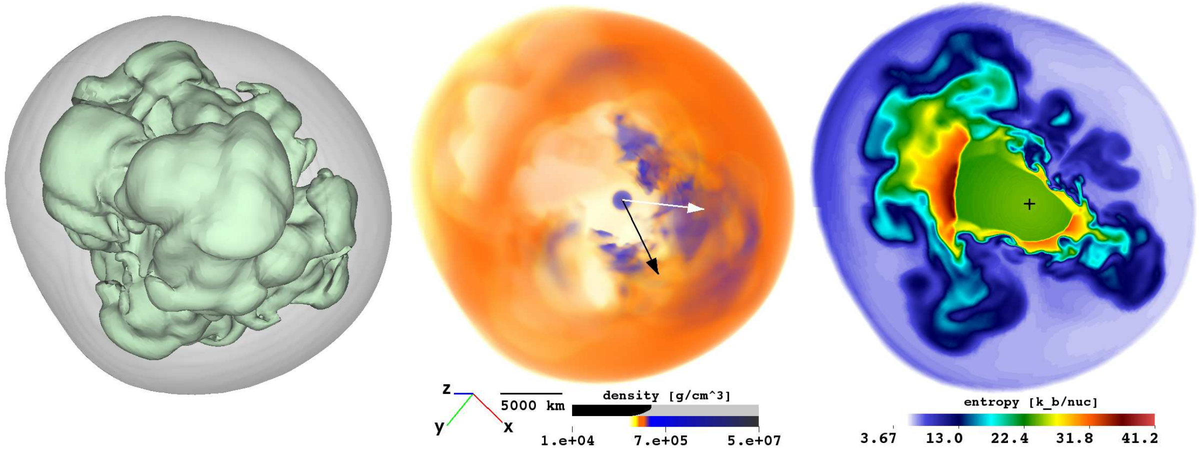

Figure 5.5: Entropy-isosurfaces of the SN shock and the high-entropy bubbles (*left*), ray-casting image of the density (*middle*), and entropy distribution in a cross-sectional plane through the center (*right*) at $t = 1.3\,\mathrm{s}$ after bounce for model W15-2. The outer boundaries coincide with the shock surface, the viewing direction is normal to the plane of the NS kick and spin vectors, which also define the plane for the entropy slice. The kick and spin directions are indicated by the white and black arrows, respectively, in the *middle figure*. The NS location is marked by a black cross in the *right plot* and is clearly displaced from the geometrical center of the expanding shock. The SN shock has an average radius of 13000 km (a length of 5000 km is given by a yardstick below the *middle image*) but shows a pronounced dipolar deformation, which is clearly visible from the color asymmetry of the postshock gas between the lower right (weaker shock with minimum radius of 11000 km) and upper left (stronger shock with maximum radius of 15000 km) directions. The *middle plot* corresponds roughly to the projection of the density distribution on a plane perpendicular to the line of sight. Dilute bubble regions are light-colored in white and yellow, while dense clumps appear more intense in reddish and bluish hues. The blue circle around the NS represents the dense inner region of the spherically symmetric neutrino-driven wind. This wind is visible in green in the *right image* and is bounded by the aspherical wind termination shock. The wind is shocked to higher entropies on the left side, where it passes the termination shock at larger radii because of the faster expansion of the preceding SN ejecta.

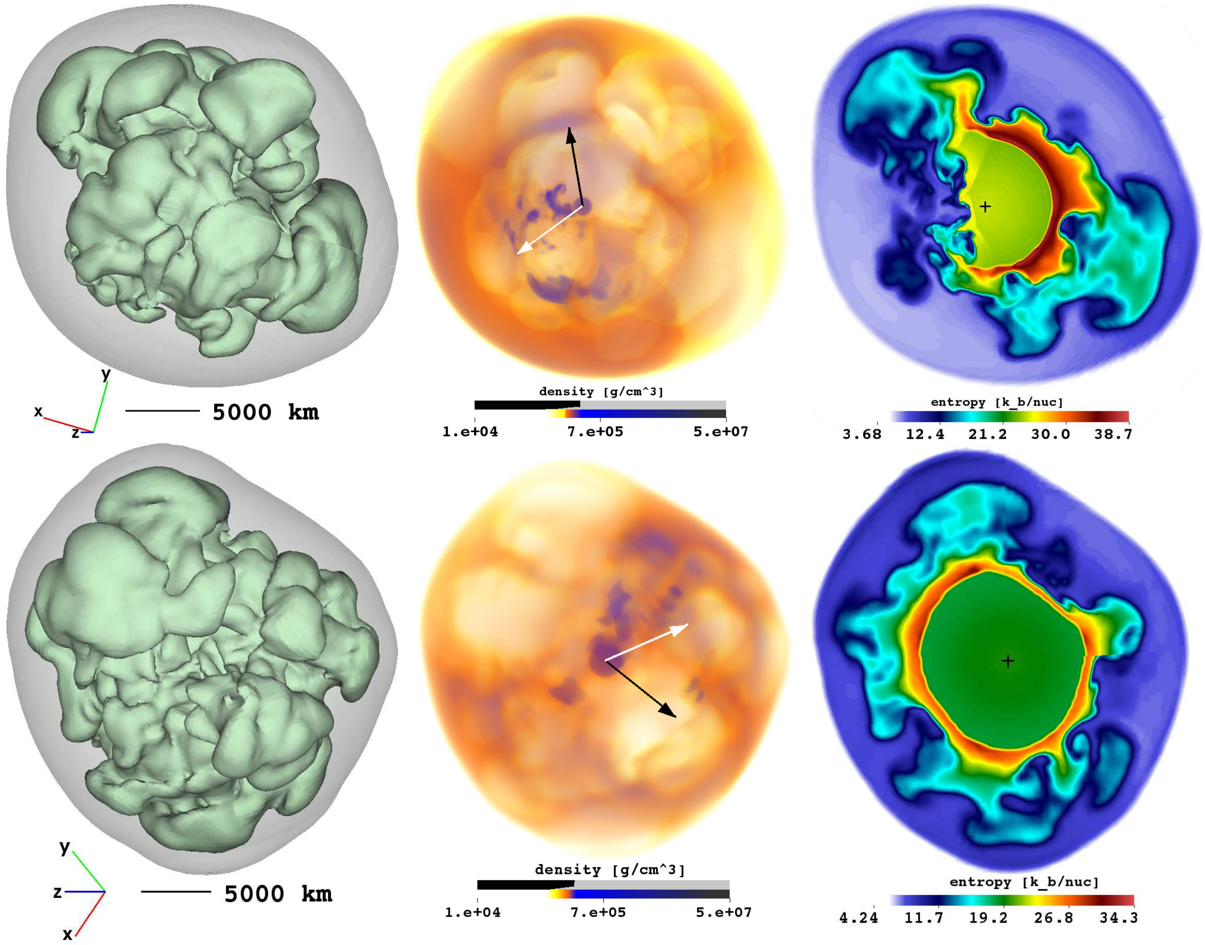
y
x
z
5000 km
density [g/cm^3]
1.e+04
7.e+05
5.e+07
entropy [k_b/nuc]
3.68
12.4
21.2
30.0
38.7
y
z
x
5000 km
density [g/cm^3]
1.e+04
7.e+05
5.e+07
entropy [k_b/nuc]
4.24
11.7
19.2
26.8
34.3

Figure 5.6: Same as Figure 5.5 but for models W15-1 and L15-2. The SN shock has an average radius of 13000 km and 14000 km for models W15-1 and L15-2, respectively. The NS is clearly displaced from the geometrical center of the expanding shock. The kick vector is pointing to the lower left direction for model W15-1, while the NS does not show any clear displacement and remains roughly at the center for model L15-2, which has a small kick velocity compared to model W15-1.

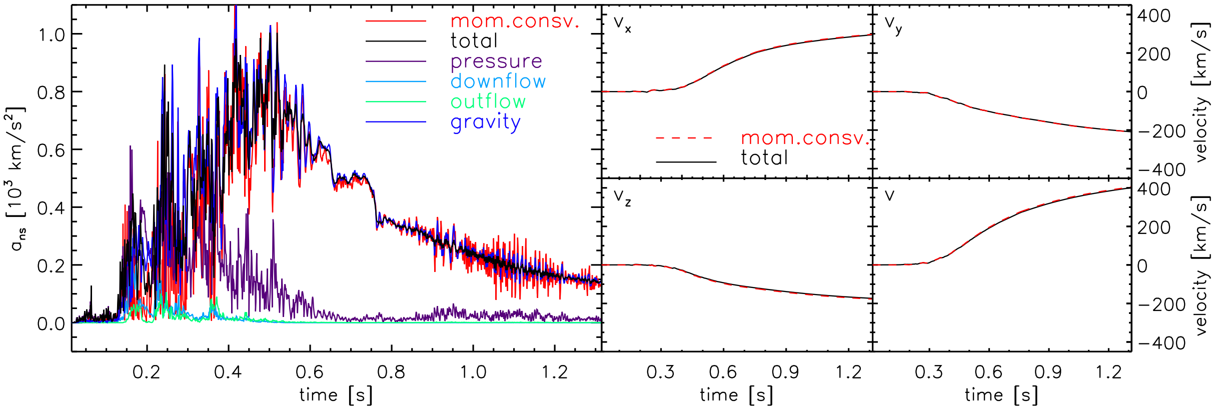

Figure 5.7: Time evolution of the NS acceleration of model W15-2 computed as the negative derivative of the total linear momentum of the gas surrounding the NS by assuming momentum conservation (red; denoted as "mom.consv."), and from the integration of hydrodynamical forces acting on the sphere with radius $1.3R_{\mathrm{ns}}$ around the PNS (black; denoted as "total"). Also shown are contributions from each term in Eq. (5.2), corresponding to momentum transfers by downflows (light blue), outflows (green), anisotropic pressure forces (purple), and gravitational attraction from asymmetric ejecta (blue). The latter effect clearly dominates over long parts of the evolution. Shown in the right panel are the corresponding NS velocity for all three components and the magnitude of the total NS velocity. Note that the two lines in each of these panels lie on top of each other.

displaced from the geometrical center of the ejecta. The same effect is shown in Figure 5.6 for model W15-1 (*top* panel). Looking at the density distribution of the ejecta it is obvious that the kick vectors always point towards the direction with the highest concentration of dense clumps. However, this effect cannot be seen in the case of model L15-2, because it possesses only a fairly small kick velocity compared to model W15-1 or W15-2. The shock expansion in model L15-2 is equally strong in all directions driven by hot bubbles that have nearly the same size. Correspondingly, the wind-termination shock shows relatively little deformation. Note that although there is a visible mass concentration in the kick direction, the opposite hemisphere contains clumps as well, though less strongly concentrated.

5.3.2 Kick mechanism: theory and toy models

The NS acceleration associated with asymmetric SN explosions is achieved by hydrodynamic and gravitational forces. This will be detailed below. The acceleration proceeds in three steps:

(1) When violent convective mass flows and SASI sloshing motions conspire to stir the postshock layer, an anisotropy of the mass-energy distribution around the PNS is created. Convective downdrafts, channelling gas accreted through the stalled shock into the neutrino-heating region, get deflected to feed an asymmetric pattern of high-entropy bubbles. The energy-loaded bubbles are created, disappear again, and reappear in a quasi-chaotic way to become smaller or larger, absorbing less or more neutrino energy. This stochastic bubble formation, however, does not cause an appreciable recoil of the NS (see Figure 5.2).

(2) When the explosion sets in, the shock and postshock gas begin to expand aspherically, driven by the asymmetric inflation of the bubbles. The ejecta gas therefore gains radial

momentum and its c.o.m. begins to shift away from the coordinate origin (Figs. 5.3, 5.5 and 5.6, right panels): The ejecta shell acquires a net linear momentum because of different strengths of the explosion in different directions. The initial *energy and mass asymmetry* is thus converted to a *momentum asymmetry* by the conversion of thermal to kinetic energy through hydrodynamical forces. When the expansion timescale becomes shorter than the timescale of lateral mixing, the asymmetric ejecta structures freeze in.

(3) Because of linear momentum conservation, the NS must receive the negative of the total momentum of the anisotropically expanding ejecta mass. Hydrodynamic pressure forces alone cannot achieve the NS acceleration (Scheck et al. 2006). As long as accretion downdrafts reach the NS, momentum is transferred by asymmetric gas flows. Stronger accretion on the weaker side of the blast and more mass loss in the neutrino-driven wind on the other side can cause a recoil opposite to the main explosion direction. However, the largest kick contribution, which continues even after accretion has ended and the wind has become spherical (Fig. 5.2), results from the gravitational pull of the anisotropic shell of ejecta (Scheck et al. 2006).

To elaborate on this point and to check our estimation of the NS recoil velocity computed from Eq. (5.1), we have also performed an analysis of the different contributions to the NS kick by considering the forces acting on a sphere of radius $r_0 = 1.3R_{\rm ns}$. Following Scheck et al. (2006) the time-derivative of the NS momentum can be deduced from the Euler equations as

$$\dot{\mathbf{P}}_{\rm ns} \approx -\oint_{r=r_0} \mathcal{P}\, d\mathbf{S} - \oint_{r=r_0} \rho \mathbf{v} v_r\, dS + \int_{r>r_0} G M_{\rm ns} \frac{\mathbf{r}}{r^3}\, dm. \tag{5.2}$$

Consequently, the NS acceleration is $\mathbf{a}_{\rm ns} = \dot{\mathbf{P}}_{\rm ns}/M_{\rm ns}$ and the NS velocity $\mathbf{v}_{\rm ns}(t) = \int_0^t dt'\, \mathbf{a}_{\rm ns}(t')$. The first term in Eq. (5.2) accounts for the variation of pressure across the sphere with radius r_0. The second term is the flux of momentum flowing through that sphere. This term can be decomposed into a *downflow* and an *outflow* for the sign of the radial velocity v_r being *negative* or *positive*, respectively. The third term is the contribution from the long-range gravitational force acting on the NS due to the anisotropic mass distribution outside the sphere. Note that a change of the radius of evaluation in a range around $r_0 = 1.3R_{\rm ns}$ leads to variation of the weights of the different forces but gives the same result for the inferred effect.

Figure 5.7 compares $a_{\rm ns}$ and $v_{\rm ns}$ calculated by the two different methods: the requirement of total momentum conservation (Eq. (5.1)) and the integration of the responsible hydrodynamical and gravitational forces in Eq. (5.2). Both the NS acceleration and velocity show excellent agreement between the two methods. At around 200-300 ms postbounce, both the force by the anisotropic pressure distribution and the gravitational pull account for the total acceleration on significant levels. However, at later stages, the gravitational force term starts to dominate and therefore contributes most importantly to the final NS velocity. We also find that in 3D models the direct hydrodynamical momentum transfer by downflows and outflows to the NS is much less important than in 2D. While in 2D the toroidal nature of all structures due to the existence of the symmetry axis favors the formation of large hemispheric differences with inflow to the NS dominating in one hemisphere and outflow in the other (corresponding to an $\ell = 1$ geometry), the 3D downflow and outflow pattern is characterized by higher multipoles. The momentum transfer by inflows thus compensates the opposite one by outflows on smaller angular scales. The gravitational drag by the asymmetric ejecta distribution is therefore the dominant mediator of the NS acceleration in a time-integrated sense, although it is not necessarily the only important effect, in particular not during the very early phase of the NS recoil and not in 2D.

Why can our models produce kick velocities of $\sim$500 km s^{-1}, possibly even much beyond, by a hydrodynamical mechanism, while this appeared to be highly disfavored even for a dipolar ejecta asymmetry in an analysis of 2D explosion simulations by Janka & Müller (1994)? The crucial difference results from the fact that Janka & Müller (1994) discussed the kicks as originating from an *impulsive event*, happening during a short period of a few hundred milliseconds around the onset of the explosion. In their estimates they therefore considered the momentum asymmetry of the ejecta shell during this early phase, assuming that the kick is over when the accretion ends. In contrast, in the scenario discussed here the NS acceleration is a *long-duration* phenomenon, which continues for several seconds, promoted by the long-range gravitational force.

5.3.3 Analytic estimates of the kick magnitude[1]

Order-of-magnitude estimates of the kick velocities that can be expected by explosion asymmetries acting on the NS through anisotropic gravitational forces can be obtained by considering two different, simple situations (similar considerations were also published by Nordhaus et al. 2010).

In the first case we assume a hemispheric asymmetry of the mass distribution, in which the expanding, spherical ejecta shell contains an extra clump-like mass Δm in one hemisphere, while a corresponding mass deficiency exists in the other hemisphere. The shell with radius r_s expands with a constant velocity of v_s, beginning at a radius r_i. If the NS is displaced by a distance s from the center of the shell ($s = 0$ at $t = 0$), the gravitational forces lead to a NS velocity $v_\mathrm{ns} = \dot{s}$ via an acceleration $a_\mathrm{ns} = \ddot{s}$ given by

$$\ddot{s} = \frac{\mathrm{d}v_\mathrm{ns}}{\mathrm{d}t} = G\Delta m \left[\frac{1}{(r_\mathrm{s} - s)^2} + \frac{1}{(r_\mathrm{s} + s)^2} \right] . \tag{5.3}$$

Using $r_\mathrm{s} = r_\mathrm{i} + v_\mathrm{s} t$ and assuming $s \ll r_\mathrm{s}$ at all times, the integration of Eq. (5.3) from $t = 0$ to $t = \infty$ yields:

$$v_\mathrm{ns} \approx \frac{2G\Delta m}{r_\mathrm{i} v_\mathrm{s}} \approx 2700\,\frac{\mathrm{km}}{\mathrm{s}}\,\frac{\Delta m_{-3}}{r_{\mathrm{i},7} v_{\mathrm{s},8}} , \tag{5.4}$$

where Δm is normalized by $10^{-3}\,M_\odot$, r_i by 10^7 cm, and v_s by 10^8 cm s^{-1}. A $10^{-3}\,M_\odot$ hemispheric asymmetry of a shell expanding with a constant velocity of 1000 km s^{-1} can thus drag the NS to a velocity of 2700 km s^{-1}. Ejecta asymmetries can therefore very effectively mediate a long-lasting pull on the NS, which is accelerated in the direction of the higher mass concentration. According to Eq. (5.4) the kick becomes larger for a lower expansion velocity, because the gravitational drag from the asymmetric ejecta shell then acts for a longer time. While a value of 10^8 cm s^{-1} is at the lower end, an anisotropy of $10^{-3}\,M_\odot$ means an asymmetry of the mass distribution of $\lesssim$1% in a shell which typically contains $10^{-1}\,M_\odot$ or more at the interesting times. Note that the first-order terms s/r_s cancel in Eq. (5.3), *i.e.,* the NS recoil is affected by the NS motion and displacement from the explosion center only at the level of second-order correction terms of $s/r_\mathrm{s} \ll 1$.

In the second case we do not consider a hemispheric mass difference but a difference of the expansion velocity of clumps Δm in the ejecta shell in both hemispheres. This means that we assume that these clumps propagate away from the center of the blast according to $r_{\mathrm{s},1} = r_\mathrm{i} + v_{\mathrm{s},1}t$ and $r_{\mathrm{s},2} = r_\mathrm{i} + v_{\mathrm{s},2}t$ with $v_{\mathrm{s},1} < v_{\mathrm{s},2}$. Taking s to be again the displacement of the NS from the blast center, the compact remnant in this situation experiences a gravitational acceleration

---

[1] The analysis in this subsection is due to Hans-Thomas Janka, but is included here to explain the NS kick results.

$$\ddot{s} = \frac{\mathrm{d}v_\mathrm{ns}}{\mathrm{d}t} = G\Delta m \left[\frac{1}{(r_{\mathrm{s},1} - s)^2} - \frac{1}{(r_{\mathrm{s},2} + s)^2} \right] . \tag{5.5}$$

To lowest order in $s/r_\mathrm{s} \ll 1$ time integration from 0 to ∞ leads to

$$\begin{aligned} v_\mathrm{ns} \approx \frac{G\Delta m}{r_\mathrm{i}} \frac{v_{\mathrm{s},2} - v_{\mathrm{s},1}}{v_{\mathrm{s},1}\, v_{\mathrm{s},2}} &\approx \frac{G\Delta m}{r_\mathrm{i}} \frac{\Delta v_\mathrm{s}}{\bar{v}_\mathrm{s}^2} \\ &\approx 1300\, \frac{\mathrm{km}}{\mathrm{s}} \frac{\Delta m_{-3}}{r_{\mathrm{i},7}\, \bar{v}_{\mathrm{s},8}} \frac{\Delta v_\mathrm{s}}{\bar{v}_\mathrm{s}} , \end{aligned} \tag{5.6}$$

where we have introduced the definitions $\Delta v_\mathrm{s} = v_{\mathrm{s},2} - v_{\mathrm{s},1}$ and $\bar{v}_\mathrm{s} = \sqrt{v_{\mathrm{s},1} v_{\mathrm{s},2}}$. In the last expression we have again normalized Δm by $10^{-3}\, M_\odot$, r_i by 10^7 cm, and $\bar{v}_\mathrm{s}$ by $10^8\,\mathrm{cm\,s^{-1}}$. The acceleration is opposite to the faster expanding hemisphere, i.e. it is opposite to the direction of the strongest explosion, and of the same order of magnitude as the result given in Eq. (5.4), if we assume a velocity asymmetry of 100%, $\Delta v_\mathrm{s}/\bar{v}_\mathrm{s} \sim 1$. Since this is on a very extreme assumption, and $\Delta v_\mathrm{s}/\bar{v}_\mathrm{s} < 0.5$ seems more realistic, a velocity asymmetry according to Eq. (5.5) is less efficient in accelerating the NS than the mass asymmetry in Eq. (5.3). The first-order correction term in $s/r_\mathrm{s} \ll 1$, which we have suppressed when going from Eq. (5.5) to Eq. (5.6), reads $\mathrm{d}v_\mathrm{ns}^{(1)}/\mathrm{d}t = 2G\Delta m\, s(r_{\mathrm{s},1}^{-3} + r_{\mathrm{s},2}^{-3})$. It is not necessarily small compared to the leading term $\mathrm{d}v_\mathrm{ns}^{(0)}/\mathrm{d}t = G\Delta m\, s(r_{\mathrm{s},1}^{-2} - r_{\mathrm{s},2}^{-2})$, but the corresponding acceleration amplifies the effect of the zeroth-order term, because the displacement by the kick brings the NS closer to the attracting slower parts of the ejecta.

A closer inspection of Eqs. (5.4) and (5.6) clarifies the meaning and implications of the non-impulsive nature of the described recoil mechanism. The instantaneous linear momentum carried by clumps with asymmetric masses or velocities, $P_\mathrm{gas} \sim 2\Delta m\, v_\mathrm{s} \approx 4 \times 10^{38}\, \Delta m_{-3} v_{\mathrm{s},8}\,\mathrm{g\,cm\,s^{-1}}$, is orders of magnitude smaller than the momentum associated with the estimated possible NS kick, $P_\mathrm{ns} = M_{\mathrm{ns},1.5}\, v_{\mathrm{ns},8} \approx 3 \times 10^{41}\,\mathrm{g\,cm\,s^{-1}}$ with $M_{\mathrm{ns},1.5} = M_\mathrm{ns}/1.5\, M_\odot$. No efficient recoil of the NS can thus be achieved by just tapping the instantaneous momentum of the clumps at any time, even if the outward motion of the clumps is brought to a complete halt. Exactly this was the problem with hydrodynamical kicks as impulsive events, which were therefore ruled out as origin of large NS velocities by Janka & Müller (1994) even in cases with extreme asymmetry. Instead, for strong kicks it is necessary to maintain the momentum of the dense clumps in the ejecta shell. The corresponding continuous clump acceleration can happen by hydrodynamical forces, by which internal ejecta energy is converted to kinetic energy. This requires that the ejecta do not expand ballistically yet and thus limit the radial scales and time intervals that can contribute to the pulsar kick. While the clumps are hydrodynamically coupled to the energetic environment they are embedded in, they transfer momentum and energy to the NS through their long-range gravitational drag. The energy thus pumped into the motion of the NS can become quite significant, $E_\mathrm{k,ns} = \frac{1}{2} M_\mathrm{ns} v_\mathrm{ns}^2 \sim 10^{49} M_{\mathrm{ns},1.5} v_{\mathrm{ns},8}^2\,\mathrm{erg}$. This, however, is still a small fraction of the $\sim 10^{51}$ erg of a normal SN explosion.

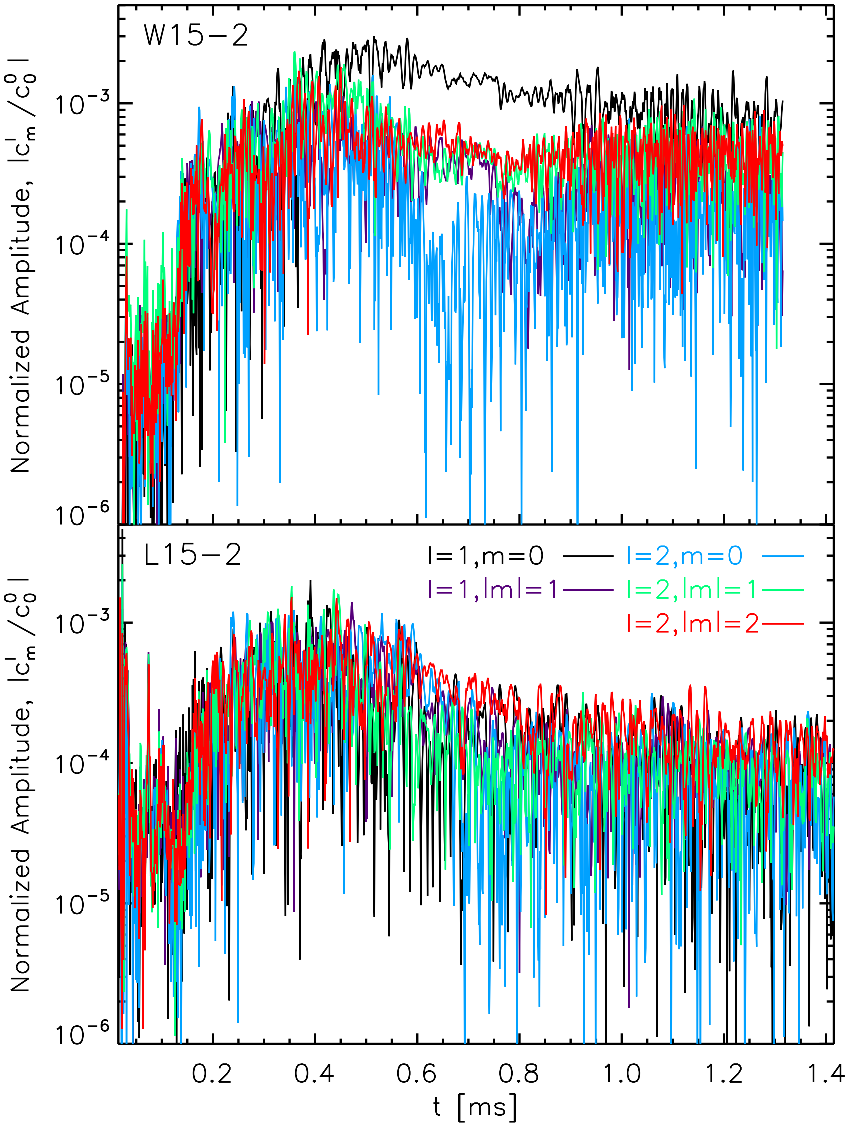

Figure 5.8: Time evolution of the normalized spherical harmonic expansion coefficients for different (ℓ, m) modes computed for the column mass density of models W15-2 (top) and L15-2 (bottom), respectively. The polar axis of the coordinate system chosen for the expansion is aligned with the final NS kick direction. Note the dominance of the $(\ell, m) = (1, 0)$ mode for model W15-2 with the highest kick velocity, while this dominance is absent for model L15-2.

5.3.4 Mode analysis

We perform a mode analysis of the column mass density of the gas in the layer between the NS surface and the SN shock, $D(\theta,\phi) = \int_{R_\mathrm{ns}}^{R_\mathrm{s}} \mathrm{d}r\, \rho(r)$, by decomposing it in spherical harmonics as

$$D(\theta,\phi) = \sum_{\ell=0}^{\infty} \sum_{m=-\ell}^{\ell} c_\ell^m Y_\ell^m(\theta,\phi), \tag{5.7}$$

where c_ℓ^m are the expansion coefficients and the spherical harmonics Y_ℓ^m can be written in terms of the associated Legendre polynomials P_ℓ^m as

$$Y_\ell^m(\theta,\phi) = K_\ell^m P_\ell^m(\cos\theta) e^{im\phi}, \tag{5.8}$$

with

$$K_\ell^m = \sqrt{\frac{2\ell+1}{4\pi}\frac{(\ell-m)!}{(\ell+m)!}}. \tag{5.9}$$

Multiplying Eq. (5.7) by the complex conjugate of the spherical harmonic, Y_ℓ^{m*}, and integrating over the solid angle, the expansion coefficients can be written as

$$c_\ell^m = \int_0^{2\pi} d\phi \int_0^{\pi} d\theta\ \sin\theta\, D(\theta,\phi) Y_\ell^{m*}(\theta,\phi). \tag{5.10}$$

We chose the coordinate system for the expansion such that the polar axis is aligned with the NS kick direction. Before performing the integration of Eq. 5.10, we interpolated, using bilinear interpolation, the surface density computed on the Yin-Yang grid into the new coordinate system. Figure 5.8 shows the resulting expansion coefficients of different (ℓ, m) modes versus time for models W15-2 and L15-2, respectively. The $(\ell, m) = (1, 0)$ mode clearly dominates after 0.4 s postbounce in the case of model W15-2, while this behaviour is absent in model L15-2. The amplitude of the $(\ell, m) = (1, 0)$ mode reaches its maximum at around 500 ms after bounce, approximately at the same time when the NS acceleration reaches its maximum value (Fig. 5.7). This provides a strong support for our proposed kick mechanism since it shows that larger dipolar mass asymmetry results in a larger NS recoil velocity.

The same analysis performed for the surface mass density $\Sigma(\theta,\phi) = \int_{R_\mathrm{ns}}^{R_\mathrm{s}} \mathrm{d}r\, r^2\rho(r)$ yields the same conclusion. We observe a clear dominance of the $(\ell, m) = (1, 0)$ mode for model W15-2 but not for model L15-2. However, as the surface mass density is less suited to quantify the mass asymmetry behind the SN shock, we chose to present the analysis of the column mass density instead. The surface mass density reflects more the morphology of the ejecta and of the SN shock because of the r^2 weighting. As shown in Fig. 5.6 the explosion is stronger in the direction opposite to the NS kick direction, and the SN shock has reached a larger radius in that direction. Integrating the density with the r^2 weighting ends up giving too much weight in the layer near the SN shock and therefore completely dominates the contribution of small dense clumps at smaller radii.

5.3.5 Contribution by anisotropic neutrino emission

We do not expect any significant contribution to the NS kick by anisotropic neutrino emission, because most of the neutrino energy is radiated from the spherically symmetric neutrinosphere.

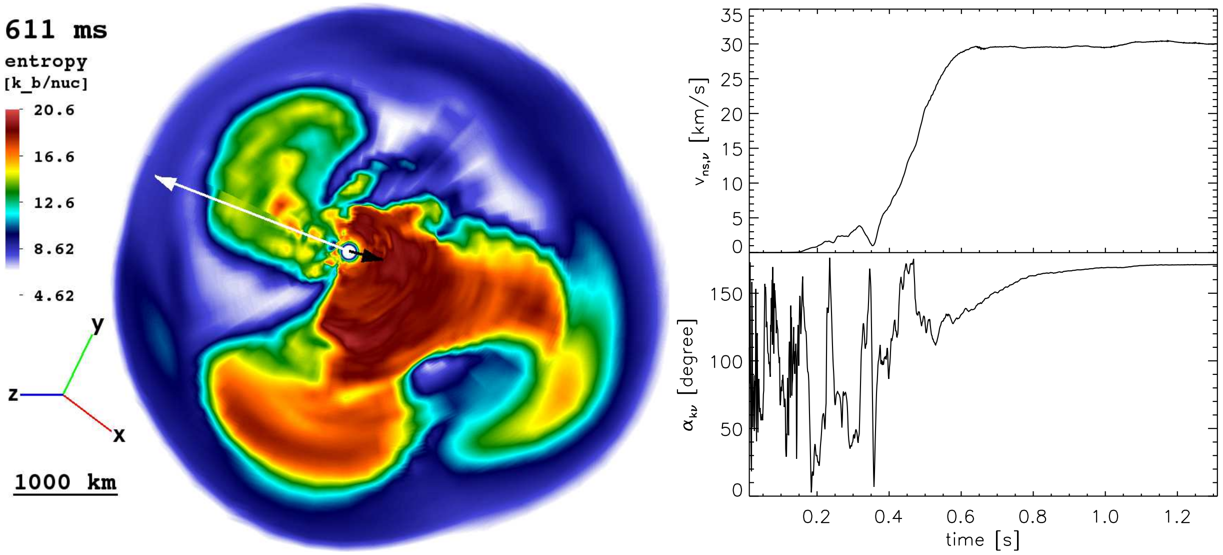

Figure 5.9: Entropy distribution (left) plotted in a cross-sectional plane containing the NS kick velocity v_{NS} due to the anisotropic mass distribution and mass flows, and the NS kick velocity $v_{\mathrm{NS},\nu}$ due to anisotropic neutrino emission for model N20-1-lr at 611 ms postbounce. A length scale of 1000 km is given by a yardstick in the lower left corner of the figure. The NS is clearly displaced in the direction of v_{ns}. The arrows representing v_{ns} and $v_{\mathrm{ns},\nu}$ are scaled according to their magnitudes, which are 175 km/s and 30 km/s, respectively. Obviously, $v_{\mathrm{ns},\nu}$ contributes only little to the final NS kick velocity. The time evolution of $v_{\mathrm{ns},\nu}$ and of the angle $\alpha_{\mathrm{k}\nu}$ between v_{ns} and $v_{\mathrm{ns},\nu}$ are shown in the right panel. Note that $v_{\mathrm{ns},\nu}$ is pointing roughly in opposite direction of v_{ns}.

Following Scheck et al. (2006), we calculated the correction to the NS velocity due to anisotropic neutrino momentum $\mathbf{v}_{\mathrm{ns},\nu}$ as the negative of the integrated neutrino momentum divided by the NS mass, $-\mathbf{P}_\nu/M_{\mathrm{ns}}$. The neutrino momentum is given by

$$\mathbf{P}_\nu(t) = \int_{R_{\mathrm{ib}}<r<R_{\mathrm{ob}}} p_\nu \, \hat{\mathbf{r}} \, dV + \int_0^t dt \oint_{r=R_{\mathrm{ob}}} p_\nu c \, \hat{\mathbf{r}} \, dS \tag{5.11}$$

where $p_\nu = F_\nu/c^2$ is the neutrino momentum density, F_ν is the neutrino energy flux, c is the speed of light, and $\hat{\mathbf{r}}$ is the unit vector in radial direction. In our case, since we apply the ray-by-ray neutrino transport only the radial component of the neutrino momentum exists. The first term integrates the total neutrino momentum on the grid, while the second term accounts for the time-integrated neutrino momentum flux leaving the computational domain at time t.

The computed $v_{\mathrm{ns},\nu}$ for all models are also presented in Table 5.1. The data clearly show that $v_{\mathrm{ns},\nu}$ makes only a tiny correction to the final NS kick velocity and can therefore be considered as negligible for all models except model N20-1-lr whose $v_{\mathrm{ns},\nu}$ is approximately 17% of v_{ns}. Figure 5.9 shows a slice of the entropy distribution for model N20-1-lr at 611 ms after bounce. The slice plane is normal to the a plane spanned by v_{ns} and $v_{\mathrm{ns},\nu}$. The time evolution of $v_{\mathrm{ns},\nu}$ and its angle $\alpha_{\mathrm{k}\nu}$ with respect to the v_{ns} are also shown in the right panel of Fig. 5.9. The velocity $v_{\mathrm{ns},\nu}$ starts rising significantly between 0.4 s-0.6 s postbounce, as during this period there exists a long-lasting downflow funnel (present in the $z-$direction in Fig 5.9) and the ejecta show a particularly strong dipolar asymmetry. The neutrino emission is stronger in the direction to the upper left resulting in a recoil velocity in the opposite direction. Moreover, the NS recoil velocity $v_{\mathrm{ns},\nu}$ is directed nearly opposite to the recoil direction. Nevertheless, $v_{\mathrm{ns},\nu}$ is still significantly smaller than v_{ns}, especially when taking into account that the long-ranged gravitational pull is still acting on the NS and accelerating it, while the neutrino luminosities have already decayed substantially resulting in the saturation of $v_{\mathrm{ns},\nu}$. Though the the SN shock surface remains relatively spherical, the NS is clearly displaced from the geometrical center to the upper left direction along $\mathbf{v}_{\mathrm{ns}}$.

Including the NS motion is unlikely to change our results. This was concluded by Scheck et al. (2006) from tests where the gas surrounding the NS in the grid center was allowed to move with $(-v_{\mathrm{ns}})$ by applying a Galilei transformation.

5.3.6 Neutron star spins

Tests confirmed very good linear momentum conservation of our code, while angular momentum is more difficult to conserve, e.g., when a rotating gas mass is in rapid coherent motion across large distances on the grid. We therefore estimate the NS angular momentum $\mathbf{J}_{\mathrm{ns}}$ as the negative of the angular momentum of the exterior gas, but by considering only the volume between R_{ns} and $r_{\mathrm{o}} = 500\,\mathrm{km}$ and adding to this the angular momentum that is carried by the gas flux into or out of this sphere:

$$\mathbf{J}_{\mathrm{ns}}(t) = -\left(\int_{R_{\mathrm{ns}}}^{r_{\mathrm{o}}} \mathrm{d}V \, \rho \mathbf{j}(t) + A_{\mathrm{o}} \int_0^t \mathrm{d}t' \, (\rho \mathbf{j} v_r)\,|_{r_{\mathrm{o}}} \right) , \tag{5.12}$$

where $\mathbf{j}$ is the specific angular momentum and $A_{\mathrm{o}} = 4\pi r_{\mathrm{o}}^2$. This assumes that the asymmetric gas mass outside of r_{o} does not exert any important torque on the gas mass below r_{o}. Accordingly, we see $\mathbf{J}_{\mathrm{ns}}(t)$ asymptoting (see Fig. 5.2) when accretion on the NS ends (around 0.6 s–0.8 s after bounce). At this time the asymmetric downdrafts of cool gas present between rising bubbles of high-entropy, neutrino-heated matter (Figure 5.5, left and right panels) do not reach down below 500 km, but are replaced by the spherically symmetric neutrino-driven wind around the NS (green region in the right panel of Figure 5.5). Assuming $J_{\mathrm{ns}} = |\mathbf{J}_{\mathrm{ns}}| = \mathrm{const}$ after the end of our simulations (at $t \approx 1.4\,\mathrm{s}$ p.b.), we obtain a rough estimate of the final NS spin period from $T_{\mathrm{spin}} = 2\pi I_{\mathrm{ns}}/J_{\mathrm{ns}}$ by considering a rigidly rotating, homogeneous sphere of mass M_{ns}, i.e., $I_{\mathrm{ns}} = \frac{2}{5} M_{\mathrm{ns}} R_{\mathrm{ns}}^2$, with a final radius of $R_{\mathrm{ns}} = 12\,\mathrm{km}$. We find NS spin periods in the range of $\sim 400\,\mathrm{ms}$-$1000\,\mathrm{ms}$. In addition, our results do not show any alignment/misalignment of the NS kick and spin directions.

Chapter 6

Element Distribution in Supernova Ejecta

6.1 Connection with Neutron Star Kick

At the onset of collapse nickel inside the core of the progenitor star is photo-disintegrated into alpha particles. It is only after the explosion sets in that nickel is formed once again by silicon burning in a thin shell due to compression and heating by the outwards propagating SN shockwave. Since the shock strength is stronger in the direction opposite to the NS kick direction we expect more nickel to be formed in the hemisphere opposite to the direction of NS motion. Figure 6.1 shows the nickel mass per solid angle in a cross-sectional plane normal to the NS kick direction for model W15-2 at 365 ms and 515 ms after bounce. The left panel, at 350 ms postbounce, demonstrates that more nickel is formed in the direction *opposite* to the NS kick vector indicated by the black arrow pointing to the right. We plotted the time evolution of the total mass of all nuclei considered in our nuclear burning network for model W15-2 in Figure 6.2. At around 450-500 ms after bounce we observe saturation of the total nickel mass produced in our simulation (black line in Figure 6.2) indicating that nickel formation ends then. At this stage, some fraction of the newly synthesized nickel is concentrated into downflows present in

Table 6.1: Hemispheric element distribution and total nickel mass

Model	^{4}He [$M_\odot$]		^{12}C [$10^{-1}\,M_\odot$]		^{16}O [$10^{-1}\,M_\odot$]		^{20}Ne [$10^{-2}\,M_\odot$]		^{24}Mg [$10^{-2}\,M_\odot$]	
	north	south	north	south	north	south	north	south	north	south
W15-1	2.78	2.66	1.18	1.10	3.68	3.75	8.90	8.49	2.41	2.85
W15-2	2.78	2.65	1.16	1.12	3.43	3.84	8.67	8.49	2.16	2.86
L15-1	2.39	2.34	0.90	0.87	2.77	2.89	5.00	5.06	2.12	2.49
L15-2	2.40	2.39	0.89	0.87	2.85	2.79	5.21	4.88	2.47	2.42

Model	^{28}Si [$10^{-2}\,M_\odot$]		^{40}Ca [$10^{-2}\,M_\odot$]		^{44}Ti [$10^{-3}\,M_\odot$]		^{56}Ni [$10^{-2}\,M_\odot$]		tracer [$10^{-2}\,M_\odot$]		Total ^{56}Ni [$M_\odot$]
	north	south	north	south	north	south	north	south	north	south	
W15-1	1.88	2.92	1.33	4.81	0.68	2.43	1.26	4.28	2.23	6.08	0.055-0.139
W15-2	1.74	2.83	1.27	4.66	0.81	2.17	1.37	4.09	2.22	6.27	0.055-0.139
L15-1	1.75	2.33	1.76	2.47	1.49	2.40	1.34	1.87	4.78	7.20	0.032-0.152
L15-2	2.13	2.15	2.54	2.74	2.32	2.55	1.81	1.89	8.68	9.74	0.037-0.221

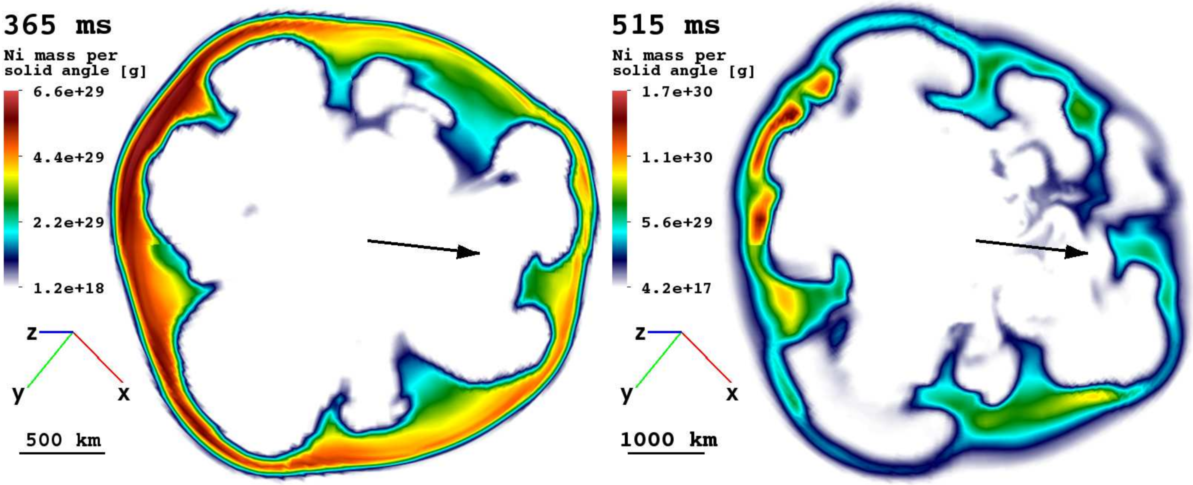

Figure 6.1: Nickel mass per solid angle plotted in a cross-sectional plane containing the NS kick direction for model W15-2 at 365 ms (left) and 515 ms (right) postbounce. The red colored regions show that more nickel is formed in the direction *opposite* to the NS kick direction, which is shown by the black arrows pointing to the right. Length scales are given by yardsticks at the lower left corner of each panel.

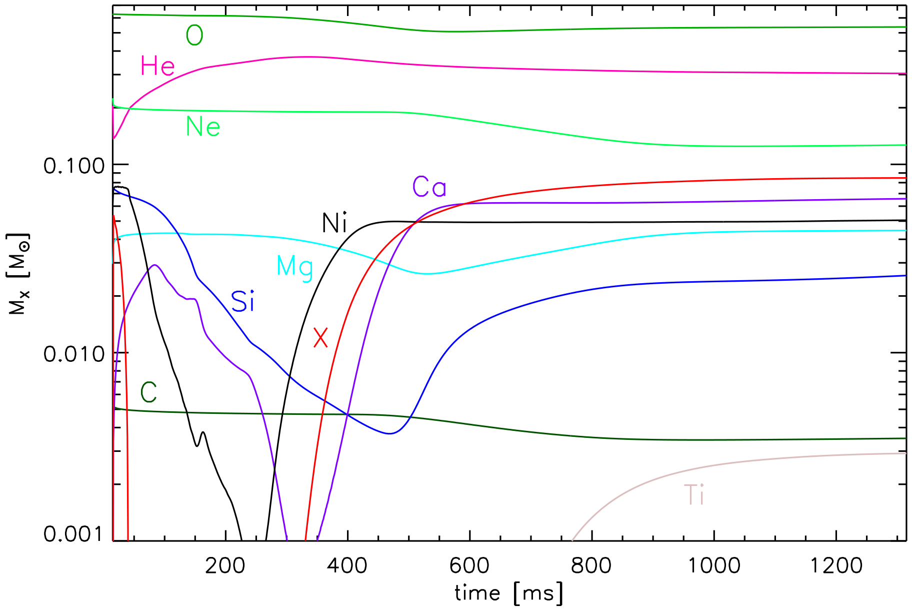

Figure 6.2: Time evolution of the total mass of nuclei considered in the nuclear burning network for model W15-2 during the explosion phase (15 ms - 1.3 s after bounce). Note that the computational domain contains only a part of the oxygen-neon-magnesium layer of the progenitor star.

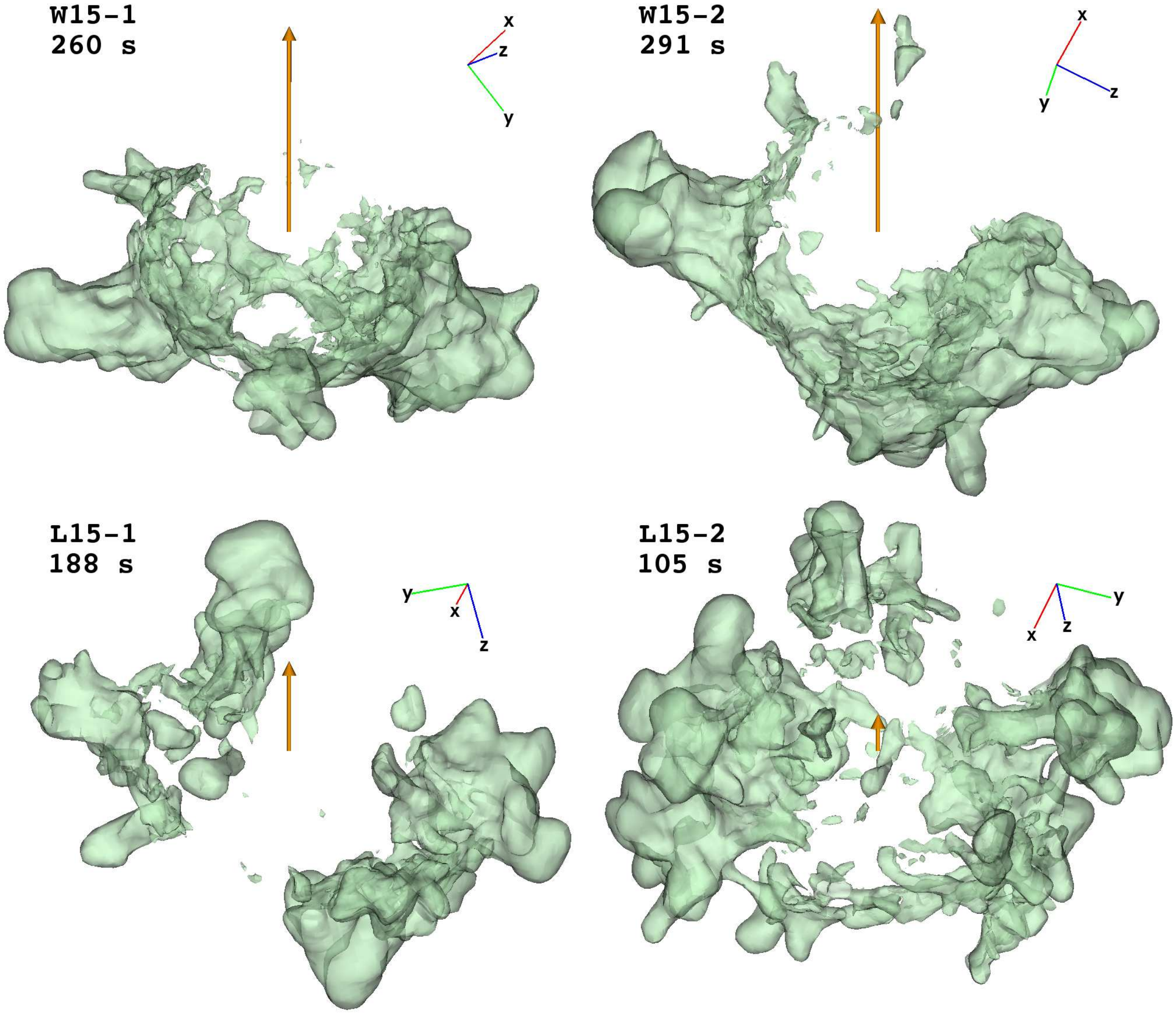

Figure 6.3: Semi-transparent isosurfaces of constant nickel mass of 3×10^{26} g at the time when all nucleosysthesis has seized in our simulations. These times are shown in the top left corner of each panel along with the model name. The orange vectors represent the NS kick direction and are scaled by the corresponding NS kick velocities (96 $\mathrm{km\,s^{-1}}$ and 575 $\mathrm{km\,s^{-1}}$ for the shortest and the longest vector, respectively) . In the top two panels showing models W15-1 (left) and W15-2 (right), the nickel mass is that is contained in the "northern" and "southern" hemispheres defined by the NS kick direction is clearly different. In contrast, models L15-1 (lower left) and L15-2 (lower right) with lower NS kick velocities do not show any clear distinction in their nickel distribution.

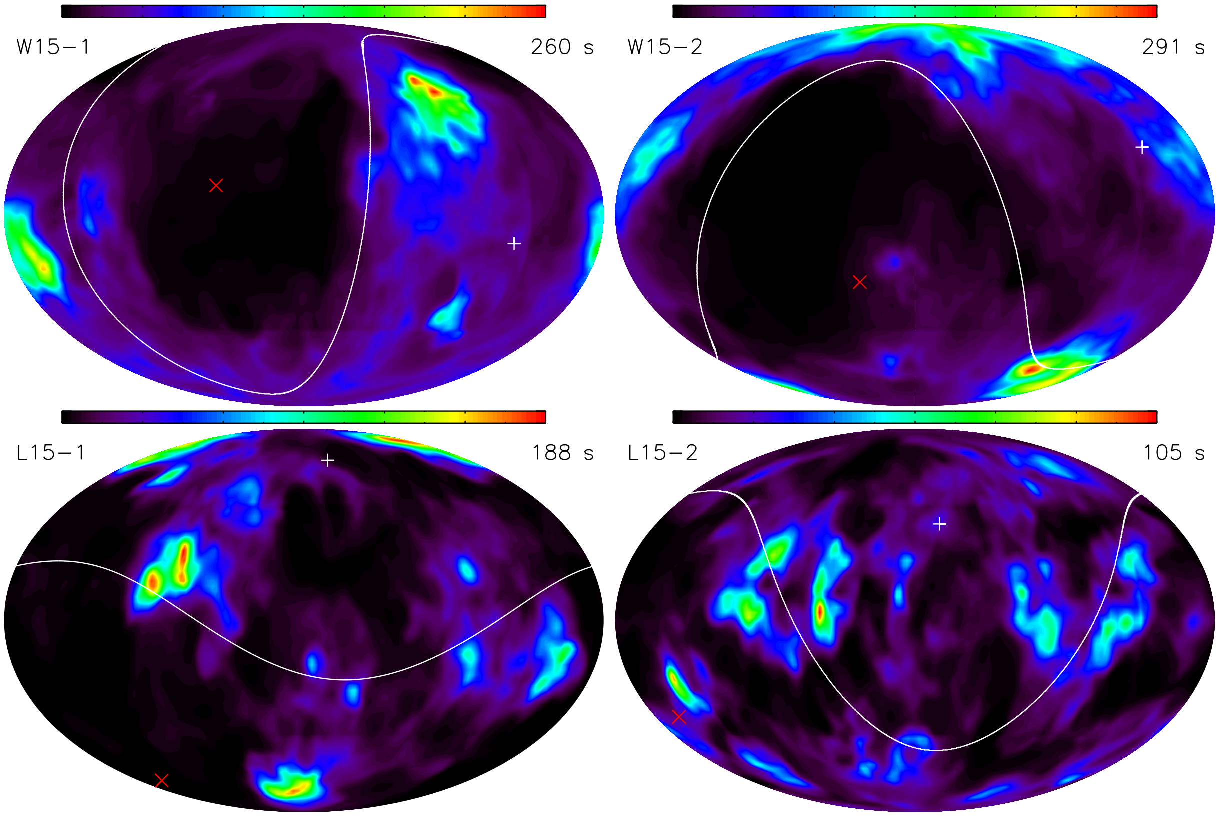

Figure 6.4: Maps of the integrated nickel mass along radial rays for models W15-1, W15-2, L15-1, and L15-2, respectively. Red crosses indicate the NS kick direction while white plus signs mark the direction *opposite* to the kick direction. White lines separate the sphere into two hemispheres with the kick direction pointing to the north pole. The nickel mass contained within the two hemispheres is clearly different for models W15-1 and W15-2 (upper panels), where more nickel is found in the hemisphere opposite to the NS kick direction. The onesidedness of the nickel distribution is not seen for model L15-1 and L15-2 (lower panels), which have smaller kick velocities.

between the diluted high-entropy bubbles which are rising and pushing outwards. The remaining nickel is concentrated into small clumps. Nevertheless, the flow dynamics does not affect the overall distribution of nickel. More nickel still remains in the hemisphere opposite to the NS kick direction.

Although nickel systhesis already stops during the explosion simulations, we continue the nucleosynthesis calculation in our long-time simulations until *all* nucleosynthesis has finished completely (*i.e.,* no grid zone fulfils our nuclear burning criteria anymore), which approximately happens at ∼100-300 s postbounce depending on the simulated model. We show the nickel mass distribution at this stage in Fig. 6.3. To this end we define a new spherical coordinate system for each of our models where the NS kick direction is pointing towards the north pole. In this coordinate system, we identify the hemisphere that the NS kick vector is pointing to as the "northern" hemisphere and the hemisphere opposite to the NS kick vector as the "southern" hemisphere. We rotate the new coordinate system such that the NS kick vectors shown by orange colored vectors are pointing directly upwards. The lengths of the NS kick vectors are scaled to the corresponding final NS kick velocities provided in Table 5.1. The two top panels show results from models W15-1 and W15-2 which possess rather high NS kick velocities noticable by long NS kick vectors. For these two models, the nickel mass distribution shows a clear contrast with very little nickel mass contained in the northern hemisphere, *i.e.,* most of the of nickel mass resides in the southern hemisphere opposite to the NS kick direction. The lower two panels give the nickel mass distributions for models L15-1 and L15-2 which both have lower NS kick velocities. These two models do not show distinct differences between the nickel mass in the northern and the southern hemisphere.

Looking only at an isosurface as in Fig. 6.3 could be misleading since the shape of the surface may strongly depend on the chosen value for which the surface is drawn. Therefore we confirm our finding by calculating also the integrated nickel mass along radial rays. Figure 6.4 shows maps of the integrated nickel mass along radial rays for models W15-1, W15-2, L15-1, and L15-2, respectively. The integrated nickel mass is defined as

$$M_{\mathrm{Ni}}^{\mathrm{ray}}(\theta,\phi) = \int_{R_{\mathrm{ib}}}^{R_{\mathrm{ob}}} \rho(r,\theta,\phi)\, X_{\mathrm{Ni}}(r,\theta,\phi)\, \Delta\Omega\, dr \tag{6.1}$$

where

$$\Delta\Omega = \Delta\phi \left[\cos\,(\theta - \frac{\Delta\theta}{2}) - \cos\,(\theta + \frac{\Delta\theta}{2})\right] \tag{6.2}$$

is the solid angle covered by each radial ray. On this map, the NS kick direction is marked by a red cross, while the opposite direction is indicated by a white plus sign. The white solid line represents the equator separating the northern and southern hemisphere. For models W15-1 and W15-2, the nickel is concentrated in the southern hemisphere. This onesidedness cannot be seen in the maps for models L15-1 and L15-2 which both show a nearly isotropic distribution of the nickel mass.

In addition, we also calculated and compared the total mass of every element included in our alpha-reaction network in the northern and southern hemisphere (see Table 6.1). We are able to separate the nuclear species into two groups based on whether the species shows clearly a hemispherically asymmetric distribution or not. It turns out that nickel is not the only species which shows an asymmetric distribution but also *silicon, calcium, titanium, and the tracer nucleus* are clearly more abundant in the southern hemisphere than in the northern hemisphere for models W15-1 and W15-2. On the other hand, helium, carbon, oxygen, neon, and magnesium do not show a clear hemispheric contrast. Note that although oxygen and magnesium are also formed asymmetrically due to stronger SN shock strength in the direction opposite to the NS kick, the asymmetries are obscured by the unperturbed spherically symmetric distribution of oxygen and magnesium inside the progenitor star. Because of the total mass is conserved, we observe helium, carbon, and neon to be concentrated more in the northern hemisphere, since more of these elements are consumed in the nuclear burning processes in the southern hemisphere. In the last column of Table 6.1, we also give the range of the total nickel mass produced in our simulations. The lower limit represents only the contribution from ^{56}Ni, while the upper limit gives the total ^{56}Ni plus tracer mass. We introduce these lower and upper limits to the total nickel mass because we are aware that only an approximative neutrino transport is included in our calculations, which therefore cannot give an extremely accurate electron fraction Y_e. Thus, it is possible that a fraction of the tracer nucleus might actually be produced as nickel instead, if we were to consider a more accurate neutrino transport.

6.2 Supernova Shock Propagation and Element Distribution

In this section, we discuss the dynamics of the SN shock as it travels through the undisturbed envelope of the progenitor star as well as the propagation of heavy elements formed during the explosion at the inner core. Figure 6.5 shows snapshots of the nickel mass per solid angle for model W15-2 in a cross-sectional plane at six different epochs starting from its formation until it reaches the edge of the hydrogen shell. The nickel mass per solid angle is defined for each grid zone as

$$M_{\Omega,\mathrm{Ni}}(r,\theta,\phi) = \rho(r,\theta,\phi)\, X_{\mathrm{Ni}}(r,\theta,\phi)\, \Delta R \tag{6.3}$$

where

$$\Delta R = \frac{(r+\Delta r/2)^3 - (r-\Delta r/2)^3}{3}, \tag{6.4}$$

and Δr is the radial grid resolution. The position of the SN shock is given by the solid black curve and the coordinate center is shown by the black cross. Length scales are given at the lower left corner of each panel, and the postbounce time at the top left corner. After nickel is formed in a thin layer behind the SN shock and clumps into smaller structures some hundred milliseconds later, it is mixed into the rising high-entropy bubbles while moving through the oxygen-neon-magnesium shell. The mass distribution of nickel at this epoch closely resembles the structure of the high-entropy bubbles (left column, middle row in Figure 6.5). The SN shock still shows the deformation acquired at the time of the explosion when it reaches the helium layer of the progenitor star. Figure 6.6 shows the mass distribution of helium, oxygen, and silicon as well as nickel at this epoch for model W15-2. In addition to the location of the SN shock shown (solid black line), we also show the carbon-helium composition interface by a red line corresponding to a helium mass fraction of 0.9. In the top left panel, the shock wave has swept up some of the mass within the carbon-helium transitional layer and compressed it into a thin but very high density layer as shown by the red region in the upper left corner of the figure. Alpha particles left inside the ejecta are visible as the dark blue region inside the SN shock. Note that although there is a vast amount of helium in the helium layer outside the red circle in Figure 6.6, it appears to contain only a small amount of helium mass (dark blue) because the figure only shows a tiny fraction of the thick helium layer and because the density is lower than in the layer swept up by the shock wave shown in dark red. The figure also shows a thick

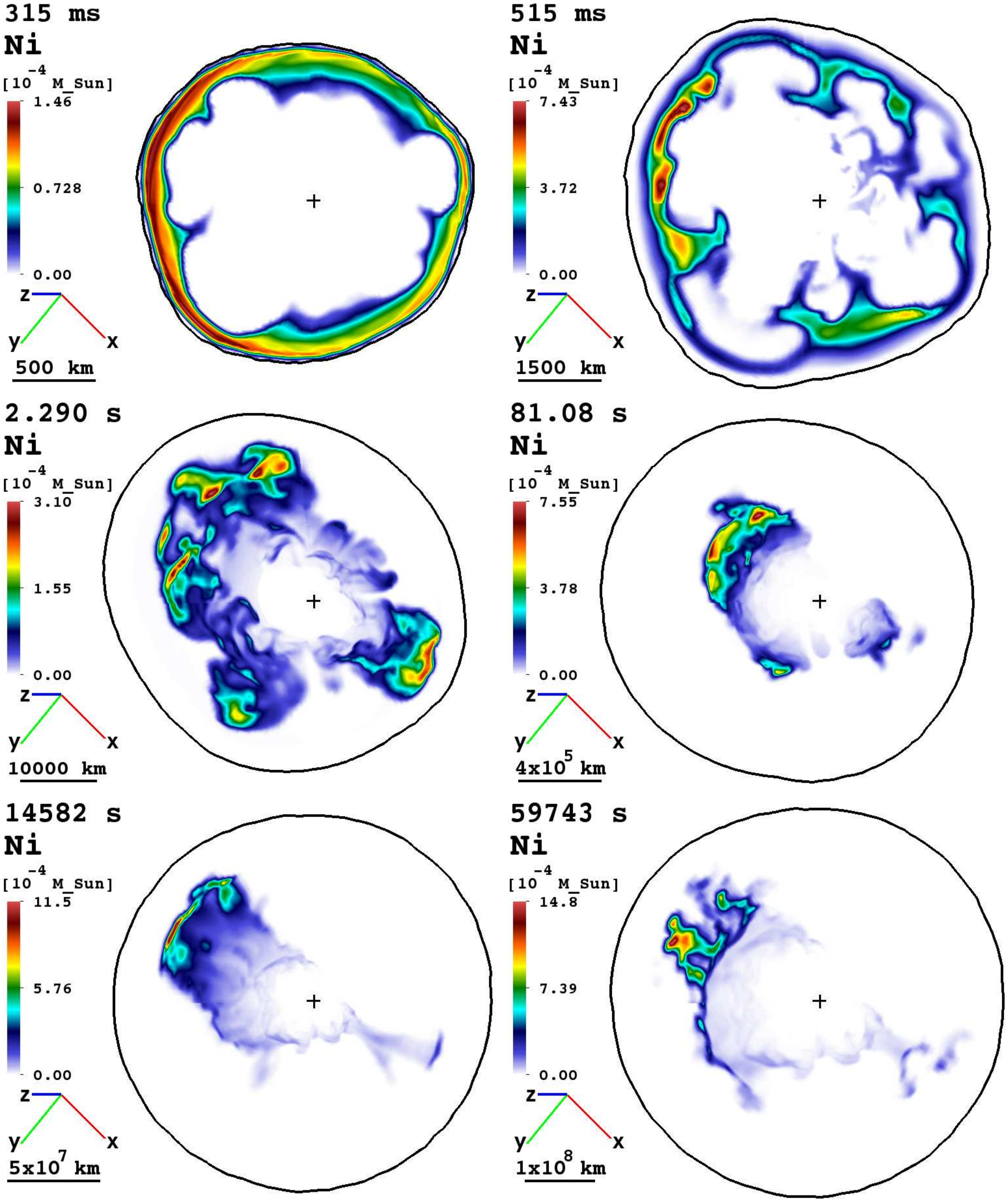

Figure 6.5: Nickel mass per solid angle plotted in a cross-sectional plane at different times for model W15-2. The SN shock radius is marked by the black line. Length scales are given at the bottom left corner of each panel. Nickel is formed in a thin shock-heated layer which fragments into clumps as the hot high-entropy bubbles push the ejecta outwards. At a later time the ejected nickel is mixed inside the high-entropy bubbles (left middle). Nickel is decelerated and slightly compressed as it propagates deep into the helium layer of the progenitor star. The shock becomes more and more spherical at this phase. Nickel eventually crashes onto the thick helium wall formed due to the deceleration when the shock enters the hydrogen envelope. It cannot penetrate through the helium wall and is compressed into a very thin layer visible in the bottom left panel. Triggered by hydrodynamic instabilities nickel shows finger-like structures as it travels through the hydrogen shell (bottom right).

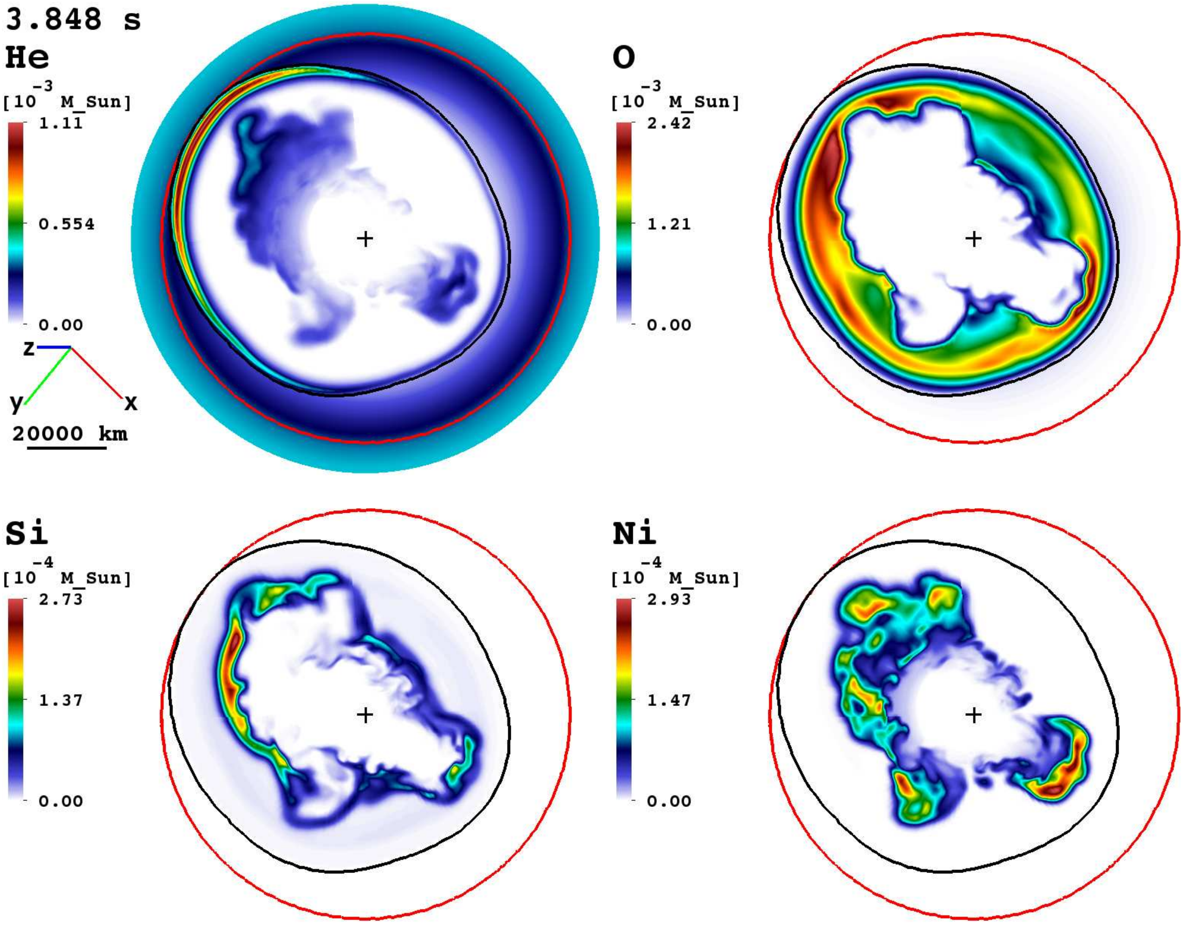

Figure 6.6: Snapshots of the mass per solid angle of different chemical species for model W15-2 at the time when the SN shock is crossing the carbon-helium compostion interface. The shock radius is outlined by the black line, while the red line marks the radius where the helium mass fraction is equal to 0.9 representing the composition interface. The shock sweeps up helium in the transitional layer forming a moon crescent shape of dense material (upper left corner, upper left panel). The oxygen core appears as a thick shell surronding the ejected material represented by silicon and nickel in the bottom two panels.

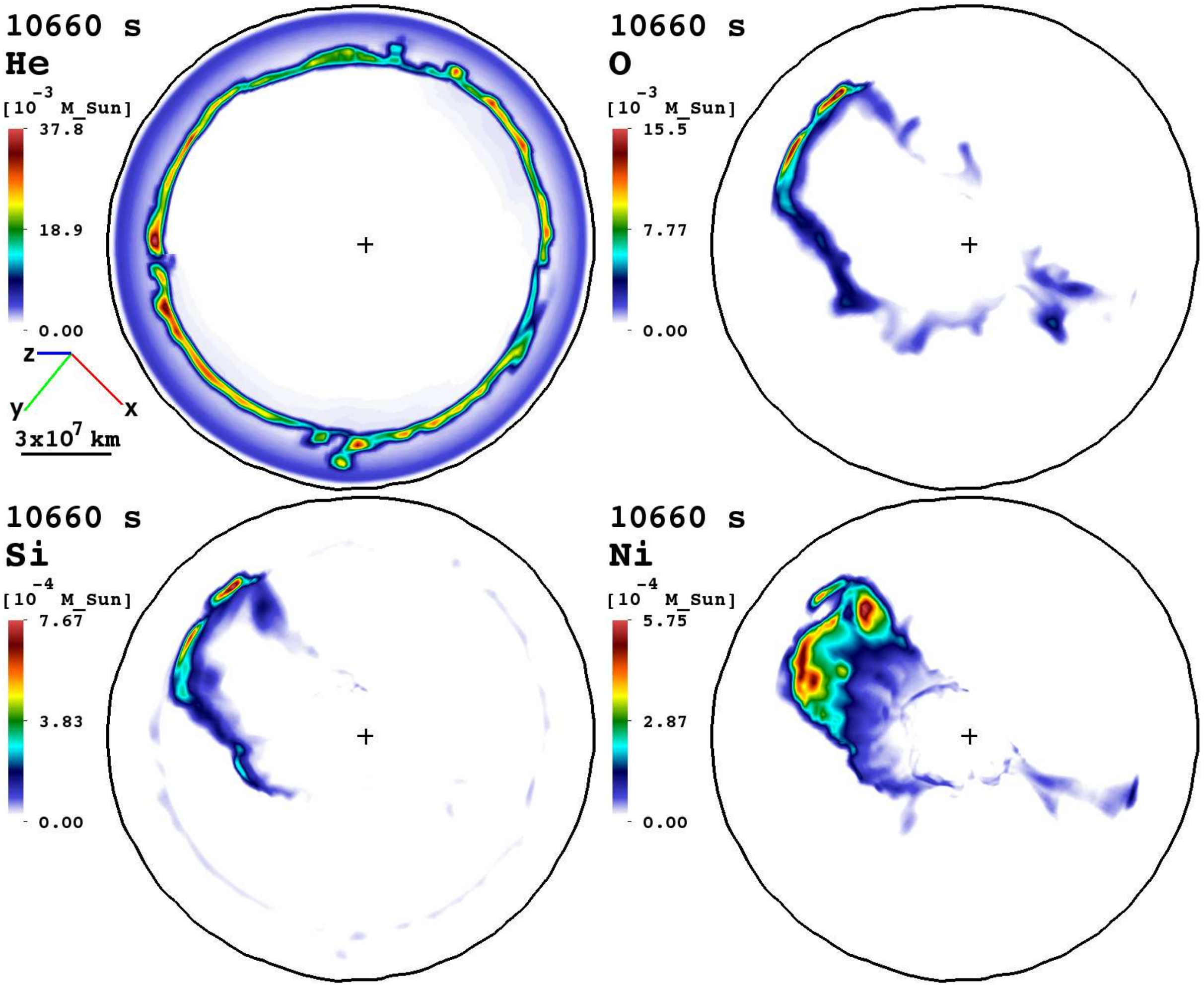

Figure 6.7: Snapshots of the mass per solid angle of different chemical species for model W15-2 at the time which the dense helium wall has formed due to the deceleration of the ejecta in the hydrogen envelope of the progenitor star. Hydrodynamic instabilites triggered by the unsteady propagation of the SN shock have already developed and are visible in the top left panel. The oxygen shell and the ejected silicon have already crashed onto the dense helium wall and are compressed into a very thin layer. The ejected nickel which is trailing behind still covers a wide radial region because it has not yet reached the helium wall.

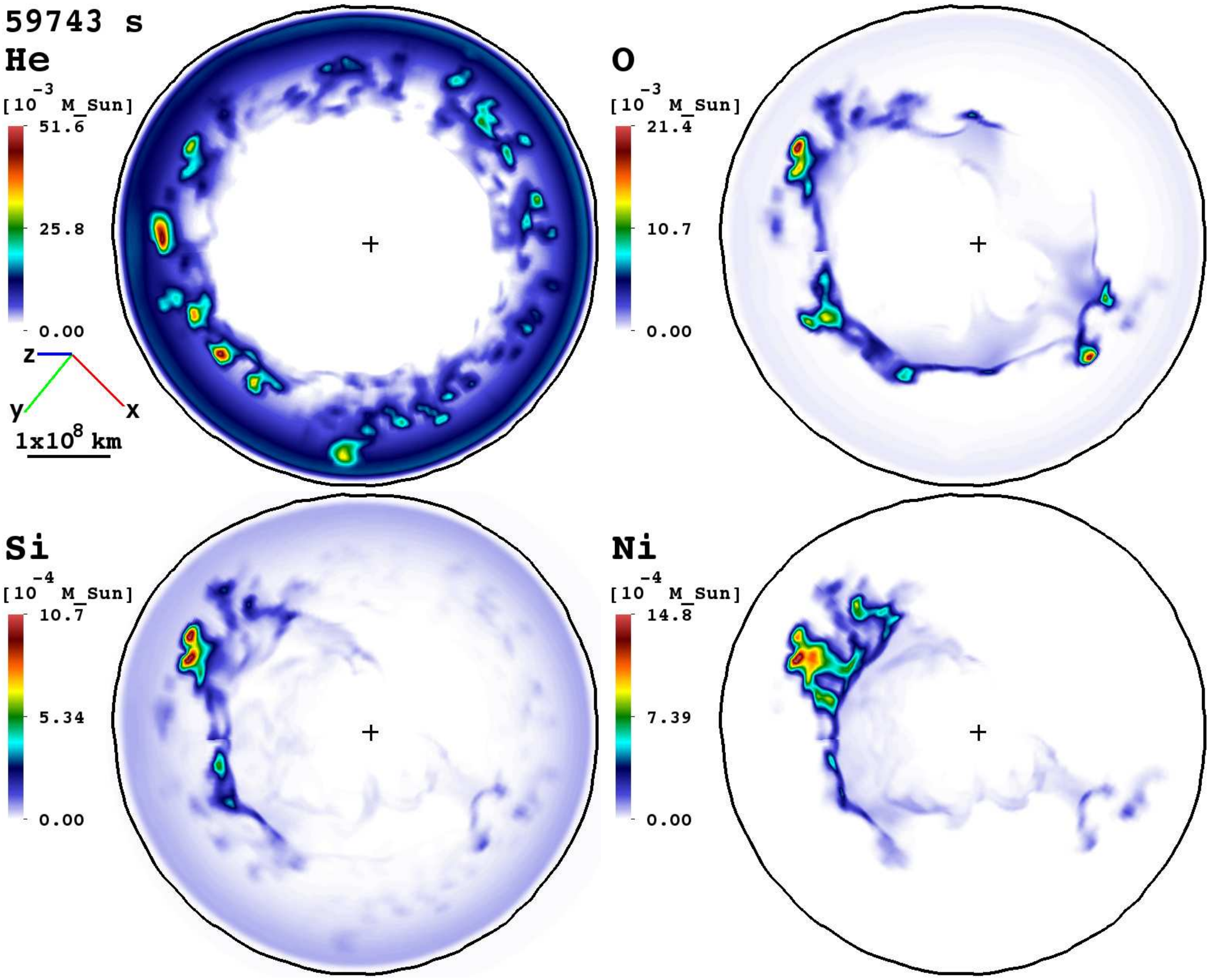

Figure 6.8: Snapshots of the mass per solid angle of different chemical species for model W15-2 at the end of the simulation, approximately 16.5 hrs after bounce. The ejecta are now concentrated into numerous small clumps due to the action of hydrodynamic instabilities. The nickel distribution displays finger-like structures (bottom right).

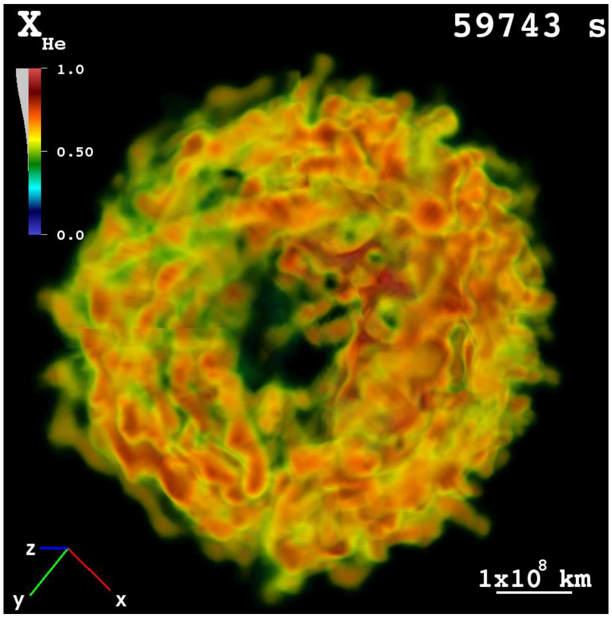

Figure 6.9: Ray-casting image of the helium mass fraction at approximately 16.5 hrs after bounce showing the hydrodynamic instabilities in three dimensions triggered at the helium-hydrogen composition interface by the SN shock propagation. The length scale is given at lower right corner of the figure.

layer of oxygen (upper right panel), still surrounding the silicon and nickel synthesized during the explosion.

As the SN shock enters and propagates through the thick layer of helium it is decelerated, which is reflected by the fact that the deformed shock wave becomes more and more spherical (right column, middle row in Figure 6.5). The ejected nickel material is also slowed down, which is now compressed into a thinner structure than at much earlier time. Once the SN shock reaches the helium-hydrogen composition interface and propagates into the hydrogen envelope it is drasticallly decelerated as it sweeps up a lot of material. The SN shock becomes completely spherical at this time. The swept up helium layer is compressed into a very thin, very dense helium "wall" which later prevents other nuclear species from penetrating through. Triggered by the propagation of the SN shock hydrodynamic instabilities start developing at this helium wall. This is shown for model W15-2 in Figure 6.7, where the helium wall is visible in the top left panel. At this time, oxygen and silicon have already crashed onto this helium wall, and they thus are concentrated into very thin layers. On the other hand, the nickel ejecta has not reached the thick helium wall yet. Therefore, nickel is still spread out radially much more than oxygen and silicon. Nonetheless, as shown in the lower left panel of Figure 6.5, the nickel ejecta eventually reaches the thick helium wall and is compressed into a very thin structure, too. The final snapshot of the time evolution shows that Rayleigh-Taylor instabilities grow as indicated by the finger-like structures, in the nickel mass distribution. In addition, we show the distribution of helium, oxygen, and silicon at this epoch for model W15-2 in Figure 6.8. As the instabilities develop and grow the helium wall is fragmented into many small helium clumps. Oxygen and silicon are also concentrated into small clumps, but the number is much less than that of the helium clumps.

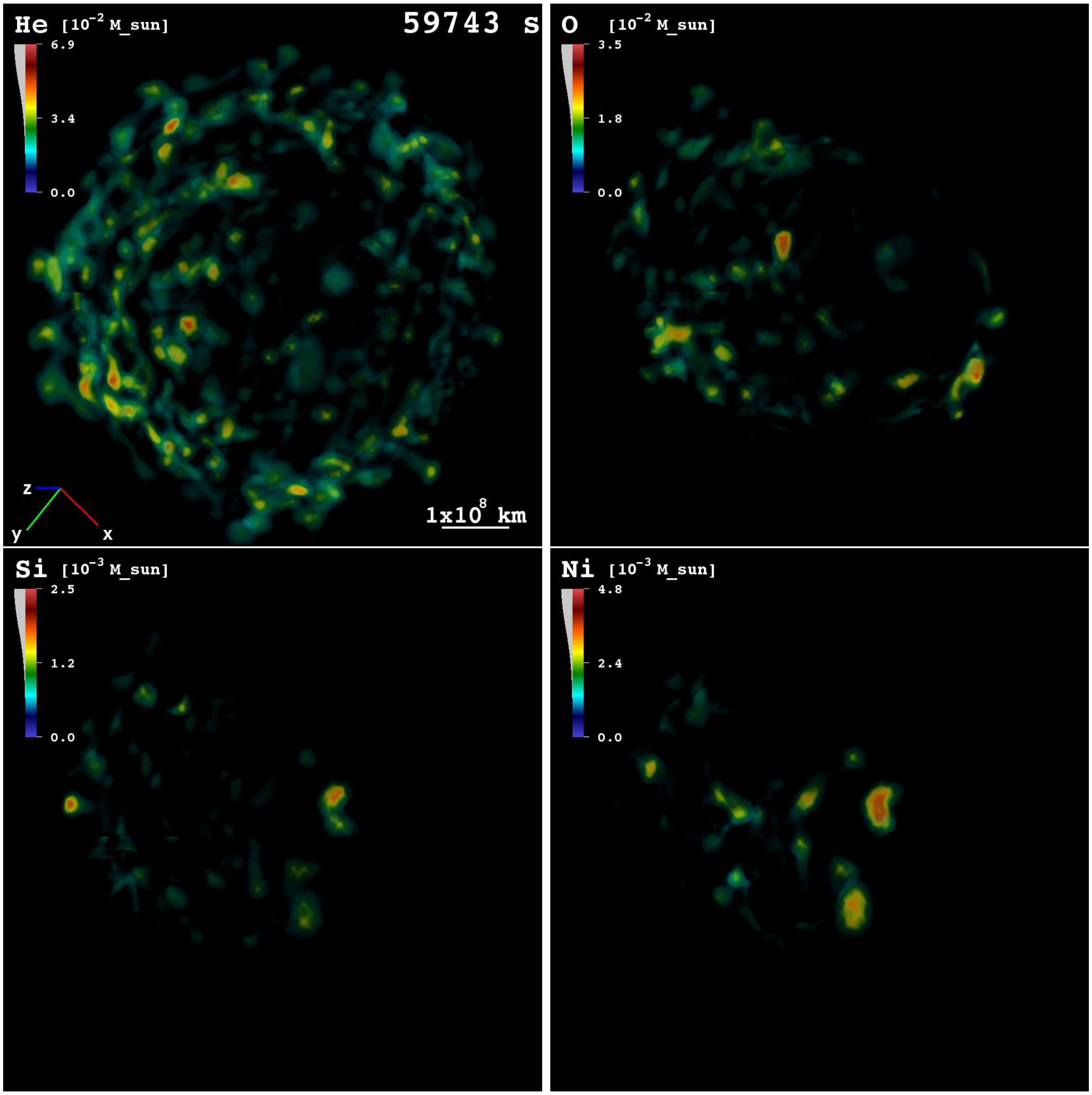
He [10^-2 M_sun]
6.9
3.4
0.0
59743 s
z
y
x
1x10^8 km
O [10^-2 M_sun]
3.5
1.8
0.0
Si [10^-3 M_sun]
2.5
1.2
0.0
Ni [10^-3 M_sun]
4.8
2.4
0.0

Figure 6.10: Ray-casting images of the mass per solid angle of different chemical species at 16.5 hrs after bounce. The figure shows numerous clumps of helium and oxygen, while the number of silicon and nickel clumps is much less.

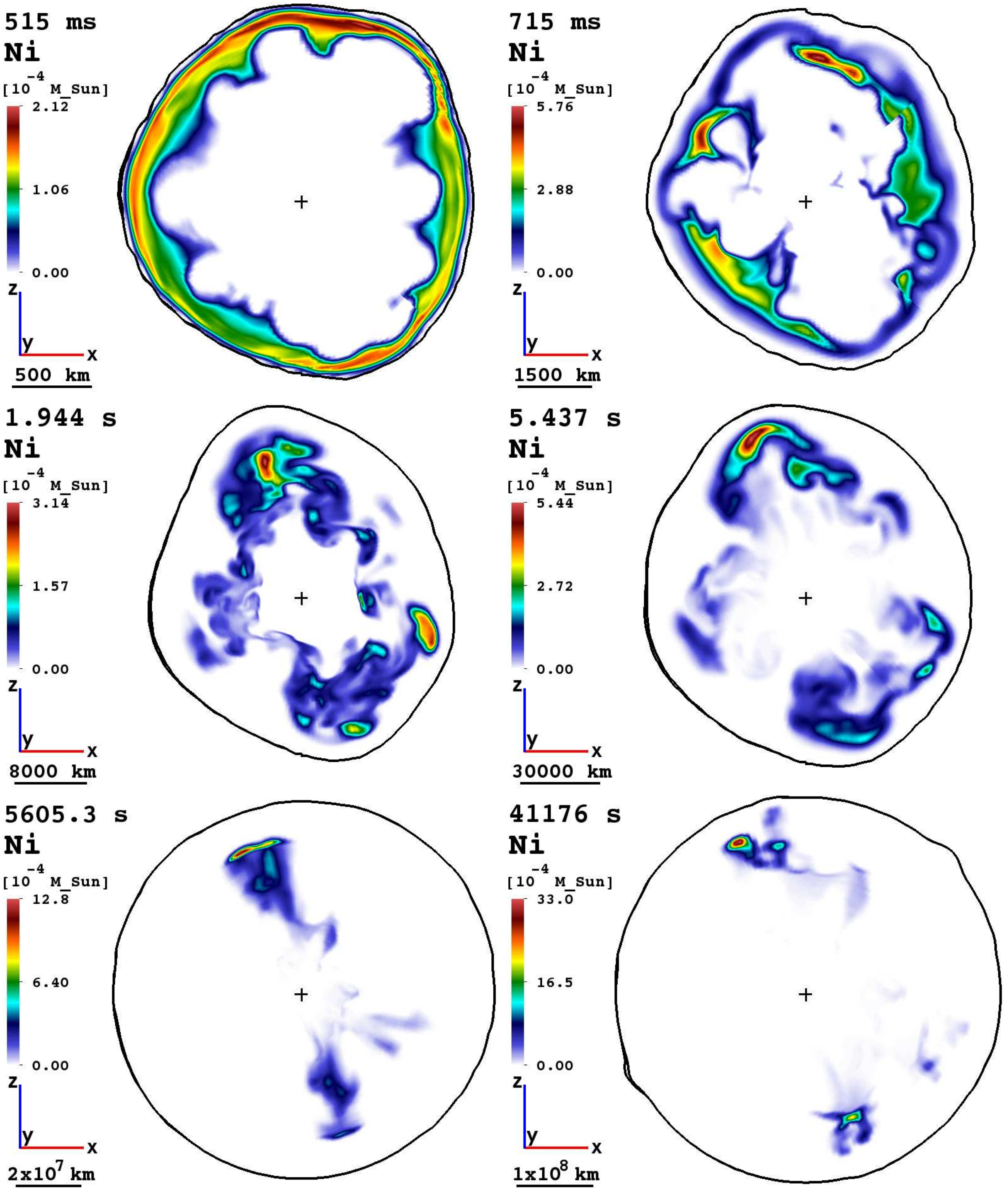

Figure 6.11: Same as Figure 6.5 but for model L15-1. The nickel mass distribution develops a bipolar structure although no jet mechanism was invoked.

So far we have shown only two-dimensional slices plotting the mass per solid angle of each nuclear species at different times of the evolution without giving details about how the structures look in three dimensions. Figure 6.9 shows a ray-casting image of the helium mass fraction at approximately 16 hrs after bounce, the time which at instabilities develop at the helium-hydrogen composition interface for model W15-2 . The figure shows numerous Rayleigh-Taylor fingers of high helium mass fraction (in orange and dark red) penetrating into the hydrogen shell. Figure 6.10 illustrates ray-casting images of the mass per solid angle for helium, oxygen, silicon, and nickel for model W15-2. The figure can be interpreted as showing the mass distribution projected onto a plane normal to the viewing direction. The figure reveals even more small helium clumps than what were shown in a two-dimensional slice in Figure 6.8. The number of oxygen clumps appears to be much less than those of helium. Finally, the number of silicon and nickel clumps is only of the order of ten.

We have also investigated the dynamical evolution for model L15-1 which has a different progenitor star than model W15-2. Figure 6.11 gives the nickel mass per solid angle in a cross-sectional plane at different epochs. We do not find any significant difference in the dynamical evolution of this model compared to model W15-2. Moreover, simulations of models W15-1 and L15-2 yield similar results, too.

6.3 Distribution in Mass Coordinate and Velocity Space

Figure 6.12 shows the normalized mass distribution of different nuclear species plotted versus mass coordinate $M(r)$ (left column) and radial velocity (right column) for all models. The distributions are calculated just before the SN shockwave leaves the computational domain. In the left column, one can notice that a small amount (of the order of $\sim$1%) of nickel and the tracer nucleus (blue and black curves), representing heavy elements synthesized during the explosion, are able to penetrate into the hydrogen envelope and nearly reach the stellar surface. On the other hand, hydrogen is mixed deep into the inner part of the ejecta as can be seen by the smooth decline of the dark green curve between approximately $M(r) \approx 7 - 8M_\odot$ and $M(r) \approx 2M_\odot$.

The right column shows that nickel is accelerated to radial velocities of about $4000\,\mathrm{km\,s^{-1}}$ for all models except for model L15-2 where the nickel even reaches a velocity of approximately $5500\,\mathrm{km\,s^{-1}}$. The differences in the velocity distributions can be directly related to the different explosion energy of the models. Models W15-1, W15-2, and L15-1 all develop an explosion energy of approximately 1.12×10^{51} erg, while model L15-2 has a higher explosion energy of 1.74×10^{51} erg. The explosion energy is defined as the sum of internal, kinetic, and gravitational energy for all zones where this quantity is positive. Since the shock wave is propagating ballistically at late times the kinetic energy dominates over the internal and gravitational energy by orders of magnitude. Therefore, we can approximately equate the explosion energy to the kinetic energy. Consequently, the radial velocity scales with the square root of the explosion energy. The normalized mass versus radial velocity curves for all nuclear species should shift to a higher radial velocity by a factor of $\sqrt{1.74/1.12} \approx 1.25$ for model L15-2 with respect to all other models, which indeed is the case.

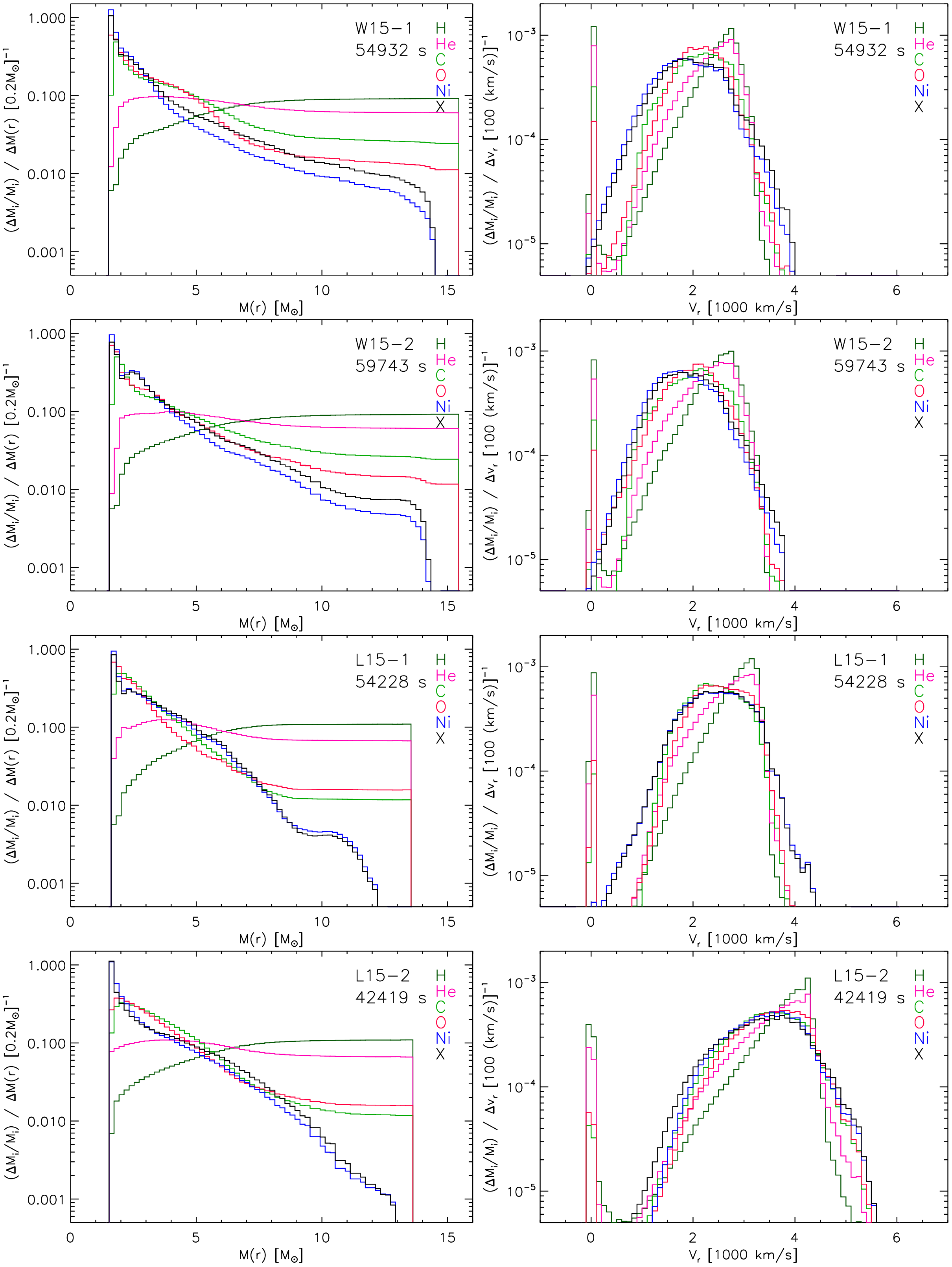

Figure 6.12: Normalized mass distribution of different nuclear species versus mass coordinate (left column) and radial velocity (right column) at the time when the SN shock wave is about to leave the computational domain for all models. Nickel is able to penetrate into the hydrogen envelope for all cases with a velocity ranging from approximately 4000 km s^{-1} to 5500 km s^{-1}.

6.4 Comparison with Previous Work

In comparison with the recent work by Hammer et al. (2010), who also simulated self-consistently the evolution in three dimensions of the neutrino-driven SN explosion starting from shortly after bounce until hours later, we find several differences. Firstly and most importantly, we consider $15\,M_\odot$ red supergiant stars while Hammer et al. (2010) considered a $15\,M_\odot$ blue supergiant. A blue supergiant star has a much more compact structure compared with a red supergiant star of the same mass. Our computational domain extends out to 3.3×10^{13} cm while in Hammer et al. (2010) the star has a radius of 3.9×10^{12} cm only, approximately a factor of 10 smaller than in our case. Consequently, in their simulations they observed large nickel bullets penetrating carbon, oxygen, and helium shells with large velocities deep into the hydrogen envelope of the star. In contrast, we find that our nickel clumps suffer a longer deceleration by drag forces and thus are not able to break out of the thick helium shell. Once the Rayleigh-Taylor instabilities grow at the helium-hydrogen interface mixing nickel is transported into the hydrogen envelope.

The second difference is how the explosion phase was followed. Hammer et al. (2010) used the three dimensional explosion model calculated by Scheck et al. (2006). The explosion model was followed until only 0.5 s when the explosion energy has not yet saturated, and the explosion yields an explosion energy of only 0.6×10^{51} erg. They then artificially boosted the explosion energy up to 1×10^{51} erg. On the other hand, our explosion models follow the evolution until approximately 1.4 s after bounce, when the explosion energy is very close to saturation. Moreover, we included an alpha-reaction nuclear network in our calculations while they did not.

Another difference is the computational grid employed for the simulation. In Hammer et al. (2010) the computational grid did not cover the full sphere. A small cone of 5.8° half opening angle was cut out near the polar axis to relax the CFL timestep condition. Thus they had to assume a reflecting boundary condition near the polar axis, which however did not create any obvious numerical artifact to the hydrodynamical flow. We confirmed this result by repeating the three dimensional simulation of Hammer et al. (2010) with our axis-free Yin-Yang grid.

Recently Joggerst et al. (2010) investigated three different $15\,M_\odot$ progenitors: one blue supergiant and two red supergiant stars. The explosions were initiated with a spherical piston instead of a more realistic physics treatment (as in our case based on the assumed viability of the neutrino-heating mechanism). They also focused on the comparison between results from 2D and 3D simulations, similar to what was discussed in Hammer et al. (2010), and found that instabilities initially grow faster in 3D than in 2D, in agreement with Hammer et al. (2010). However, clumps of heavy elements are not able to penetrate through shells of lighter elements as seen in Hammer et al. (2010).

6.5 Comparison with current observations

Since we calculate only a small set of simulations it is not possible to compare our results directly to any individual SNR in particular. Thus, in this section, we only discuss the implications of our findings for observations in general.

6.5.1 Neutron star kicks and heavy elements distributions

First of all, we find a connection between the distribution of some heavy elements synthesized during the explosion and the direction of the neutron star recoil. As already discussed in

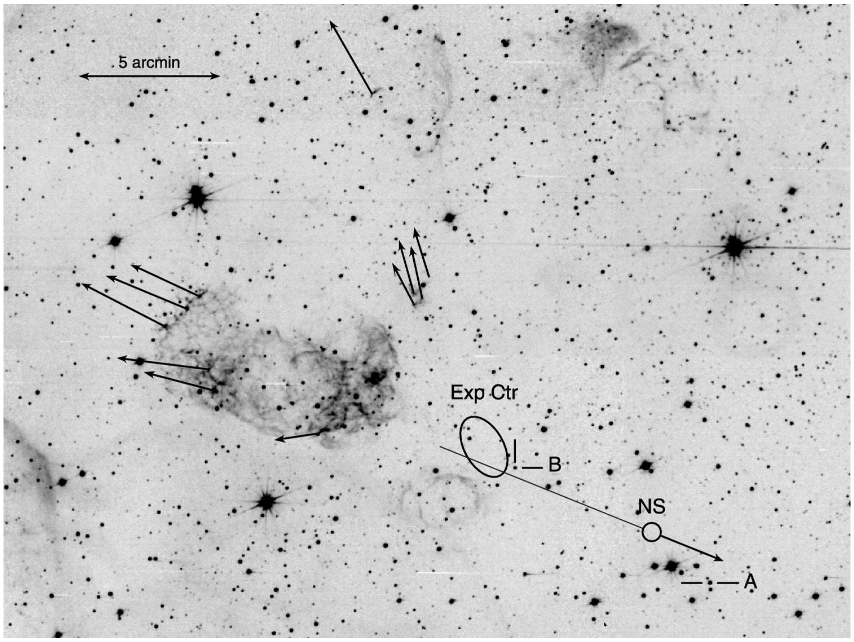

Figure 6.13: Optical image of the central region of Puppis A in [OIII] λ5007, showing proper motions of the O-rich filaments and RX J0822-4300. The arrows indicate proper-motion vectors for ~1000 yr, and the ellipse shows the 90% confidence contour for the expansion center. (This is a wider field version of Fig. 1 from Winkler et al. (1988) overlaid on a more recent CCD image.) The circle marked NS shows the present position for the presumed neutron star, RX J0822-4300, and the attached vector indicates its motion over 1000 yr at the rate we have measured. Backward extrapolation of its present motion (thin line) passes well within the error ellipse for the expansion center of the O-rich filaments. Figure and description from Winkler & Petre (2007).

Section 6.1, the explosion strength is stronger in the direction opposite to the neutron star kick direction for cases where the neutron star kick velocity exceeds several hundred $\mathrm{km\,s^{-1}}$. Therefore, we find elements heavier than ^{28}Si concentrated more in the hemisphere opposite to the neutron star kick direction. This hemispheric asymmetry cannot be destroyed during the subsequent evolution of the explosion, *e.g.,* when the SN shock propagates through the stellar envelope or after the SN shock breaks out to the interstellar medium.

Our results which are based on the hydrodynamical neutron star kick mechansim lead to the opposite conclusion to what is predicted if anisotropic neutrino emission is responsible for the neutron star kick. In the latter case, the explosion strength is stronger in the same direction as the neutron star's motion. This leads to higher concentration of heavy elements in the same direction as the neutron star recoil. Therefore, combining observations of hemispheric asymmetries of heavy elements and neutron star's proper motion provides a direct way to constrain the neutron star kick mechanism. There are only a few SNRs for which both detailed spatial distributions of heavy elements in the remnants and the neutron star's proper motion can be deduced from observations. An excellent example is the Puppis A SNR.

Puppis A is a galactic "oxygen-rich" SNR (Winkler & Kirshner 1985) which has Cas A as the prototype (Kirshner & Chevalier 1977; Chevalier & Kirshner 1978). The shock wave is observed to interact with a complex system of interstellar clouds. Using Chandra observations combined with laboratory simulations of cloud-shock interaction, the estimated onset of the cloud-shock interaction is 2000-4000 yr ago (Hwang et al. 2005; Klein et al. 2003). The compact object RX J0822-4300 is associated with the Puppis A remnant (Petre et al. 1996) and is observed to travel with a velocity of $\sim 1600\,\mathrm{km\,s^{-1}}$ (Winkler & Petre 2007). Hui & Becker (2006) found a lower velocity of $\sim 1100\,\mathrm{km\,s^{-1}}$, which however can still be considered as a very high neutron star kick velocity. Figure 6.13 shows the spatial distribution of fast-moving O-rich filaments/knots observed in the Puppis A SNR. These structures have been found only in the northeastern region of the remnant. They are believed to be the relics of an asymmetric SN explosion, and not contaminated by the interstellar medium (Winkler & Kirshner 1985; Winkler et al. 1988). The proper motion vector of the compact object RX J0822-4300 is pointing to the southwest direction, opposite to the concentration of O-rich filaments/knots (see Fig 6.13). This is very similar to what we observe in our model W15-2 with the highest neutron star kick velocity of $575\,\mathrm{km\,s^{-1}}$. More recent observations using combined XMM-Newton and Chandra data show X-ray emission from O-rich filaments/knots (Katsuda et al. 2008, 2010). These X-ray emitting filaments/knots are coincident with O-rich knots with high velocities found in optical observations. These observations oppose the anisotropic neutrino emission model for the neutron star kick and favor the hydrodynamical mechanism. However, Petre et al. (1982) pointed out the possibility that the O-rich knots can well be explained with a complicated structure of the interstellar medium surrounding Puppis A. More detailed observations are needed to confirm that the asymmetry of the O-rich filaments/knots originates from the SN explosion itself, not from inhomogenieties in the interstellar medium.

Another example is the Cas A SNR. The compact object of Cas A SNR has a velocity of $\sim 350\,\mathrm{km\,s^{-1}}$ (e.g., Fesen et al. 2006). DeLaney et al. (2010) and Isensee et al. (2010) derived the three-dimensional structure of Cas A. Rest et al. (2010) confirms the asymmetry of the Cas A SN explosion, in accordance with previous observations (e.g., Hughes et al. 2000; Willingale et al. 2002). These asymmetries are believed to be intrinsic to the explosion itself, and not arising from the interaction with the circumstellar medium. The remnant shows a bipolar structure of Fe-rich outflows in the southeast and northwest direction. The northwest outflow is found to orient almost in opposite direction to the derived proper motion of the central compact object (Rest et al. 2010). More detailed observations regarding the connection between the neutron star's motion and distributions of elements in Cas A are upcoming (Satterfield et al. 2011).

6.5.2 Mixing of elements in stellar envelopes

There is ample evidence of large-scale mixing of elements in the stellar envelope of the progenitor of SN 1987A (see, e.g., Arnett et al. 1989, for a review). Besides SN1987A, also observations of other CCSNe indicate large-scale mixing throughout the envelope (see, e.g., Wang & Wheeler 2008). Using one-dimensional radiation hydrodynamic calculations, modelling of the light curve of SN 1987A suggests that a substantial amount of Ni should be mixed outward to the H/He interface, and H should be mixed inward into the He core (Woosley 1988; Shigeyama & Nomoto 1990; Blinnikov et al. 2000; Utrobin 2004). The theoretical light curves of Utrobin et al. (1995) require the presence of a high-velocity Ni clump ($\sim$4700 km s^{-1}). High-velocity dense knots/filaments, *e.g.,* as those observed in Puppis A also provide strong evidence of mixing processes. These observations can be explained by our simulations, where we find extensive mixing at the H/He interface resulting from hydrodynamic instabilities triggered by the non-steady propagation of the SN shock wave. Figure 6.10 shows dense clumps similar to those observed, which also possess high-velocities of the order of a few thousand km s^{-1} (see Figure 6.12).

Chapter 7

Summary and outlook

During the past decade one-dimensional CCSNe simulations have failed to deliver a successful explosion, suggesting that multi-dimensional effect must play an important role in understanding the explosion mechanism. Although two-dimensional simulations already revealed the importance of multi-dimensional fluid instabilities concerning the explosion mechanism, astrophysicists yearn for three-dimensional CCSNe simulations. To this end, the goal of this work is to study CCSNe by means of three-dimensional simulations relying on the viability of the neutrino-driven explosion mechanism.

CCSNe simulations in three dimensions are computationally very demanding, especially when using the spherical coordinate system. By employing the usual latitude-longitude grid for spatial discretization of the computational domain in angular directions, one encounters the so-called "pole problem" since the coordinate lines converge at the north and south pole of the sphere resulting in extremely small grid zones, and therefore an extremely small time step for the simulation. To avoid this problem, we adopt and implement an overlapping grid technique called the "Yin-Yang" grid into the computer program, Prometheus. The Yin-Yang grid helps resolving the pole-problem by getting rid of the high-latitude parts of the sphere and thus allows for a much larger time step. The time step gain can be as large as a factor of 40 for a simulation with 2° angular resolution, and factors of several hundred for higher angular resolutions. Moreover, it has an advantage over other overlapping grid techniques in spherical coordinates due to its simple geometry allowing it to be implemented relatively easily. The code is tested by standard hydrodynamic test problems such as Sod's shock tube problem and the Taylor-Sedov blast wave problem as well as some astrophysically relevant problems, e.g., the Rayleigh-Taylor instability and the evolution of rotating polytropes in three dimensions. We found a conservation problem, common for overlapping grid techniques if only interpolation is used for communication of data between neighbouring grids. Conservation for scalar conserved quantities (density and total energy) can be ensured with an additional step of flux calculation. However, we are still not able to ensure conservation for vector quantities, *i.e.,* momentum, using the same scheme. Nevertheless, results show very good agreement with known solutions and the conservation problem does not destroy the viability of the code for CCSNe simulations.

Using the newly developed code, we performed a series of three-dimensional CCSNe simulations. We started the simulations at a time shortly after the formation of the SN shock wave ($\sim 15\,\mathrm{ms}$ after core bounce). The shock wave stalls at a radius of around 100-200 km and is later revived by neutrino energy deposition in the post shock layers. First, we focus on studying the hydrodynamical neutron star kick mechanism. Young neutron stars are observed to possess average space velocities around $400\,\mathrm{km\,s^{-1}}$. In some rare cases, the neutron star kick velocity can exceed a thousand $\mathrm{km\,s^{-1}}$. Results from our simulations show that these high velocities of the neutron star can be naturally obtained. The highest neutron star velocity found in one of our models is $\sim 600\,\mathrm{km\,s^{-1}}$. This high velocity resulted mainly from the long-lasting gravitational drag forces exerted on the neutron star by dense clumps of matter distributed asymmetrically in the ejecta. Our results are in agreement with results of two-dimensional simulations performed by Scheck et al. (2006). We also found a connection between the neutron star kick direction and the distributions of heavy elements in the SN ejecta. In cases where the neutron star possesses a kick velocity of the order of several hundred $\mathrm{km\,s^{-1}}$, the explosion strength is stronger in the direction opposite to the neutron star's motion. This results in higher concentration of heavy elements, synthesized by explosive nuclear burning during the explosion, in the hemisphere opposite to the neutron star kick direction. This is just opposite to what is predicted by neutrino kicks due to anisotropic emission. Therefore, combined observations of distributions of elements in SNRs and neutron star's proper motion can provide a direct way to constrain the neutron star kick mechanism. Evidence has already been accumulated in the case of the Puppis A and Cas A SNRs. Observations of these SNRs revealed neutron stars moving in the opposite direction of concentration of dense fast-moving O-rich filaments/knots. Nevertheless, more observations are needed to confirm such conclusions.

We also study the mixing of elements in the stellar envelope as the SN shock wave propagates outwards by performing long-time simulations. We followed the SN evolution until the shock wave breaks out of the progenitor star. We found (additional to the ones in the neutrino-heated hot bubble deep inside the star) hydrodynamic instabilities developing at the H/He interface triggered by the non-steady propagation of the SN shock wave. This leads to fragmentation of the onion-skin like compositional structure of the progenitor star into small dense clumps, and to extensive mixing of elements as suggested by one-dimensional light curve modelling of, *e.g.,* SN 1987A. Some of the clumps are moving with high velocities exceeding $\sim 3500\,\mathrm{km\,s^{-1}}$.

Still, more work is left to be done. So far, we have investigated only a small set of three-dimensional models, as due to high demand of computing time for a three-dimensional CCSN simulation, we are not able to cover a wide range of parameter space. A larger set of simulations covering a wider range of explosion energies and a larger variety of progenitor models are needed to confirm our findings and to gain further insight.

Bibliography

Arcones, A., Janka, H., & Scheck, L. 2007, A&A, 467, 1227

Arnett, W. D., Bahcall, J. N., Kirshner, R. P., & Woosley, S. E. 1989, ARA&A, 27, 629

Arras, P. & Lai, D. 1999, ApJ, 519, 745

Arzoumanian, Z., Chernoff, D. F., & Cordes, J. M. 2002, ApJ, 568, 289

Baade, W. & Zwicky, F. 1934a, Proceedings of the National Academy of Science, 20, 254

Baade, W. & Zwicky, F. 1934b, Physical Review, 46, 76

Bethe, H. A. 1990, Reviews of Modern Physics, 62, 801

Blinnikov, S., Lundqvist, P., Bartunov, O., Nomoto, K., & Iwamoto, K. 2000, ApJ, 532, 1132

Blondin, J. M. & Mezzacappa, A. 2007, Nature, 445, 58

Blondin, J. M., Mezzacappa, A., & DeMarino, C. 2003, ApJ, 584, 971

Buras, R., Janka, H., Rampp, M., & Kifonidis, K. 2006, A&A, 457, 281

Buras, R., Rampp, M., Janka, H., & Kifonidis, K. 2003, Physical Review Letters, 90, 241101

Burrows, A. & Hayes, J. 1996, Phys. Rev. Lett., 76, 352

Burrows, A. & Woosley, S. E. 1986, ApJ, 308, 680

Chandrasekhar, S. 1939, An introduction to the study of stellar structure (The University of Chicago press)

Chandrasekhar, S. 1969, Ellipsoidal figures of equilibrium (Yale Univ. Press)

Chesshire, G. & Henshaw, W. 1994, SIAM J. Sci. Comput., 15, 819

Chevalier, R. A. 1984, Annals of the New York Academy of Sciences, 422, 215

Chevalier, R. A. & Kirshner, R. P. 1978, ApJ, 219, 931

Chin, Y.-N. & Huang, Y.-L. 1994, Nature, 371, 398

Chugai, N. N. 1984, Sov. Astron. Lett., 10, 87

Colella, P. & Glaz, H. M. 1985, J. Comput. Phys., 59, 264

Colgate, S. A. & White, R. H. 1966, ApJ, 143, 626

Collela, P. & Woodward, P. R. 1984, J. Comput. Phys., 54, 174

DeLaney, T., Rudnick, L., Stage, M. D., et al. 2010, ApJ, 725, 2038

Eriguchi, Y. & Müller, E. 1985, A&A, 147, 161

Faucher-Giguère, C. & Kaspi, V. M. 2006, ApJ, 643, 332

Fesen, R. A., Hammell, M. C., Morse, J., et al. 2006, ApJ, 645, 283

Filippenko, A. V. 1997, ARA&A, 35, 309

Foglizzo, T. 2002, A&A, 392, 353

Foglizzo, T. & Tagger, M. 2000, A&A, 363, 174

Fragile, P. C., Lindner, C. C., Anninos, P., & Salmonson, J. D. 2009, ApJ, 691, 482

Fryxell, B., Müller, E., & Arnett, D. 1991, ApJ, 367, 619

Fuller, G. M., Kusenko, A., Mocioiu, I., & Pascoli, S. 2003, Phys. Rev. D, 68, 103002

Gardner, F. F. & Milne, D. K. 1965, AJ, 70, 754

Green, D. A. & Gull, S. F. 1984, Nature, 312, 527

Hammer, N. J., Janka, H., & Müller, E. 2010, ApJ, 714, 1371

Herant, M. 1995, Phy. Rep., 256, 117

Hillebrandt, W. 1994, in Supernovae, ed. S. A. Bludman, R. Mochkovitch, & J. Zinn-Justin, 251

Hillebrandt, W. & Niemeyer, J. C. 2000, ARA&A, 38, 191

Hobbs, G., Lorimer, D. R., Lyne, A. G., & Kramer, M. 2005, MNRAS, 360, 974

Hoyle, F. & Fowler, W. A. 1960, ApJ, 132, 565

Hughes, D. W. 1980, Nature, 285, 132

Hughes, J. P., Rakowski, C. E., Burrows, D. N., & Slane, P. O. 2000, ApJL, 528, L109

Hui, C. Y. & Becker, W. 2006, A&A, 457, L33

Hwang, U., Flanagan, K. A., & Petre, R. 2005, ApJ, 635, 355

Isensee, K., Rudnick, L., DeLaney, T., et al. 2010, ApJ, 725, 2059

Janka, H., Langanke, K., Marek, A., Martínez-Pinedo, G., & Müller, B. 2007, Phys. Rep., 442, 38

Janka, H. & Müller, E. 1994, A&A, 290, 496

Janka, H. & Müller, E. 1996, A&A, 306, 167

Joggerst, C. C., Almgren, A., & Woosley, S. E. 2010, ApJ, 723, 353

Johnston, S., Hobbs, G., Vigeland, S., et al. 2005, MNRAS, 364, 1397

Johnston, S., Kramer, M., Karastergiou, A., et al. 2007, MNRAS, 381, 1625

Kageyama, A. & Sato, T. 2004, Geochemistry Geophysics Geosystems, 5

Kaplan, D. L., Chatterjee, S., Gaensler, B. M., & Anderson, J. 2008, ApJ, 677, 1201

Katsuda, S., Hwang, U., Petre, R., et al. 2010, ApJ, 714, 1725

Katsuda, S., Mori, K., Tsunemi, H., et al. 2008, ApJ, 678, 297

Kifonidis, K., Plewa, T., Janka, H., & Müller, E. 2003, A&A, 408, 621

Kifonidis, K., Plewa, T., Janka, H.-T., & Müller, E. 2003, A&A, 408, 621

Kirshner, R. P. & Chevalier, R. A. 1977, ApJ, 218, 142

Kitaura, F. S., Janka, H., & Hillebrandt, W. 2006, A&A, 450, 345

Klein, R. I., Budil, K. S., Perry, T. S., & Bach, D. R. 2003, ApJ, 583, 245

Koldoba, A. V., Romanova, M. M., Ustyugova, G. V., & Lovelace, R. V. E. 2002, ApJ, 576, L53

Kotake, K., Sato, K., & Takahashi, K. 2006, Reports on Progress in Physics, 69, 971

Lai, D., Chernoff, D. F., & Cordes, J. M. 2001, ApJ, 549, 1111

Landau, L. & Lifshitz, E. 1959, Fluid mechanics, Vol. 6 (Pergamon)

Limongi, M., Straniero, O., & Chieffi, A. 2000, ApJS, 129, 625

Liou, M.-S. 1996, J. Comput. Phys., 129, 364

Livio, M. 2000, in Type Ia Supernovae, Theory and Cosmology, ed. J. C. Niemeyer & J. W. Truran, 33

Marschall, L. A. 1988, The supernova story (Plenum)

Mezzacappa, A. 2005, Annual Review of Nuclear and Particle Science, 55, 467

Minkowski, R. 1941, Publ. Astron. Soc. Pac., 53, 224

Müller, E. 1998, in Saas-Fee Advanced Course 27: Computational Methods for Astrophysical Fluid Flow., ed. O. Steiner & A. Gautschy, 343

Müller, E., Fryxell, B., & Arnett, D. 1991b, A&A, 251, 505

Müller, E., Fryxell, B., & Arnett, D. 1991a, in European Southern Observatory Conference and Workshop Proceedings, ed. I. J. Danziger & K. Kjaer, Vol. 37, 99

Müller, E. & Steinmetz, M. 1995, Comput. Phys. Commun., 89, 45

Ng, C. & Romani, R. W. 2007, ApJ, 660, 1357

Nordhaus, J., Brandt, T. D., Burrows, A., Livne, E., & Ott, C. D. 2010, Phys. Rev. D, 82, 103016

Peng, X., Xiao, F., & Takahashi, K. 2006, Q.J.R. Meteorol. Soc., 132, 979

Petre, R., Becker, C. M., & Winkler, P. F. 1996, ApJL, 465, L43

Petre, R., Kriss, G. A., Winkler, P. F., & Canizares, C. R. 1982, ApJ, 258, 22

Plewa, T. & Müller, E. 1999, A&A, 342, 179

Quirk, J. J. 1994, Int. J. Num. Meth. Fluids, 18, 555

Rampp, M. & Janka, H. 2000, ApJL, 539, L33

Rankin, J. M. 2007, ApJ, 664, 443

Rest, A., Foley, R. J., Sinnott, B., et al. 2010, ArXiv e-prints

Romanova, M. M., Ustyugova, G. V., Koldoba, A. V., Wick, J. V., & Lovelace, R. V. E. 2003, ApJ, 595, 1009

Ronchi, C., Iacono, R., & Paolucci, P. S. 1996, J. Comput. Phys., 124, 93

Satterfield, J., DeLaney, T., & Chatterjee, S. 2011, in American Astronomical Society Meeting Abstracts, Vol. 217, American Astronomical Society Meeting Abstracts, 256.15

Scheck, L., Kifonidis, K., Janka, H.-T., & Müller, E. 2006, A&A, 457, 963

Scheck, L., Plewa, T., Janka, H.-T., Kifonidis, K., & Müller, E. 2004, Phys. Rev. Lett., 92, 011103

Schlegel, E. M. 1990, MNRAS, 244, 269

Shigeyama, T. & Nomoto, K. 1990, ApJ, 360, 242

Socrates, A., Blaes, O., Hungerford, A., & Fryer, C. L. 2005, ApJ, 632, 531

Sod, G. A. 1978, J. Comput. Phys., 27, 1

Staelin, D. H. & Reifenstein, III, E. C. 1968, Science, 162, 1481

Stephenson, F. R. & Green, D. A. 2002, The historical supernovae and their remnants (Oxford University Press)

Strang, G. 1968, SIAM J. Numer. Anal., 5, 506

Thompson, C. 2000, ApJ, 534, 915

Thompson, T. A., Burrows, A., & Pinto, P. A. 2003, ApJ, 592, 434

Timmes, F. X. & Swesty, F. D. 2000, ApJS, 126, 501

Toro, E. F. 1997, Riemann solvers and numerical methods for fluid dynamics - a practical introduction (Springer)

Trimble, V. 1973, Pub. Astron. Soc. Pacific., 85, 579

Turatto, M. 2003, in Lecture Notes in Physics, Berlin Springer Verlag, Vol. 598, Supernovae and Gamma-Ray Bursters, ed. K. Weiler, 21–36

Utrobin, V. P. 2004, Astronomy Letters, 30, 293

Utrobin, V. P., Chugai, N. N., & Andronova, A. A. 1995, A&A, 295, 129

Wang, C., Lai, D., & Han, J. L. 2006, ApJ, 639, 1007

Wang, L. & Wheeler, J. C. 2008, ARA&A, 46, 433

Wang, Z. 1995, J. Comput. Phys., 122, 96

Wheeler, J. C. 1990, in Supernovae, ed. Wheeler, J. C., Piran, T., & Weinberg, S., Supernovae. Proceedings., World Scientific, Singapore (Singapore), 1–93

Wheeler, J. C. & Levreault, R. 1985, ApJL, 294, L17

Willingale, R., Bleeker, J. A. M., van der Heyden, K. J., Kaastra, J. S., & Vink, J. 2002, A&A, 381, 1039

Winkler, P. F. & Kirshner, R. P. 1985, ApJ, 299, 981

Winkler, P. F. & Petre, R. 2007, ApJ, 670, 635

Winkler, P. F., Tuttle, J. H., Kirshner, R. P., & Irwin, M. J. 1988, in IAU Colloq. 101: Supernova Remnants and the Interstellar Medium, ed. R. S. Roger & T. L. Landecker, 65

Wongwathanarat, A., Hammer, N. J., & Müller, E. 2010, A&A, 514, A48

Woosley, S. & Janka, T. 2005, Nature Physics, 1, 147

Woosley, S. E. 1988, ApJ, 330, 218

Woosley, S. E. & Eastman, R. G. 1997, in NATO ASIC Proc. 486: Thermonuclear Supernovae, ed. P. Ruiz-Lapuente, R. Canal, & J. Isern, 821

Woosley, S. E., Pinto, P. A., Martin, P. G., & Weaver, T. A. 1987, ApJ, 318, 664

Woosley, S. E. & Weaver, T. A. 1995, ApJS, 101, 181

Wu, Z.-N., Xu, S.-S., Gao, B., & Zhuang, L.-S. 2007, Comput. Fluids, 36, 1657

Young, P. A. & Arnett, D. 2004, in Stellar Collapse, ed. C. L. Fryer, Astrophysics and Space Science Library, 5–38

Zink, B., Schnetter, E., & Tiglio, M. 2008, Phys. Rev. D, 77

Acknowledgements

First of all, I would like to thank Ewald Müller, my supervisor, for introducing me to such an interesting project, for all support, and for his valuable time. This work could not be completed without his supervision.

Special thanks to Hans-Thomas Janka for providing magnificent ideas for the project. Thanks also for his supervision and time for discussions.

Many thanks to Nicolay J. Hammer for the incredible pioneer work of implementing the Yin-Yang grid into Prometheus. Without his effort, I would not have finished the work within my PhD time. Thanks also for giving support when I started learning the code.

Thanks to efforts from Markus Rampp and Klaus Reuter to provide support for visualization. Nice figures would have been impossible without their support.

Thanks to MPA staffs for nice support on everything and for nice working environment.

Thanks to Monique Alves Cruz, my best friend at MPA, for making three and a half year of PhD time much more enjoyable.

Thanks to Zhongli Zhang for all her support and encouragement. It would have been so difficult time without her.

Thanks to all IMPRS students for valuable friendship.

Last but not least, thanks to my parents, Anant and Chutikarn Wongwattanarat, my sister, Aornsuda Wongwattanarat, and my brother, Attakorn Wongwattanarat, for everything. I am able to come to this point because of their support and love.

“ Thank you ... ”